Spatial and temporal aspects of intense attosecond pulses for pump-probe experiments

Wikmark, Hampus

2019

Document Version:
Publisher's PDF, also known as Version of record

Spatial and temporal aspects of intense attosecond pulses for pump-probe experiments

HAMPUS WIKMARK
FACULTY OF ENGINEERING | LUND UNIVERSITY

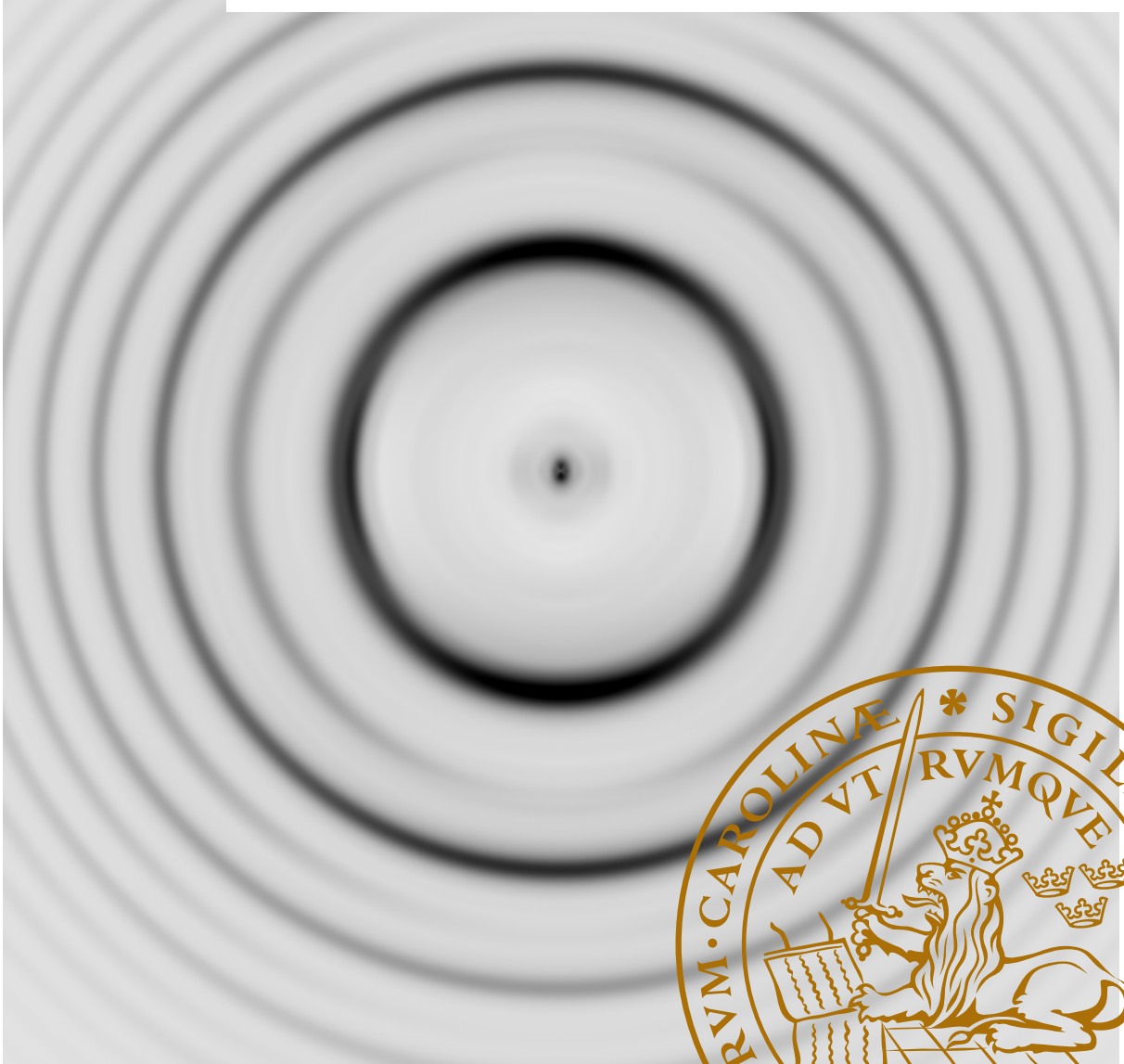

Spatial and temporal aspects of intense attosecond pulses for pump-probe experiments

Spatial and temporal aspects of intense attosecond pulses for pump-probe experiments

by Hampus Wikmark

LUND
UNIVERSITY

Thesis for the degree of Doctor of Philosophy
Thesis advisors: Doctor Per Johnsson, Professor Anne L'Huillier
Faculty opponent: Professor Eric Mével, Université de Bordeaux

To be presented, with the permission of the Faculty of Engineering of Lund University, for public criticism in the Rydberg lecture hall (Rydbergsalen) at the Department of Physics on Friday, May 17 2019 at 09:15.

Organization
LUND UNIVERSITY

Department of Physics
Box 118
SE–221 00 LUND
Sweden

Document name
DOCTORAL DISSERTATION

Date of disputation
2019-05-17

Sponsoring organization

Author(s)
Hampus Wikmark

Title and subtitle
Spatial and temporal aspects of intense attosecond pulses for pump-probe experiments

Abstract
Nuclear and electronic dynamics in atoms and molecules are the foundation of many physical processes and chemical reactions. Often, these dynamics take place on timescales so much shorter than those commonly encountered that they are called ultrafast.

In order to study ultrafast phenomena, time-resolved techniques such as pump-probe experiments, involving ultrafast light pulses, are necessary. For these experiments to be successful, the properties of ultrafast light pulses must be carefully controlled and examined in order to discern their influence on the experiment.

This thesis deals with the spatial and temporal properties of XUV light, generated through the process of high-order harmonic generation in gases, using an intense IR laser beam. The influence of the spatial properties of this generating laser on the XUV has been studied, as has the influence of the XUV light's spatial properties on its focusability and peak intensity.

The generated high-order harmonics are also used to study physical phenomena such as multiphoton ionization, something that requires high intensities. An instrument for simultaneous studies of ions and electrons produced by photoionization is also presented.

The efforts towards ultrafast pump-probe experiments include designs for interferometer setups to enable these experiments. Some preliminary results of interferometer testing are also given, including a proof of principle of XUV-IR pump-probe experiments on the Lund Laser Centre intense XUV beamline.

Key words
ultrafast lasers, attosecond pulses, pump-probe experiments, XUV light, wavefront sensing, XUV and X-ray optics

Classification system and/or index terms (if any)

Supplementary bibliographical information

Language
English

ISSN and key title
0281-2762
Lund Reports on Atomic Physics, LRAP-556.

ISBN
978-91-7895-042-3 (print)
978-91-7895-043-0 (pdf)

Recipient's notes

Number of pages
241

Price

Security classification

Signature 

Date 2019-04-05

Spatial and temporal aspects of intense attosecond pulses for pump-probe experiments

by Hampus Wikmark

LUND
UNIVERSITY

A doctoral thesis at a university in Sweden takes either the form of a single, cohesive research study (monograph) or a summary of research papers (compilation thesis), which the doctoral student has written alone or together with one or several other author(s).

In the latter case the thesis consists of two parts. An introductory text puts the research work into context and summarizes the main points of the papers. Then, the research publications themselves are reproduced, together with a description of the individual contributions of the authors. The research papers may either have been already published or are manuscripts at various stages (in press, submitted, or in draft).

Cover illustration front: An illustration of the photoelectron momenta resulting from XUV ionization of neon in the presence of an IR field. Data by Jasper Peschel.

Cover illustration back: The intense XUV beamline.

This thesis was typeset in Adobe Garamond Pro using XeLaTeX. Most figures were produced or reproduced by the author using MATLAB, Inkscape and/or **Microsoft Paint**.

Faculty of Engineering, Department of Physics

ISBN: 978-91-7895-042-3 (print)
ISBN: 978-91-7895-043-0 (pdf)
ISSN: 0281-2762
Lund Reports on Atomic Physics, LRAP-556.

Printed in Sweden by Media-Tryck, Lund University, Lund 2019

Har ingen användning alls för att gå till roten
Med småproblem när man har alla svaren som står i boken
Bara luftmotståndet går emot en, lättvindigt
Solen leder ut mig, breder ut mig, som lättsinnet

- Pst/Q

Abstract

Nuclear and electronic dynamics in atoms and molecules are the foundation of many physical processes and chemical reactions. Often, these dynamics take place on timescales so much shorter than those commonly encountered that they are called ultrafast.

In order to study ultrafast phenomena, time-resolved techniques such as pump-probe experiments, involving ultrafast light pulses, are necessary. For these experiments to be successful, the properties of ultrafast light pulses must be carefully controlled and examined in order to discern their influence on the experiment.

This thesis deals with the spatial and temporal properties of XUV light, generated through the process of high-order harmonic generation in gases, using an intense IR laser beam. The influence of the spatial properties of this generating laser on the XUV has been studied, as has the influence of the XUV light's spatial properties on its focusability and peak intensity.

The generated high-order harmonics are also used to study physical phenomena such as multiphoton ionization, something that requires high intensities. An instrument for simultaneous studies of ions and electrons produced by photoionization is also presented.

The efforts towards ultrafast pump-probe experiments include designs for interferometer setups to enable these experiments. Some preliminary results of interferometer testing are also given, including a proof of principle of XUV-IR pump-probe experiments on the Lund Laser Centre intense XUV beamline.

Populärvetenskaplig sammanfattning

Målet med arbetet som ledde till den här avhandlingen är att möjliggöra studier av *dynamiska processer i atomer och molekyler*. Ett annat sätt att uttrycka det är att vi vill kunna studera vad atomer och molekyler gör, på deras egen tidsskala. Detta sker så otroligt snabbt (vi pratar ofta om attosekunder, miljarddelars miljarddelars sekunder) att det enda mätinstrumentet vi har som är tillräckligt snabbt är ljuspulser, som vi kallar ultrakorta.

För att vi ska kunna göra det krävs många tekniska och vetenskapliga framsteg. I den här avhandlingen fokuserar jag på två huvudsakliga områden: vi behöver *korta, intensiva pulser* av ljus, och vi behöver kunna styra pulserna noggrant i tiden, i så kallade *pump-prob-experiment*.

Intensiva attosekundpulser

Varför behöver vi *intensiva attosekundpulser*? Först och främst vill vi som sagt ha pulser som är minst lika snabba, eller korta, som de fenomen vi vill studera. En gammal Moraklocka är vacker, och väldigt bra på att berätta tiden på dagen, men är förmodligen inte lämplig när vi vill ta tid på ett 100-meterslopp. Dessa ultrakorta pulser är inte lätta att framställa, så en viktig del av avhandlingen beskriver hur vi skapar dem med hjälp av nästan lika korta ljuspulser från mycket starka lasrar, i en process som kallas högre ordningens övertongenerering.

Det är dock inte nog med att de är korta, utan vi vill att de ska vara intensiva också. Om vi vill studera en process med hjälp av fotoner, ljuspartiklar, så avgörs såklart hur många "mätvärden" vi får vid varje tillfälle av hur många fotoner vi har tillgängliga just då. Vissa experiment kräver att en given atom eller molekyl tar upp två fotoner på en gång (eller inom en miljondels miljarddels sekund!), och i sådana fall behöver vi ha så många fotoner att det kan hända regelbundet.

En sak som avgör hur intensiva våra pulser kan bli är hur väl vi kan fokusera dem. På samma sätt som solljus kan starta bränder om det fokuseras med en lupp, kan en fokusering av våra ultrakorta laserpulser göra att vi kan studera helt nya fenomen.

En viktig del av mitt avhandlingsarbete har därför varit att, förutom att studera hur vi kan skapa dessa pulser, också studera hur vi effektivt kan fokusera dem, och vilka av deras egenskaper vi måste ta hänsyn till för att vi ska kunna göra det.

Flera pulser: pump-prob-experiment

Vi vet nu hur vi kan skapa väldigt korta pulser, men hur kan vi använda dem? För att kunna lära oss mer om atomers och molekylers värld, och de korta tiderna i denna värld, så måste vi ha en referens; vi kan inte veta t.ex. hur fort något händer om vi inte vet både när det börjar och när det slutar.

För att ta ett exempel som ofta dök upp under skrivandet av den här avhandlingen, så tycker jag om att dricka te med en skvätt mjölk. Jag vet inte hur teet "borde" smaka utan mjölken, utan det visar sig när jag hällt i den. När jag väl häller i mjölken svalnar teet så mycket att det inte längre drar.

Jag har alltså problemet att jag vill avgöra hur lång tid en process tar (teet drar och blir gott), men jag kan bara göra en mätning, sedan har jag under-, över- eller lagom bryggt te. Det här är också vad som händer oss när vi vill studera många fysiska fenomen, vi kan bara studera eftermälet men kan inte avgöra vad som händer medan det faktiskt händer.

Det jag kan göra är att, för varje kopp te jag brygger, variera när jag häller i mjölken och provsmakar teet, sedan kan jag följa hur gott det är. Om jag börjar från noll (jag häller i mjölken omedelbart efter tepåsen) och varierar tiden upp till, säg, sex-sju minuter, så kommer smaken antagligen att variera från blaskig, till god, till alldeles för besk. Figur 1 visar hur jag kan markera detta (för enkelhetens skull ger jag ett smakbetyg från 1-10).

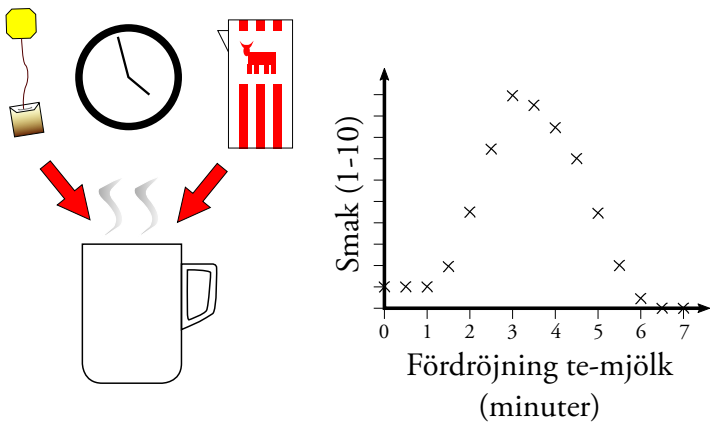

Figur 1: Ett enkelt pump-prob-experiment: Jag noterar smaken på mitt te som en funktion av när jag häller i mjölken, dvs hur länge teet får dra.

Mitt försök att avgöra hur länge teet borde dra är ett exempel på ett pump-prob-experiment; jag påbörjar en process (lägger tepåsen i vattnet) och varierar sedan när jag gör min mätning (häller i mjölken och smakar) för att avgöra hur lång tid processen tar. Det första steget kallas "pump" i den ultrasnabba jargongen och det andra för "prob" (sond). Genom att göra samma experiment flera gånger så kan jag avgöra tidsutvecklingen utan att behöva mäta den direkt.

Samma teknik har visat sig vara användbar för många experiment inom fysik och kemi. Våra mätinstrument är inte tillräckligt snabba för att upplösa själva händelserna, men vi kan använda två pulser och studera resultatet av att variera tidsskillnaden mellan de två.

Om vi till exempel vet att följden av en reaktion är att en molekyl splittras, så kan vi starta reaktionen med en ljuspuls, och sedan skicka in en ljuspuls lite senare för att undersöka vad som hänt. Till exempel kan den här pulsen stämma överens i energi med en energinivå som finns i en atom som lämnat molekylen, men inte i den hela molekylen. Genom att mäta antalet av dessa atomer som en funktion av tidsfördröjningen kan vi då avgöra hur lång tid det tar för molekylen att splittras.

Eftersom det handlar om otroligt små fördröjningar vi vill studera så kan vi inte skapa pulser separat och hoppas att de träffar vårt studieobjekt samtidigt. Istället börjar vi med pulser vi vet är samtidiga, och fördröjer dem genom att låta dem färdas olika långt. Eftersom ljuset färdas så otroligt fort kan vi styra väldigt små tidsskillnader genom att ändra avståndet, men det kräver fortfarande att vi kan

ändra det på några nanometer (miljarddelars meter) när.

En del av mitt avhandlingsarbete har också varit att rita och prova mätinstrument som hjälper oss göra dessa experiment. Tillsammans med en ökad förståelse av våra korta ljuspulser, och andra uppfinningar i vårt labb (som ett noggrant instrument för att se vilka atomer och molekyler vi har kvar efter våra reaktioner), har det förhoppningsvis bidragit till att göra framtida experiment lite lättare.

Popular science summary

The goal of the work described in this thesis is to enable studies of *dynamics in atoms and molecules*. Another way of putting it is that we want to study what atoms and molecules do on the timescale on which they do it. This happens so incredibly fast (we often speak of attoseconds, which are billionths of a billionth of a second) that the only measurement devices we have that are fast enough are light pulses we refer to as ultrashort.

In order to carry out our goal, many technical and scientific achievements are necessary. In this thesis, I will focus on two principal areas: the requirement of *short and intense* light pulses, and the need to control them very precisely in time, in what is known as *pump-probe experiments*.

Intense attosecond pulses

Why do we need *intense attosecond pulses*? First of all, we need pulses at least as fast, or short, as the phenomena under study. An old grandfather clock is beautiful, and very good at telling the time of day, but probably not suitable for timing a 100-meter sprint. However, realizing these ultrashort pulses is not trivial, so an important part of the thesis concerns how they are created using only slightly longer light pulses from high-power lasers, in a process known as high-order harmonic generation.

The pulses should not only be short, though, we want them to be intense as well. If we wish to study a process with the help of photons, i.e. light particles, the amount of "measurements" we can do in a given amount of time naturally depends on how many photons are available to us in this time. Some experiments require an atom to absorb two photons at once (or within a millionth of a billionth of a second!) and in these cases we need so many photons that this becomes a regular event.

One limiting factor to how intense our pulses can be is how well they can be focused. In the same way that sunlight can start a fire when focused through a looking glass, focusing our ultrashort laser pulses makes it possible to study entirely new kinds of phenomena.

An important part of my thesis work has thus been, apart from studying the creation of these ultrashort pulses, to examine how we can focus them effectively, and which of their properties need to be taken into account to enable this.

Multiple pulses: pump-probe experiments

We now know how to create very short pulses, but how can we use them? To learn more about the world of atoms and molecules, and the short timescales in this world, we need a reference. For instance, we cannot now the duration of an event if we do not know when it starts and when it ends.

To take an example that often came up during the writing of this thesis, I like my tea with a splash of milk. I don't know how the tea is "supposed to" taste without the milk, I only find out after I

have added it if it tastes right. Once I have added the milk, the tea cools to the point where it is no longer brewing.

This poses a problem for me. I want to determine the duration of a process (the tea brews to an agreeable flavor) but I can only perform one "measurement", at which point I am left with under-, over-, or perfectly brewed tea. This is also the case for many physical phenomena, we can only study the aftermath of a process but cannot study it as it happens.

One thing I can do, for every cup of tea I make, is to vary the time at which I add the milk, sample the tea, and note the flavor. Starting from zero (I add the milk immediately after the tea bag) and vary the time up to, say, six or seven minutes, presumably the flavor will vary from watery, to nice, to much too bitter. This is illustrated in Figure 2 (for simplicity I will give it a flavor grade from 1-10).

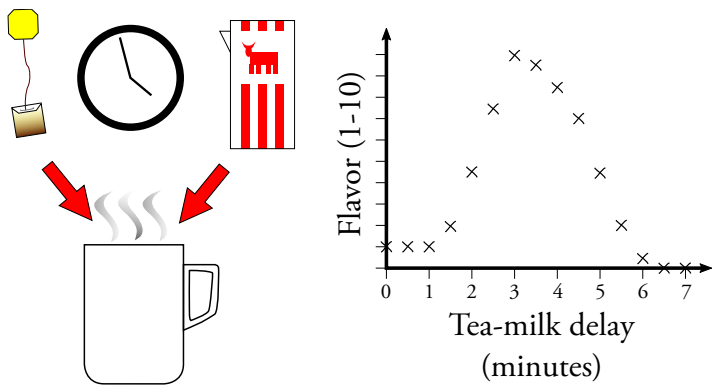

Figure 2: A simple pump-probe experiment: noting the flavor of tea as a function of when the milk is added (and the tea stops brewing).

This study is an example of a pump-probe experiment: I start a process (adding the tea bag to the hot water) and then vary the time until I perform my measurement (adding the milk and tasting the tea) to determine the duration of the process. The first step is known as the "pump" in ultrafast jargon, and the second is the "probe". By performing the same experiment several times I can thus determine the evolution of the system over time without measuring it directly.

The same technique has proven highly useful for many experiments in physics and chemistry. Our instruments are not fast enough to resolve the events that occur, but we can use two pulses and study the effects of varying their relative delay.

For example, if we know that a reaction results in the fragmentation of a molecule, we can start the reaction with one light pulse, and send in another one with a slight delay to investigate the effects. The probe pulse may, for example, have an energy corresponding to an energy level present in one of the fragments but not in the unfragmented molecule. By measuring the response from this fragment as a function of the delay between our pulses we can measure the duration of the fragmentation.

As we are dealing with very small delays, we cannot create separate pulses and hope they reach our target roughly simultaneously. Instead we start off with pulses we know are simultaneous and

introduce a relative delay by letting them propagate for varying distances. Thanks to the incredible speed of light we can use the distances to control extremely small delays. This, however, still requires a precision on the order of a few nanometers (billionths of a meter).

Part of my thesis work has consisted in designing and testing instruments that allow us to perform these kinds of experiments. Along with an improved understanding of our ultrashort light pulses and other innovations in our lab (such as an accurate instrument to determine what atoms and molecules remain after our reactions), this will hopefully make future experiments a little easier.

List of publications

The thesis is based on the following publications, referred to by their Roman numerals:

I **Two-photon double ionization of neon using an intense attosecond pulse train**

B. Manschwetus, L. Rading, F. Campi, S. Maclot, H. Coudert-Alteirac, J. Lahl, **H. Wikmark**, P. Rudawski, C. M. Heyl, B. Farkas, T. Mohamed, A. L'Huillier, and P. Johnsson
Physical Review A **93**, 061402 (2016)

II **The ELI-ALPS facility: The next generation of attosecond sources**

S. Kühn, M. Dumergue, S. Kahaly, R. Lopez-Martens, M. Fule, T. Csimadia, F. Calegari, M. Devetta, F. Frassetto, E. Månsson, L. Poletto, S. Stagira, C. Vozzi, M. Nisoli, S. Maclot, P. Johnsson, C. L. Arnold, C. M. Heyl, F. Campi, **H. Wikmark**, B. Manschwetus, M. Miranda, P. Rudawski, A. L'Huillier, E. Skantzakis, N. Papadakis, C. Kalpouzos, P. Tzallas, F. Lépine, D. Charalambidis, K. Varju, K. Osvay, and G. Sansone
Journal of Physics B: Atomic, Molecular and Optical Physics **50**, 13 (2017)

III **Micro-focusing of broadband high-order harmonic radiation by a double toroidal mirror**

H. Coudert-Alteirac, H. Dacasa, F. Campi, E. Kueny, B. Farkas, F. Brunner, S. Maclot, B. Manschwetus, **H. Wikmark**, J. Lahl, L. Rading, J. Peschel, B. Major, K. Varjú, G. Dovillaire, P. Zeitoun, P. Johnsson, A. L'Huillier and P. Rudawski
Applied Sciences **7**, 11 (2017)

IV **A versatile velocity map ion-electron covariance imaging spectrometer for high intensity XUV experiments**

L. Rading, J. Lahl, S. Maclot, F. Campi, H. Coudert-Alteirac, B. Oostenrijk, J. Peschel, **H. Wikmark**, M. Gisselbrecht, and P. Johnsson
Applied Sciences **8**, 6 (2018)

V **Spatiotemporal coupling of attosecond pulses**

H. Wikmark, C. Guo, J. Vogelsang, P. W. Smorenburg, H. Coudert-Alteirac, J. Lahl, J. Peschel, P. Rudawski, H. Dacasa, S. Carlström, S. Maclot, M. B. Gaarde, P. Johnsson, C. L. Arnold and A. L'Huillier
Proceedings of the National Academy of Sciences **116**, 11 (2019)

VI **Single-shot extreme-ultraviolet wavefront measurements of high-order harmonics**

H. Dacasa, H. Coudert-Alteirac, C. Guo, E. Kueny, F. Campi, J. Lahl, J. Peschel, **H. Wikmark**, B. Major, E. Malm, D. Alj, K. Varjú, C. L. Arnold, G. Dovillaire, P. Johnsson, A. L'Huillier, S. Maclot, P. Rudawski, and P. Zeitoun
Optics Express **27**, 3 (2019)

Acronyms

ADK Ammosov-Delone-Krainov.

APT Attosecond Pulse Train.

ARCNL Advanced Research Center for Nanolithography.

ATI Above-Threshold Ionization.

CCD Charge-Coupled Device.

CDI Coherent Diffraction Imaging.

CEP Carrier-Envelope Phase.

CPA Chirped-Pulse Amplification.

DM Deformable Mirror.

ELI-ALPS Extreme Light Infrastructure - Attosecond Light Pulse Source.

FEL Free-Electron Laser.

FFT Fast Fourier Transform.

FWHM Full Width at Half Maximum.

GDD Group Delay Dispersion.

HHG High-order Harmonic Generation.

IR Infrared.

LLC Lund Laser Centre.

LOA Laboratoire d'Optique Appliquée.

MCP Multi-Channel Plate.

MLM Multi-Layer Mirror.

Nd:YAG Neodymium-doped Yttrium-Aluminium Garnet.

OPCPA Optical Parametric Chirped-Pulse Amplification.

RABBIT Reconstruction of Attosecond Beating By Interference of Two-photon transitions.

REMI Reaction Microscope.

RMS Root Mean Square.

SDU Split-and-Delay Unit.

SFA Strong Field Approximation.

TDSE Time-Dependent Schrödinger Equation.

TOF Time-Of-Flight.

UV Ultraviolet.

VMIS Velocity Map Imaging Spectrometer.

VUV Vacuum Ultraviolet.

WFS Wavefront sensor.

XUV Extreme Ultraviolet.

Contents

Thesis

Chapter 1

Introduction

In this introduction the subject matter of the present thesis, studying the spatial and temporal aspects of intense attosecond pulses for their use in pump-probe experiments, is presented, and the case for its utility is made. Following this is a brief outline of the two parts of the present thesis.

1.1 Motivation for the work

In order to advance the understanding of the fundamental chemistry and physics of atoms and molecules, it is important to have the right tools. To be useful, the tools will need to match the object, or process, of study in spatial and temporal resolution.

1.1.1 Who cares about atoms?

Physics, like natural sciences in general, often plays a role in society whether one is aware of it (or believes in it) or not. Many technologies that are now more or less taken for granted rely on concepts that were unheard of or untested a century ago: the development of transistors required an insight into the quantum mechanical view of solid-state physics [1], and the atomic clocks synchronizing time signals throughout the world would not exist without the knowledge of advanced spectroscopy techniques as well as atomic physics phenomena such as the hyperfine splitting of cesium-133 [2, 3].

The use for humanity of inventions such as the transistor is immeasurable, but as there is often a lag between a discovery and its application it is hard to determine the utility of many current scientific endeavors, other than the obvious: that furthering our knowledge of the world is to some extent a goal in itself.

However, some conjectures can be made, based on the known utility and applications of similar technologies and scientific concepts. Advancing the understanding of the way atoms and molecules interact often carries over into the chemistry and physics of molecules and materials. This in turn

can lead to a "ripple effect" into all the fields that build upon this knowledge (as wide-ranging as materials science, medicine, electronics and fuel research). It is thus not an entirely unreasonable assumption that there is great practical utility, albeit some time into the future, of studying something as seemingly fundamental as electronic and nuclear dynamics in atoms and molecules.

1.1.2 Ultrafast experiments

Many areas of interest in physics, chemistry, and other fields that build on conclusions from these disciplines require the study of very fast, or short-lived, phenomena involving electronic and nuclear motion in atoms and molecules [4]. These phenomena may occur on timescales so short that the extent of their shortness easily overcomes our understanding. To use a well-worn analogy, one second relates to an attosecond (24 attoseconds is the so-called atomic unit of time) roughly as the age of the universe relates to one second.

In measuring the fastest phenomena, we are limited by the speed of our measurement instruments. To use an example from electronics, some of the fastest commercially available oscilloscopes have a sampling frequency of 240 GS/s [5], meaning that they can at best measure a duration on the order of 0.004 nanoseconds (4 picoseconds, or 4 000 000 attoseconds). While it is certainly possible (and likely) for measurement electronics to improve somewhat, our area of research revolving around electron motions means that there is a certain difficulty, timescale-wise, in trying to use (indirect) electron motions to directly measure (comparatively simple) electron motions.

Thus, measurement techniques have emerged that use events even faster than the motion of electrons: *ultrashort light pulses*. However, simply being fast is not enough, the finest checks on a yard stick do no good if we do not know where to place it. Thus we enhance our toolbox by using two pulses and precisely controlling the distance, or delay, between them. This is known as the pump-probe technique; the *pump* pulse starts a reaction or event, and the *probe* pulse arrives to discern the status of the event. By tuning the delay between these two pulses, we can determine the evolution in time of the event we have started. In order to perform a successful pump-probe experiment, however, many things need to fall into place. We must have *spatial* and *temporal* control of our two pulses, as well as spatial and temporal control of the target we are interested in.

1.2 Scope of the thesis

1.2.1 Short pulses and wavelengths

As will be explained in the next chapter, short light pulses often have central frequencies much higher, or wavelengths much shorter, than those of the visible light for which most optical designs were originally conceived.

Light of shorter wavelengths than visible light is referred to as Ultraviolet (UV). There are subdivisions in this as well; when the wavelength is below 200 nm the light is referred to as Vacuum Ultraviolet (VUV) due to the fact that it can only propagate for longer distances in vacuum. Its photon energy is so high that it ionizes the gases in the air, thus becoming absorbed very quickly. Light of even shorter wavelength is referred to as Extreme Ultraviolet (XUV), and it is found on the border between UV light and X-ray radiation.

The characteristics of XUV light mean that in many respects it must be treated differently from the Infrared (IR) and visible light used in many laser labs. The generation of this XUV light, through the process of High-order Harmonic Generation (HHG), results in ultrashort attosecond pulses and has been an important part of this thesis work.

In order to use the generated pulses to resolve ultrafast dynamics, the thesis work has also involved the construction of an interferometer enabling pump-probe experiments.

1.2.2 Spatial characteristics and spatiotemporal coupling

Any experiment that involves several photons interacting with the same target must take into account the cross sections, or probabilities, of the transitions or events under study. Even the simplest multiphoton interaction, two-photon excitation [6], could not be experimentally studied until the invention of the laser [7, 8]. An important reason for the higher intensity enabled even by the earliest lasers is the high degree of spatial coherence of the light produced by most lasers.

Many experiments performed today require intensities orders of magnitude higher than those of the early multiphoton studies. These intensities require short and energetic pulses, focused into small areas, i.e. the pulse must be temporally coherent in order to maintain a high peak power, and spatially well-defined to enable as small a focus as possible.

The exotic properties of our short wavelength light, however, require the focusing optics to be realized and used in a very deliberate way so as not to introduce wavefront aberrations that deteriorate the quality of the focus, ruining the important intensity.

Another effect comes from the HHG process itself. As discussed in this thesis, the process may lead to chromatic aberrations and spatiotemporal coupling, where the focus is not homogeneous in space and time.

A large part of this thesis work has been devoted to studying the spatial properties of the harmonics, how they depend on the generation process, and their interaction with the focus and focusing optics.

1.3 Thesis outline

The present thesis consists of two parts. The first part aims to explain and expand on the ideas and results presented in the Papers included in the second part.

The first part consists of five chapters, following this one. These chapters provide a background and explanation for the work presented, the experimental methods and equipment used, and the results of the experiments performed as part of this thesis work. Taken together, they will show various spatial and temporal aspects of ultrashort XUV pulses, and how their properties can be measured and controlled.

The first part is concluded by a summary of what has been discussed, as well as an outlook that sheds light on ongoing and future endeavors connected to this work.

Chapter 2

High-order harmonic generation in gases

Since its discovery in the late 1980s, the generation of high-order harmonics has been a hot topic in the field of nonlinear optics [9, 10]. The general understanding of the phenomenon on a single-atom level started with the so-called three-step model [11], which was soon justified from a quantum mechanical point of view with the development of the Strong Field Approximation (SFA) [12].

The understanding of the macroscopic response, i.e. taking into account phase matching and reabsorption effects in an extended generation medium, was developed in parallel [13]. The parameters derived from the macroscopic response were important factors in the development of a theory of scaling harmonic generation [14], which, along with the design principles of the Lund Laser Centre (LLC) intense harmonic beamline, also played a role in the design of the Lund-designed LONG GHHG beamline [15], described further in Paper II and Section 3.7.

This chapter will begin by showing the use for high-order harmonic generation as a source of high-frequency, broadband, ultrashort light pulses. Following this is a brief overview of the theory of HHG in gases, from the single-atom response to the macroscopic response of the generation medium.

2.1 Background - ultrashort pulses

As mentioned in the introduction, the shortest events mankind can create (or at the very least control) are ultrashort light pulses [16]. The duration of the light pulse itself naturally determines the fastest, or most shortest-lived, event that the pulse can be used to study.

There is, however, a fundamental limit to how short a pulse can be. Because of the Fourier transform relation between the time and frequency representations of a light pulse, its duration (i.e. "shortness") has a lower bound given by the so-called time-bandwidth product. For a Gaussian pulse (in

time) with a duration at Full Width at Half Maximum (FWHM) τ and FWHM bandwidth $\Delta\nu$ this product is

$$\tau\Delta\nu = 0.44. \tag{2.1}$$

This means that for a pulse to be sufficiently short, it needs to be very broadband. As an example, a Gaussian pulse with a FWHM pulse length of 1 fs needs a bandwidth of 440 THz, or more than the entire visible spectrum (approximately 400 to 750 THz). In order for the pulse to support this bandwidth, the central frequency must be sufficiently high.

2.1.1 Spectral phase and dispersion

Unfortunately, while necessary for a short pulse duration, a large bandwidth by itself is not sufficient. The phase of the pulse must also be taken into account. To study this, it is helpful to perform a Taylor expansion of the spectral phase. Around a central frequency ω_0 the expression becomes

$$\Phi(\omega) = \Phi_0 + \Phi_0'(\omega - \omega_0) + \frac{1}{2!}\Phi_0''(\omega - \omega_0)^2 + \frac{1}{3!}\Phi_0'''(\omega - \omega_0)^3 + ... \tag{2.2}$$

where Φ_0 is the absolute phase and Φ_0', Φ_0'', and so on are the n:th order derivatives of $\Phi(\omega)$ at $\omega = \omega_0$.

The absolute phase is the so-called Carrier-Envelope Phase (CEP). For extremely short pulses (only a few optical cycles in length), this becomes significant [17] but for sufficiently long pulses (as an example, the main laser system used in this thesis work has a pulse duration of around 40 fs, or 15 cycles), the envelope is sufficiently long in comparison to the cycle length that one may use the so-called slowly-varying envelope approximation, meaning that CEP effects can be neglected [18].

The first-order derivative of the spectral phase is known as the group delay. Since the phase varies linearly with the frequency, it corresponds to a temporal displacement of the whole pulse. As there is often no fixed start point in time other than that defined by the pulse itself[1], this feature does not influence the temporal *structure* of the pulse.

The second-order derivative is referred to as the Group Delay Dispersion (GDD). GDD and higher-order dispersion terms (derivatives of the spectral phase) are responsible for distorting the temporal structure of the pulse. If these terms are significant, the pulse is said to be frequency-modulated or chirped. Figure 2.1 shows two pulses in the time and frequency domains.

If the spectral phase is purely quadratic, the instantaneous (time-dependent) frequency is linearly dependent on time, and the pulse is thus referred to as linearly chirped. This can be seen in Figure 2.1 (d), where the electric field of a pulse with quadratic spectral phase is shown in the time domain; the higher-frequency components appear earlier in time than the lower-frequency components.

A pulse without any spectral phase is referred to as transform limited (its duration is only limited by the time-bandwidth product).

[1] See Section 6.1 for an overview of how the time can be defined by the pulse.

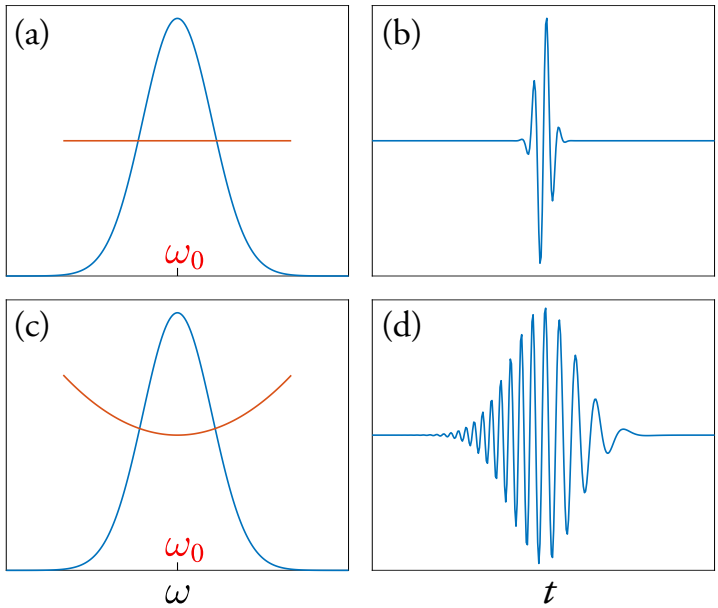

Figure 2.1: (a) The amplitude (blue) and phase (red) of frequency components of a broadband, transform-limited pulse, (b) The **E**-field of the same pulse in the time domain. (c,d) the frequency- and time domain pictures of a pulse with a linear chirp.

2.1.2 Chirped pulse amplification

An obstacle that appears when high intensity, ultrashort pulses are created is damage in the gain medium, caused by nonlinear effects such as self-focusing when an intense pulse propagates through the medium [19]. One solution for this is called Chirped-Pulse Amplification (CPA) [20] and led to its inventors, Donna Strickland and Gérard Mourou, being awarded the 2018 Nobel Prize.

The main point of the technique is to stretch the pulse temporally (i.e. chirping it) and then amplify it. After the pulse energy has been increased, the pulse can be compressed again using reflection gratings or chirped mirrors. The advantage is that the compression can be done without transmissive optics, so there is no medium that is damaged by the high pulse energy.

The laser used for all experiments in this thesis work (as described in Section 3.1) relies on the CPA principle, as do most high-power, ultrafast lasers in the world.

2.1.3 High-order harmonics as ultrashort pulses

Due to the previously mentioned time-bandwidth product, it is clear that high-order harmonics, as high-frequency, broadband pulses, have characteristics appropriate for ultrashort pulses. When HHG was first discovered it was quickly theorized that these pulses could be even shorter than the laser pulses used to generate them [21], which was confirmed in 2001 by cross-correlating the

harmonics with the generating field [22], employing the technique now known as Reconstruction of Attosecond Beating By Interference of Two-photon transitions (RABBIT).

2.2 The single-atom response

2.2.1 The three-step model

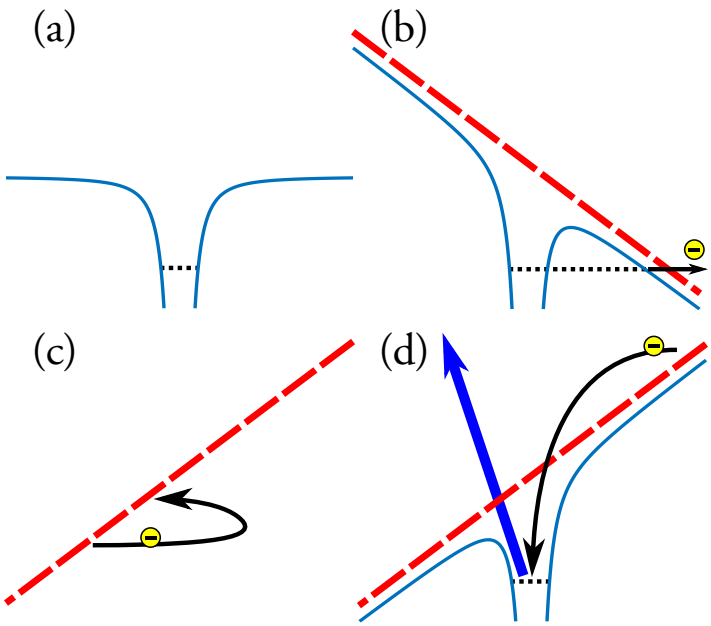

Figure 2.2: An illustration of the three-step model: (a) An atomic potential with a bound electron, (b) distortion of the potential and tunnel ionization, (c) the electron propagating in the oscillating field, and (d) recombination and emission of a high-energy photon.

The three-step model starts with the assumption that a strong laser field will distort the potential of an atom or molecule, allowing an electron to tunnel out (step 1, **ionization**). When the electron is free from the potential it travels as a free particle in the **E**-field of the laser (step 2, **propagation**). As the **E**-field oscillates with the frequency of the laser, there is a possibility for the electron to return to its parent ion, at which point its excess energy, the sum of its kinetic energy and the potential energy of the ion, is released as a high-energy photon (step 3, **recombination**). Figure 2.2 illustrates this process.

Ionization

High-order harmonic generation in gases generally assumes very strong laser fields and photon energies much smaller than the ionization potential of the medium, leading to a preference for tunneling

ionization over other multiphoton processes [23]. The time-dependent electric field $\mathbf{E}(t)$ can be seen as a periodic modulation of the electric field amplitude E_0, which is related to the field intensity as

$$I = \frac{1}{2}\epsilon_0 c|E_0|^2, \tag{2.3}$$

where ϵ_0 is the vacuum permittivity and c the speed of light in vacuum. The laser intensities used in HHG typically range from 10^{14} W/cm^2 to 10^{15} W/cm^2, corresponding to field strengths of around 30 to 90 GV/m.

Propagation

Once the electron has left the atomic potential, it is assumed to travel freely in the field of the laser. Its motion can be estimated by following the classical propagation in one dimension, chosen as x, of a charged particle in an oscillating electric field:

$$F_x(t) = eE_x(t) = -eE_0 \sin(\omega t), \tag{2.4}$$

where e is the fundamental unit of charge ($1.609 \cdot 10^{-19}$ C) and ω is the driving field frequency, leading to an acceleration of

$$a_x(t) = \frac{-eE_x(t)}{m_e}, \tag{2.5}$$

with m_e being the electron mass. Integrating the time-dependent acceleration from the ionization time t_i to the recombination time t_r yields the velocity at t_r as

$$v_x(t_r) = \int_{t_i}^{t_r} a_x(t)dt = \frac{-eE_x(t)}{m_e\omega}\left[\cos(\omega t_r) - \cos(\omega t_i)\right]. \tag{2.6}$$

The velocity can then be integrated to give the x position at t_r as

$$x(t_r) = \int_{t_i}^{t_r} x(t)dt = \frac{-eE_x(t)}{m_e\omega^2}\left[\sin(\omega t_r) - \sin(\omega t_i) - \omega(t_r - t_i)\cos(\omega t_i)\right]. \tag{2.7}$$

The result of this equation, assuming a fundamental laser field strength of 33 GV/m ($I \approx 3.3 \cdot 10^{14}$ W/cm^2) and a wavelength of 800 nm, can be seen in Figure 2.3, which shows the x position over time of an electron, depending on t_i. t_r can thus be determined as the time in which x returns to 0 (the parent ion) again. As seen in the figure, this recombination does not happen for all trajectories (the gray, dashed trajectories are those where the electron does not return).

Once t_r is established, the return energy of the electron can be calculated using the velocity $v(t_r)$, and the classical kinetic energy $E = mv^2/2$, as

$$E_r = \frac{m_e v(t_r)^2}{2} = \frac{E_0^2 e^2}{2m_e\omega^2}\left[\cos(\omega t_r) - \cos(\omega t_i)\right]^2, \tag{2.8}$$

or in terms of the ponderomotive energy U_p,

$$E_r = 2U_p\left[\cos(\omega t_r) - \cos(\omega t_i)\right]^2. \tag{2.9}$$

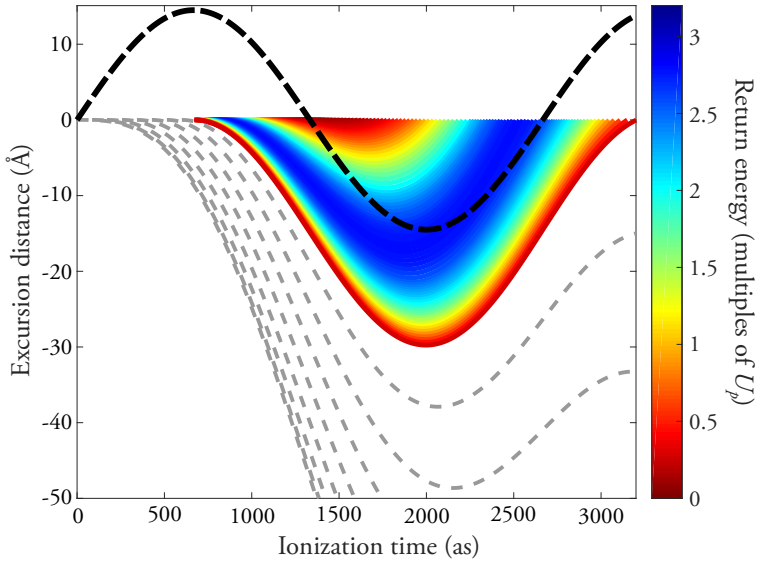

Figure 2.3: The trajectories of an electron in an oscillating laser field, as a function of ionization time t_i. The colors of the trajectories correspond to the return energy, with blue being the highest and red the lowest. The dashed gray trajectories are those that do not lead back to the parent ion. The fundamental field over time is illustrated by the dashed black sinusoidal.

defining it as

$$U_p = \frac{e^2 E_0^2}{4 m_e \omega^2}. \tag{2.10}$$

An alternative way of stating this is

$$U_p = \frac{\alpha_{\mathrm{FS}} \hbar I \lambda^2}{2\pi c^2 m_e} \tag{2.11}$$

where α_{FS} is the fine structure constant and λ is the fundamental wavelength.

Recombination

The ionization time dependent return times and return energies are provided in Figure 2.4. As can be seen, the calculated maximum energy is 3.17 U_p, to which one can add the I_p of the generation medium, thus leading to a highest, or "cutoff", energy of

$$E_c = I_p + 3.17 U_p. \tag{2.12}$$

Before and after the cutoff trajectory, one can identify two families of trajectories as the long and short trajectories, respectively. The short trajectories have t_i after the cutoff and are shown above the darkest blue line in Figure 2.3. The long trajectories ionize before the maximum energy trajectory and are shown below it in the plot.

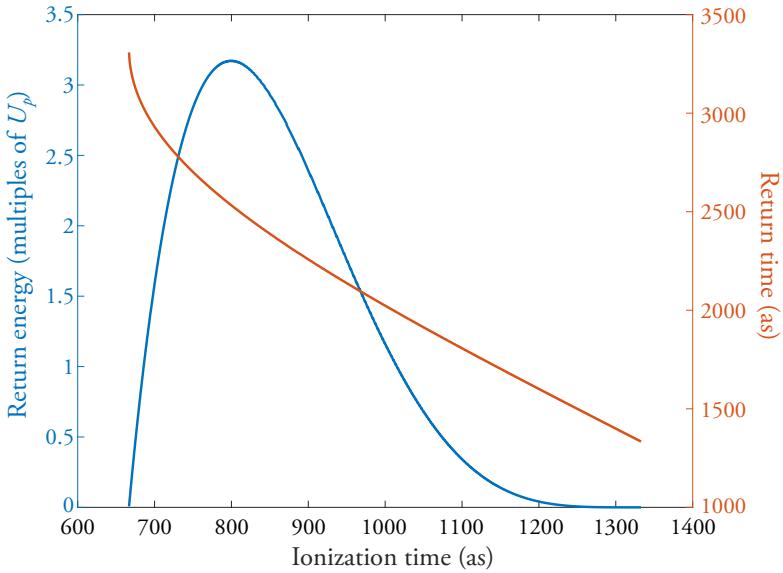

Figure 2.4: The return energy E_r (blue) and return time t_r (red) as a function of the ionization time t_i.

Table 2.1: Ionization and return times for the electron trajectories in Figure 2.3.

Time	Time (fs) for 800 nm laser	Cycles (T)
t_i, non-returning	$0 < t < 0.66$	$0 < t < T/4$
t_i, long trajectories	$0.66 < t < 0.8$	$T/4 < t < T/3$
t_i, short trajectories	$0.8 < t < 1.33$	$T/3 < t < T/2$
t_r, short trajectories	$1.33 < t < 2.53$	$T/2 < t < 0.95\ T$
t_r, long trajectories	$2.53 < t < 3.3$	$0.95\ T < t < 5/4\ T$

Table 2.1 lists the ranges of approximate ionization and return times that define the trajectories, in femtoseconds for the previously mentioned laser characteristics as well as in laser cycles T for a sinusoidal field (i.e. $\omega T = 2\pi$).

2.2.2 Harmonic cutoff

The high photon energies of the harmonics, as mentioned in the introduction, are fundamental to the temporal structure of the pulse (a large bandwidth around a high central frequency), but can also be seen as an end in themselves. For spectroscopy, they may allow for addressing otherwise unavailable energy levels [24]. For many biological applications, it is useful to produce photons in the so-called water window, where the absorption of water rapidly drops [25]. Thus an important question is how to extend the cutoff of the harmonic spectrum.

For the calculations shown in the previous section, U_p is approximately 18 eV, implying that the

second term in Equation (2.12) is a more important factor than I_p (ranging from $\sim 10 - 20$ eV for the noble gases) if one is interested in a high cutoff (producing high-energy photons).

However, selecting a medium with a higher I_p leads to a rapidly decreasing ionization rate. In order to estimate this, the so-called Ammosov-Delone-Krainov (ADK) equation can be applied to calculate the time-dependent tunneling rate from a varying electric field $E(t)$ as [26, 27]:

$$\Gamma(t) = 4\omega_0 \left(\frac{I_p}{I_\mathrm{H}}\right)^{5/2} \frac{E_a}{E(t)} \exp\left[-\frac{2}{3}\left(\frac{I_p}{I_\mathrm{H}}\right)^{3/2} \frac{E_a}{E(t)}\right], \tag{2.13}$$

where $\omega_0 = 6.8 \cdot 10^{15}$ Hz is the atomic frequency unit, I_p is the ionization potential of the element used, $I_\mathrm{H} = 13.6$ eV is the ionization potential of hydrogen, and $E_a = 5.14 \cdot 10^{11}$ V/m is the atomic unit of the electric field. Through this equation, it can thus be seen that there is a strong dependence of the field strength, and this dependence varies with the ionization potential of the medium.

While this means a lower harmonic yield for a medium with a higher I_p, it also means that the driving laser intensity can be increased further without saturating the medium (depleting the ground state), which leads to a much greater increase in U_p than the relatively small increase in the ionization potential [10]. The question of yield will be discussed further in the next section on macroscopic effects.

2.2.3 Even and odd harmonics

This thesis work has dealt with HHG in gases. While some (variably) similar descriptions can be made of HHG in other media, such as crystals [28], plasma mirrors [29], and more esoteric structures [30], particularities of these cases are not discussed further. One interesting characteristic of HHG in gases is that in most cases, it only yields odd harmonic orders.

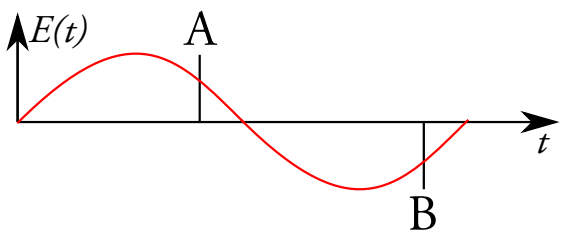

Figure 2.5: The E-field of the fundamental beam in time, featuring two points A and B, separated by $T/2$.

One way to explain this is with the isotropicity of the medium. Considering two points A and B, as shown in Figure 2.5, that are separated by $T/2$ (in opposite phase), the time-dependent field $E(t)$ at the two points can be expressed as

$$E(\mathrm{A}) = -E(\mathrm{B}), \tag{2.14}$$

and the polarization of the medium thus induced is

$$P(E(\mathrm{A})) = -P(E(\mathrm{B})), \tag{2.15}$$

while any even-ordered nonlinear process $\chi^{(2n)}$ yields a polarization as

$$P(E(t)) = \chi^{(2n)} E(t)^{2n}. \tag{2.16}$$

It is then apparent that the only solution to the two equations is that $\chi^{(2n)} = 0$, $\forall n$. Thus, as long as the medium is isotropic and the half-cycle periodicity of the field is maintained [31], even harmonic orders will be suppressed. In this case, the harmonics are emitted every half-cycle in what is known as a train of attosecond pulses, or an Attosecond Pulse Train (APT).

2.2.4 The Strong Field Approximation

Shortly after the three-step model, a fully quantum mechanical model for HHG was realized in the SFA [12]. The model is based on solving the Time-Dependent Schrödinger Equation (TDSE). In order to simplify the solution of the equation, several assumptions are made that greatly reduce the number of possible interactions that need to be taken into account:

- The electron propagates freely in the continuum, i.e. the laser field is so strong that the electron is not affected by the atomic potential after ionization.
- The ground state is not depleted, signifying that the intensity is not so high as to completely ionize the generation medium.
- Only the ground state interacts in a meaningful way with the continuum state, no excited states are assumed to contribute to the generation process.

Used in conjunction with other approaches such as the saddle-point approximation and the single active electron approximation [13], the fully quantum mechanical model for harmonic generation can thus be calculated numerically in a computationally efficient manner.

2.2.5 The dipole phase

One important conclusion of studying the single-atom response is that different frequencies are generated (i.e., the electron returns creating them take place) at different times, in addition to the varying return times of the long and short trajectories.

This time-dependent frequency of the attosecond pulse, in the terminology of Section 2.1.1, constitutes a chirp. It is often referred to as the "attochirp", and sets a limit on the duration of attosecond pulses [32]. However, the impact of this order-dependent emission time on the phase of the emitted harmonics, known as the dipole phase, has other interesting properties, which are discussed in this section.

The dipole phase term has often been parametrized as αI, a consequence of its derivation from the Strong Field Approximation [12]. An alternative way of stating this phase component can be found in [33, 34] and is based on deriving a frequency- and intensity-dependent phase from the three-step model (as described in section 2.2.1).

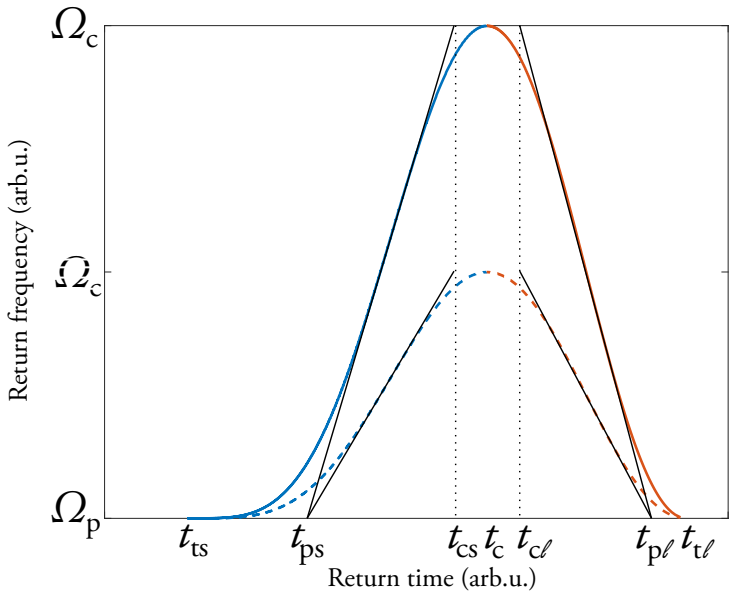

Figure 2.6: The frequency of harmonics as a function of the return time, showing the straight lines of the "model" and that these lead to the same times t_{pi} and t_{ci} for two different intensities, shown as full and dashed lines. The short and long trajectories are marked in blue and red, respectively.

Figure 2.6 shows the two y-axes of Figure 2.4 plotted against each other, i.e. the return energy as a function of the return time. The return energy is then converted into frequency ($\Omega = E/\hbar$) for the benefit of the following discussion. The times t_c and t_{ti} symbolize the return time of the cutoff harmonics (which is the same for both trajectories) and the trajectory-dependent ($i = s, \ell$) threshold return time (i.e., the time giving the lowest return frequency, meaning the first of the long trajectories and the last of the short ones).

By approximating the return-time-dependent frequency by a straight line, which can be shown to be a reasonable assumption along the plateau harmonics, this can be inverted from $\Omega(t)$ to $t(\Omega)$ to yield the frequency-dependent return time t_{ri}

$$t_{ri}(\Omega) = t_{pi} + \frac{t_{ci} - t_{pi}}{\Omega_c - \Omega_p}(\Omega - \Omega_p), \tag{2.17}$$

where t_{pi} is the threshold time, t_{ci} is the cutoff time, both defined by the straight lines shown in Figure 2.6, and Ω_p and Ω_c are the frequencies at the threshold and cutoff, respectively.

Assuming a constant (not frequency dependent) time for tunneling and recombination, $t_{ri}(\Omega)$ can be seen as the group delay of the harmonics, and thus its integral is the spectral phase

$$\Phi_i(\Omega) = \Phi_i(\Omega_p) + t_{pi}(\Omega - \Omega_p) + \frac{t_{ci} - t_{pi}}{\Omega_c - \Omega_p}\frac{(\Omega - \Omega_p)^2}{2}. \tag{2.18}$$

Since $\Omega_c - \Omega_p = 3.17 U_p/\hbar$ and U_p (as stated in Equation (2.11)) is proportional to the intensity,

the last term can be rewritten, yielding

$$\Phi_i(\Omega) = \Phi_i(\Omega_\mathrm{p}) + t_{\mathrm{p}i}(\Omega - \Omega_\mathrm{p}) + \frac{\gamma_i}{I}(\Omega - \Omega_\mathrm{p})^2 \tag{2.19}$$

where

$$\gamma_i = \frac{(t_{ci} - t_{\mathrm{p}i})\pi c^2 m_e}{3.17\alpha_\mathrm{FS}\lambda^2}. \tag{2.20}$$

The term $\Phi_i(\Omega_\mathrm{p})$ is equivalent to the SFA-derived $\Phi_\ell(\Omega_\mathrm{p}) = \alpha_\ell I$ for the long trajectories, while it is 0 for the short trajectories (i.e. $\alpha_\mathrm{s} = 0$).

2.3 The macroscopic response

The single-atom response, while useful in itself, does not accurately estimate the yield of high-order harmonics, or their spatial properties. One also needs to take into account macroscopic effects, which emerge when the pulses are generated in a finite medium.

2.3.1 Phase-matching

Seen along the propagation axis, the main macroscopic effect to take into account is phase-matching, which refers to whether or not the a fields of a given harmonic, generated in different parts of the medium, are in phase with one another. If the fundamental field and the harmonics propagate differently through the medium, and the medium has a finite length, it is very likely that they are not, and since the two fields have dramatically different wavelengths it is not unreasonable to expect different properties of propagation. For the process to be as efficient as possible it can be assumed this *wavevector mismatch* should be minimized.

The total wavevector mismatch for the qth harmonic can be described as [14]

$$\Delta\mathbf{k}(q) = q\mathbf{k} - \mathbf{k}_q \tag{2.21}$$

where $\mathbf{k}$ is the fundamental field wavevector, and the total wavevector mismatch can be described using four terms as

$$\Delta\mathbf{k}(q) = \Delta\mathbf{k}_g + \Delta\mathbf{k}_n + \Delta\mathbf{k}_p + \Delta\mathbf{k}_d \tag{2.22}$$

where $\mathbf{k}_g$ is the Gouy phase term, $\mathbf{k}_n$ is the contribution from neutral dispersion, $\mathbf{k}_p$ is the mismatch from plasma dispersion and $\mathbf{k}_d$ is that introduced by the dipole phase. Assuming, as previously stated, on-axis propagation, the vectors are replaced with z-dependent wavenumbers and their order-dependence is implied for the sake of simplicity.

The Gouy phase, as discussed in Section 4.1, reflects the spatial phase along the focus of a Gaussian beam [35] and goes from $-\pi/2$ at $z = -\infty$ to $\pi/2$ at $z = \infty$. The mismatch induced by the Gouy phase is [14]

$$\Delta k_g = -\frac{q}{z_0}, \tag{2.23}$$

and is thus always negative.

The dipole phase contribution to the mismatch, recalling Equation (2.19), can be calculated as

$$\Delta k_d = \frac{\partial \Phi_i(\Omega_q)}{\partial z} = \frac{\partial I}{\partial z}\left[\alpha_i - \frac{\gamma_i}{I^2}(\Omega_q - \Omega_\mathrm{p})^2\right]. \tag{2.24}$$

For the short trajectories, as discussed in Paper V, α_s reduces to 0 and γ_s is positive, leading to a mismatch which is negative before the focus ($z < 0$) and positive after the focus ($z > 0$). For the long trajectories α_ℓ and γ_ℓ are both negative but with different signs. However, α_ℓ is always greater than γ_ℓ, meaning that the dipole phase mismatch contribution is always negative.

The neutral dispersion mismatch and that caused by plasma dispersion both depend on the pressure, the plasma term also depending on the intensity in the medium (by way of the ionization rate). The plasma dispersion contribution is negative, while the neutral atom dispersion term is positive. When generating before the focus this is the only positive mismatch contribution, meaning that the generation pressure ideally can be tuned to allow this wavevector to cancel out the negative contributions.

Phase matching is never exact, however, and one must often use all available generation parameters to optimize harmonic yield, including the intensity, the pressure, and where one places the generation medium in relation to the IR focus (or vice versa).

2.3.2 Harmonic yield and scaling

Like many nonlinear optical processes [35], HHG is not an "efficient" process in the sense that a large part of the IR energy is converted into XUV light. The practical limits for efficiency in day-to-day operation of HHG sources seem to be somewhere in the region of 10^{-5}. To take a coarse example from the intense XUV beamline, this means that 100 mJ of IR light gives a maximum total energy in the APT of around 1 µJ (as described in Paper I).

In combination with the difficulties one has in manipulating light at these wavelengths (see Section 5.1), it is thus often complicated to achieve high pulse energies in the XUV. However, some efforts have been made to mitigate this.

Based on the on-axis phase matching conditions, and general propagation equations, some scaling laws for nonlinear optics have been developed [36]. While they are in principle applicable to any nonlinear processes and have been demonstrated for phenomena such as filamentation in gases, they apply well to HHG [14].

The principle of scaling is that as long as all the relevant parameters are changed according to the scaling parameter η, shown in Table 2.2, the process is scale-invariant; i.e. has the same generation efficiency and response. For example, the pulse energy scales as η^2, as does the focal length of the system, while the medium density scales as $1/\eta^2$; meaning that if one wants to generate in the same conditions for a laser pulse with 10 times the energy the focal length must be scaled up by the same amount and the generation gas pressure scaled *down* by a factor of 10.

Table 2.2: The generation parameters and their scaling properties. Adapted from [14].

Parameter	Description	Scaling with η
E	Pulse energy[a]	$E \propto \eta^2$
f	Focal length	$f \propto \eta^2$
D	Beam diameter before focusing	$D \propto \eta$
L	Medium length	$L \propto \eta^2$
ρ	Medium density	$\rho \propto 1/\eta^2$

[a] Note that this scaling of the pulse energy assumes a constant pulse duration.

The design for the LONG GHHG beamline at the Extreme Light Infrastructure - Attosecond Light Pulse Source (ELI-ALPS) facility, as described in Paper II and shown more briefly in Section 3.7, shows an extreme example of this; in order to prepare for the high pulse peak powers anticipated from future laser development, the focal length, for example, is scaled up to 55 meters.

Chapter 3

Experimental methods

The LLC intense XUV beamline was where the experiments presented in Papers I and III-VI took place, so it will be described thoroughly in this chapter. Part of this thesis work also involved the development and characterization of the beamline, especially the XUV-IR interferometer, which will be presented in some detail.

In addition to the intense XUV beamline, during this thesis work some designs were made for the LONG GHHG beamline at ELI-ALPS, which is described in detail in Paper II but will also be presented briefly at the end of this chapter.

3.1 Pump laser

Figure 3.1 shows the current layout of the terawatt laser of the LLC High Power Laser Facility [37, 38], which powers the intense XUV beamline. In addition to HHG the TW laser is also used for acceleration of protons [39] and electrons [40].

The laser system is based on a passively mode-locked titanium-sapphire oscillator [41], pumped by a frequency-doubled Neodymium-doped Yttrium-Aluminium Garnet (Nd:YAG) laser, and thus has a central wavelength around 800 nm. The oscillator has a repetition rate of around 80 MHz, which for the subsequent steps is reduced to 10 Hz by a pulse picker. The signal from a photodiode in the oscillator is used as the clock source for the subsequent synchronization of all lasers and other systems in the lab.

Before being stretched and amplified (in a CPA scheme, see Section 2.1.2), the beam is sent through a pre-amplifier. This decreases the amplification needed in later steps and thus improves the pulse contrast (the peak power of the pulse compared to the power of the leading edge). The contrast is typically above 10^8, which is many orders of magnitude higher than required for HHG, but necessary for experiments, such as particle acceleration, that take place in a stronger-field regime [42].

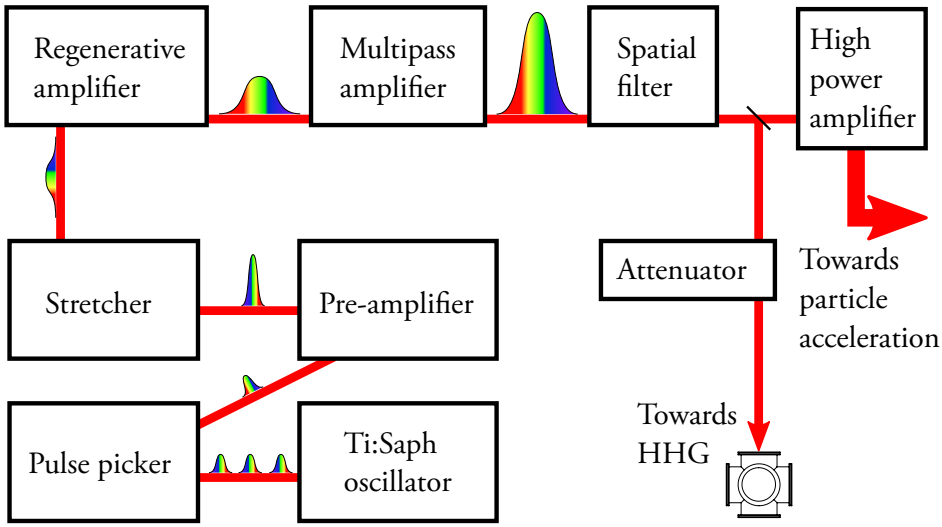

Figure 3.1: A sketch of the layout of the High Power Laser Facility terawatt laser.

Once stretched, the beam is amplified by a regenerative amplifier and subsequently by a multipass amplifier, pumped by pulsed Nd:YAG lasers with 1 J pulse energy. It is then sent through a spatial filter, in which the wavefront is cleaned up by removing high spatial frequency components in Fourier space. Practically, this is done by focusing the beam into a glass cylinder with a pinhole that admits most of the focus but clips the outermost edges.

At this stage, the laser delivers 400-mJ pulses with a bandwidth of around 37 nm, which can be compressed down to approximately 35 fs[1]. These pulses are split using a 50/50 beamsplitter. One half is employed at the high intensity XUV beamline, while the other, to be used for particle acceleration, goes through another amplification stage to increase the pulse energy by an additional order of magnitude.

The IR beam used for HHG passes through a half-wave plate and a coated glass plate at the Brewster angle, which together function as a variable attenuator, enabling continuous control of the laser power from approximately 1 to 98%.

The beam is sent from the laser room into the intense XUV beamline through a series of evacuated tubes. This is to ensure that any nonlinear propagation effects in air do not negatively affect the quality of the beam profile and the temporal phase of the pulse.

One challenge introduced by the very long beam path (as an example, from the spatial filter to the compressor the beam travels around 15 meters) is that even small deviations in angle can lead to very large displacements of the beam. For this reason, there are actuated mirrors throughout the beamline, adjusting the beam as dictated by image analysis. This can be done on the beam profile to estimate the beam position, or the focused beam to estimate the angle.

[1]Note that according to equation (2.1) a much shorter pulse length is supported, emphasizing the need to also consider factors such as higher-order dispersions of the spectral phase.

3.2 Harmonic generation

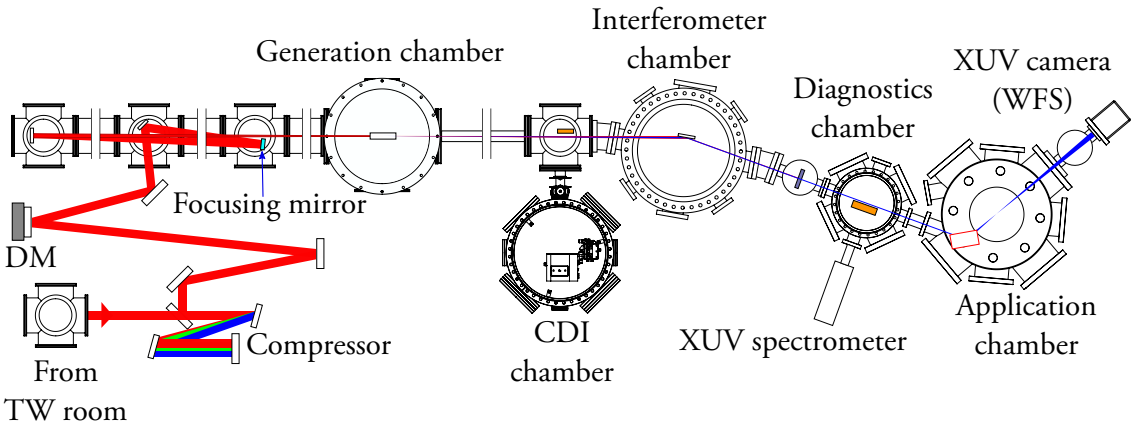

Figure 3.2: The intense XUV beamline.

Figure 3.2 shows a simplified drawing of the intense XUV beamline. The stretched pulse from the high power laser is compressed to 35 – 40 fs using two gratings and a retroreflector [20, 43]. After the beam transport and compression, the pulse energy is typically up to 100 mJ. At this stage, there are also some diagnostic instruments available including an autocorrelator, power meter and IR spectrometer.

3.2.1 Deformable mirror

The beam is reflected on a Deformable Mirror (DM) in order to correct for wavefront aberrations and change the focusing conditions (see Section 4.4 for more information on the principles of DMs).

A DM was installed at the intense XUV beamline during the course of this work, in the position shown in Figure 3.2. Figure 3.3 shows a photo of the DM as well as an iris aperture just before it. The DM was provided by AKA Optics, with control software written by NightN Optics, the designers of the mirror. Figure 3.4 illustrates the distribution of the 31 piezoelectric actuators and focusing membrane, individually controllable through the software.

The DM was used in conjunction with an IR wavefront sensor in order to improve the IR wavefront, which proved especially important when investigating the interplay between aberrations in the IR and XUV wavefronts, as described in Paper VI.

The focusing membrane (shown as actuator number 1 in Figure 3.4, but actually covering the whole surface) was used in conjunction with the focusing optics to, in effect, form a detuned telescope, which enabled a repeatable translation of the IR focus without the need for (much) realignment. This proved instrumental in the investigations of the spatial effects of the dipole phase discussed in Section 4.5.3 and Paper V.

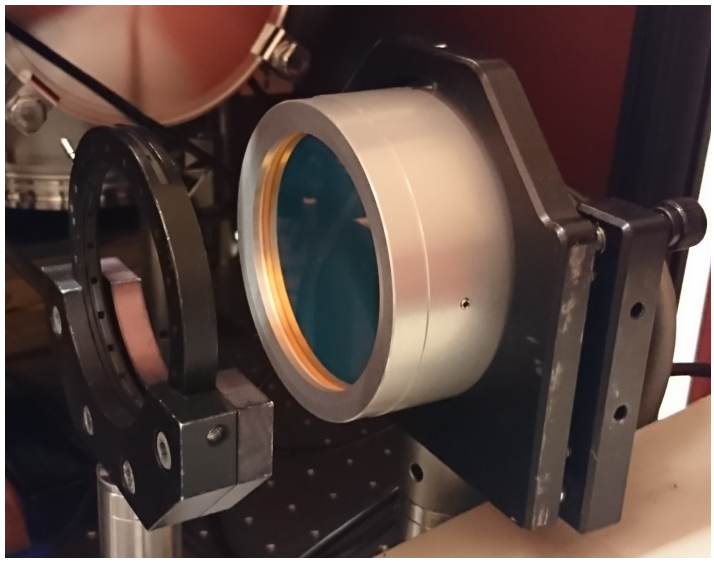

Figure 3.3: A photo of one of the DMs installed at the high-intensity XUV beamline.

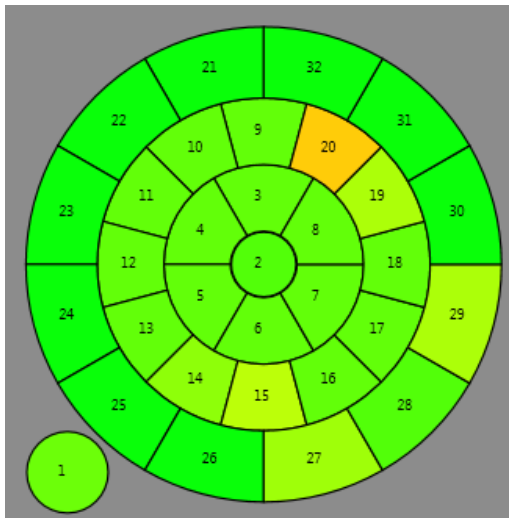

Figure 3.4: A screenshot from the NightN Optics deformable mirror software, showing a map of the available actuators on the DM used.

In order to avoid that the focusing membrane changed the beam pointing, it proved crucial to carefully align the incident beam on the center of the DM[2], as illustrated by the iris aperture in Figure 3.3.

[2] This also explains the somewhat convoluted beam path between the compressor and the DM in Figure 3.2: The pointing error induced by the DM also depends on the angle of incidence.

3.2.2 IR focus and generation medium

For the experiments described in Papers I, III and VI, the IR beam was focused by means of a plano-convex lens with a focal length $f = 8.7$ m. For subsequent experiments, including those described in Papers IV and V, the lens was replaced with a spherical mirror with $f = 8$ m.

Using these optics, the infrared beam is focused into the generation medium, which was argon for most experiments mentioned in this thesis, with some exceptions. Most notably, krypton was used for the multiphoton ionization studies described in Section 6.3.1 and Paper I.

As mentioned in section 2.3.1, the geometry of the generation medium matters greatly for the harmonic properties. For most experiments a 6 cm long gas cell was used, fed from a pulsed piezoelectric valve. In some experiments, however, cells of different lengths, e.g. 1 cm, were used.

To regulate the pressure, the peak voltage of the pulse sent to the valve, as well as the length of the pulse, could be regulated. As there was no direct measurement of the pressure in the cell, the ambient pressure of the generation chamber was used to compare the pressure for different conditions.

For Papers III and VI, the gas cell was fed continuously from the central gas line of the laboratory, through a reducer that could be used to regulate the pressure.

3.3 Interferometer chamber

After generation, the beam enters the interferometer chamber. This chamber has housed several different mirrors and mirror setups, geared towards different kinds of experiments. Drawings of these setups can be seen in Figure 3.5. In all cases, the chamber held some reflective optics for the XUV beam, as well as means of reducing the (still very high) IR pulse energy. For most experiments, 200 nm thick aluminium filters from LUXEL corporation were used to attenuate the IR.

3.3.1 Interferometer chamber configurations

I. Single silica plate

The simplest setup involved using a fused silica plate, anti-reflection coated for the IR, at a 10° angle of incidence. The reason for this very shallow angle, as discussed in Section 5.1, is to preserve the XUV reflectivity, which remains around 50% for an HHG spectrum generated in argon. The anti-reflection coating for the IR means that only a few percent of the IR energy is reflected and the rest transmitted through the glass, which means that the IR beam is at a sufficiently low power to not destroy the filters used to completely extinguish it. The filters are mounted in the small chamber after the interferometer chamber, on a vertical manipulator enabling selection of different filters and, if necessary, admitting the IR into the application chamber.

This setup was used for most of the investigations not requiring time-resolved experiments, since the simple design lead to an easy alignment and a high energy throughput.

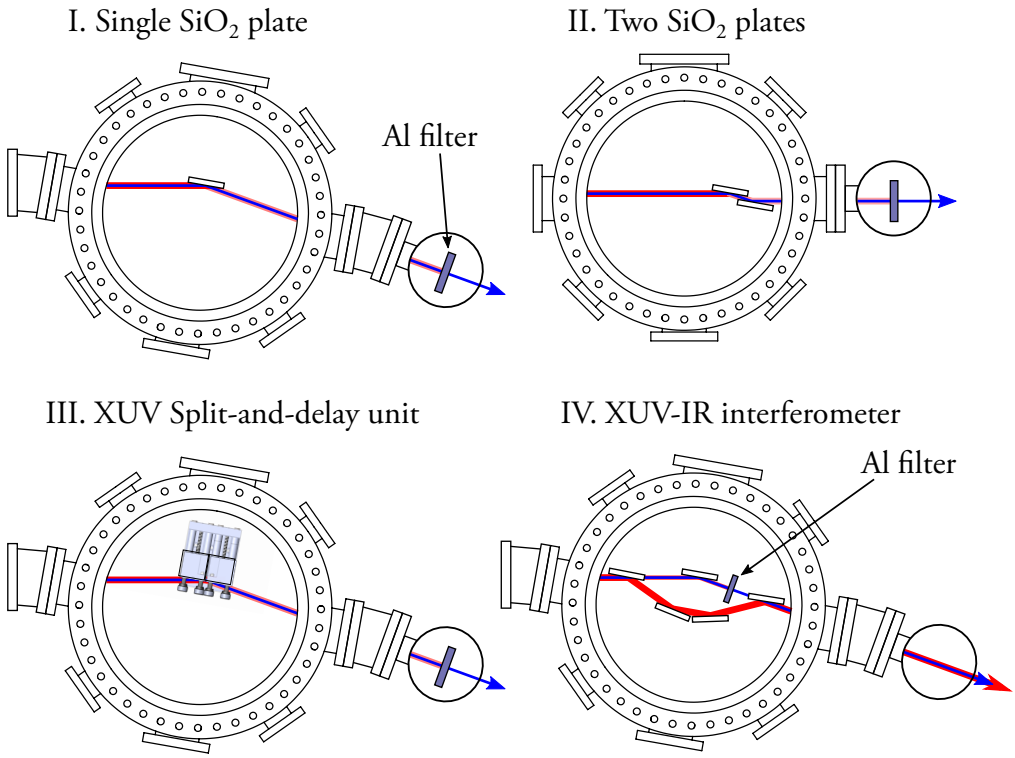

Figure 3.5: The different layouts of the interferometer chamber, showing sketches of optical components as well as XUV (blue) and IR (shades of red depending on power) beams.

II. Two silica plates

The original design for the chamber, used in the experiments described in Paper I, featured two silica plates, in order to more fully extinguish the IR light. Positioning the two plates parallel also meant enabled the light to the chamber at the same angle as it entered, with simply a small lateral displacement, making alignment slightly easier than with the current "wedge" design.

III. XUV split-and-delay unit

An XUV Split-and-Delay Unit (SDU) has been developed earlier in the group [44] and its performance was tested during the time this thesis work was carried out. As shown in Figure 3.5, its design features two anti-reflection coated silica plates, each of which reflects half of the XUV beam. One of the two plates can be displaced, introducing a delay between the two half beams. The design enables XUV pump-XUV probe experiments with a precision as low as $10 - 20$ as (measured by online analysis in an auxiliary interferometer) and a range of up to 50 fs, as can be seen in Figure 3.6.

To test the delay range and stability of the SDU, a delay scan was run studying Above-Threshold Ionization (ATI), a common strong-field experiment [45] in argon using the fundamental IR field.

The total ion yield was estimated by summing up the whole signal on the Velocity Map Imaging Spectrometer (VMIS). Since ATI is a highly nonlinear process (the I_p of argon is 15.8 eV, or approximately 10 times the photon energy of the IR), this works as a higher-order intensity autocorrelation.

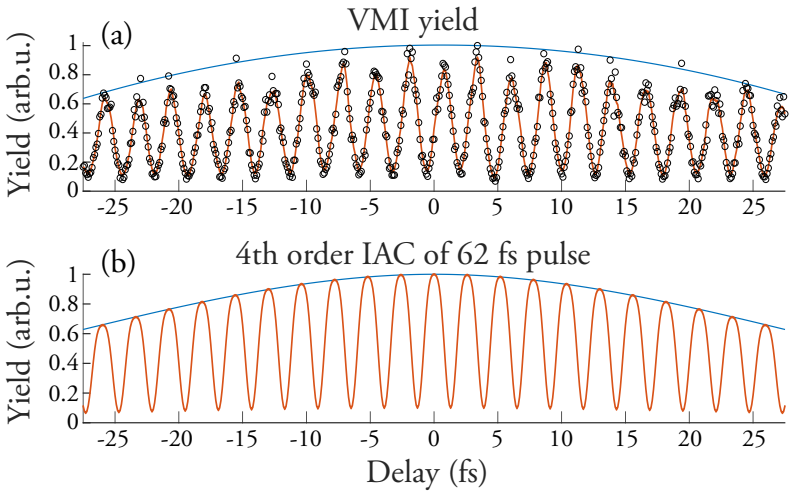

Figure 3.6: (a) ATI scan using the XUV split-and-delay unit and (b) a simulated 4th order interferometric autocorrelation of a 62 fs IR pulse. Adapted from [46].

Figure 3.6 (a) shows the ion yield as a function of the delay. As can be seen, there is a strong oscillation, which can be shown to have a period of around 2.7 fs, corresponding to one cycle of the IR field. Seen as the interferometric autocorrelation trace of the IR, this can also be used to estimate the pulse duration of the IR [46]. Assuming 4th-order interferometric autocorrelation[3], as shown in (b), this corresponds to a pulse with a duration of 62 fs, which is longer than the 50 fs which was measured (by second order autocorrelation before vacuum) just before this scan. Nevertheless this could possibly be explained by the fact that the light enters the vacuum through a glass window, which introduces some dispersion and might stretch the pulse.

IV. XUV-IR interferometer

The XUV-IR ("post-generation") interferometer, described in the following sections, was also mounted in the interferometer chamber. The filters used before were taken out of the beam path when using this setup, as the IR beam was desired for pump-probe experiments. Instead, a similar 200 nm Al filter was mounted directly in the XUV arm of the interferometer. The previously described SDU can also be installed in place of a single silica plate, as illustrated in more detail in Figure 3.7.

[3] A parallel can also be drawn here to the kind of strong-field ionization described as the first step of the three-step model in Section 2.2. An effective intensity dependence to the power of $\sim$4 was also found using TDSE calculations as part of Paper V.

3.3.2 XUV-IR interferometer design

Design constraints

The presented XUV-IR interferometer design is meant for pump-probe experiments, as described further in Section 6.1. Since these experiments are not in themselves a new pursuit, many laboratory setups have already been designed for this purpose. A common design is described in [47]. An IR pulse is split up, and one part is used for the HHG process, whereas the other, the probe pulse, is sent to a delay stage. After the first IR pulse has generated harmonics, it is attenuated by a metallic filter to make sure that this arm of the interferometer contains only the XUV light. The harmonics are then recombined with the probe pulse by way of a holey mirror, at which point the two beams are focused into a target.

There are some advantages to this design. The "leftover" IR from the generation process can be interfered with a small portion of the probe pulse to get an accurate reading of the delay. The differing optical pathways also enable a great deal of manipulation of the probe pulse; if, for example, a blue-light probe pulse of 400 nm is desirable and HHG is performed using an 800 nm IR laser, there is room for the probe pulse to be sent through a second harmonic generation crystal.

However, for the high intensity XUV beamline, this scheme is not considered to be viable. The main reason for this is the scale: as detailed in the previous section, the beamline is almost 15 meters long. Stabilizing delay and pointing fluctuations over this distance is a daunting prospect. This also applies to the interferometer design for the LONG GHHG beamline at ELI-ALPS, with the generation beam in some cases propagating for almost 100 meters, as detailed in Paper II.

The solution, then, was to place the interferometer after generation, i.e. to extract IR light for the probe pulse from the generation pulse itself, after the HHG process. Practically, this can be done using holey mirrors [22], as the shorter wavelength of the XUV light generally leads to a smaller divergence. Thus one may let the XUV light pass through a small hole in a mirror and use the IR light reflected around the hole as the probe pulse. Since this design mainly creates the delay in the IR arm (for reasons outlined in Section 5.1 it is not practical to have a delay stage for the XUV), these designs are typically better suited for XUV pump - IR probe experiments, as there is typically not a long delay range for the XUV after the IR.

Interferometer design

The XUV-IR, or post-generation, interferometer is designed for XUV-IR pump-probe experiments. The current design (a Mach-Zehnder design [48, 49]) is based on an earlier design by the author [50], itself based on an early idea proposed in the ELI-ALPS long beamline conceptual design report [15]. Because of the low reflectivity of most materials for XUV light at the 45° incidence often used in interferometers[4], the interferometer employs grazing incidence reflections to preserve XUV flux.

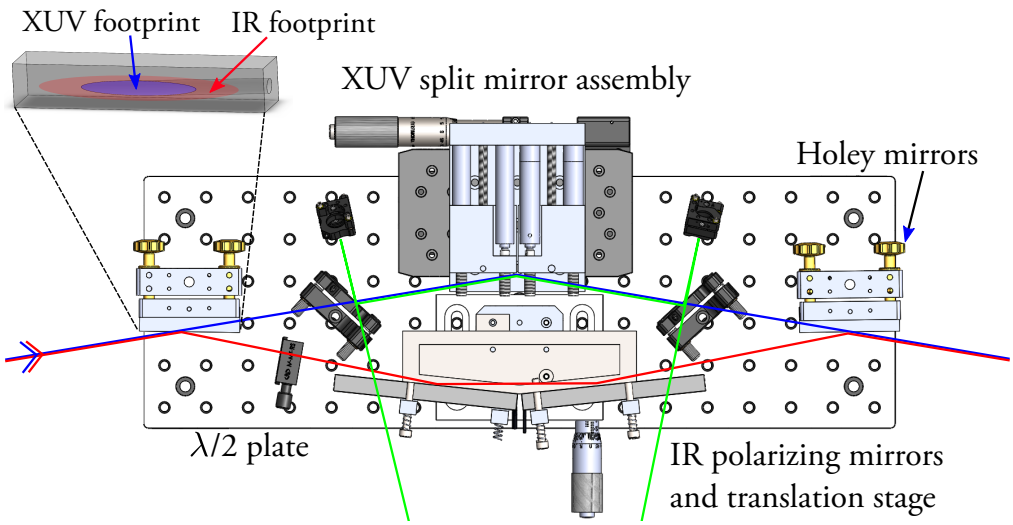

Figure 3.7: The design for the post-generation interferometer, including the SDU. The relevant beams are marked in red (IR), blue (XUV), and green (SDU stabilization laser). The inset in the top left corner shows the footprint of the XUV and IR on the holey mirrors.

The current configuration of the post-generation interferometer also includes the previously described SDU, which enables experiments with a multitude of pulses, such as XUV-XUV pump-probe experiments on targets that have been dressed or excited using an IR pre-pump. Figure 3.7 shows the design of the post-generation interferometer, with the SDU as the mirror in the XUV arm. As is evident, this further complicates the beam path; in addition to the IR (marked in red) and the XUV (blue), there is also the diode laser of the SDU (green), maintaining pointing and delay stability with the help of an additional interferometer setup outside the chamber [44].

The beam path of the XUV and IR can be followed from left to right in the sketch. The two beams are separated by a holey mirror, which admits all of the XUV light but reflects some of the IR due to the difference in divergence between the two beams (roughly shown in the inset of the figure). The XUV beam then travels through another holey mirror, used to couple in the stabilization laser. It is reflected on the split mirror (and possibly split/delayed, depending on the intended experiment), and is recombined with the IR after another set of holey mirrors. It is only reflected once, in order to maintain the XUV throughput of the interferometer. The XUV mirror is anti-reflection coated for the IR, meaning that less than 1% of the IR light in this arm is reflected. To remove the remaining

[4] See Section 5.1.

component, a thin Al filter (not shown, but installed between the two later holey mirrors) is used before recombination.

The IR beam is reflected on a pair of multilayer-coated glass plates which function as highly discriminating polarizers. In combination with the half-wave plate (seen to the left of the polarizing mirrors), it provides a high degree of accuracy in controlling transmitted IR intensity.

As previously mentioned, and seen in the design, the interferometer operates on grazing incidence beams. The XUV light is reflected once at 10° angle of incidence, while the IR is deflected to be at a 12° angle from the axis of the chamber and reflected twice. The two reflections mean that the beam footprint on the second holey mirror does not move when the delay stage is moved. This, however, means that the angle needs to be higher than that in the XUV arm, to enable the IR pulse to reach the target before the XUV.

Due to the shallow angles in the interferometer, the IR polarizing mirrors are quite wide; the maximum footprint of 15 mm for the IR beam leads to a minimum mirror width of around 72 mm. Taking into account the fact that the beam moves on the mirrors, they need to be expanded further, leading to the current width of 110 mm.

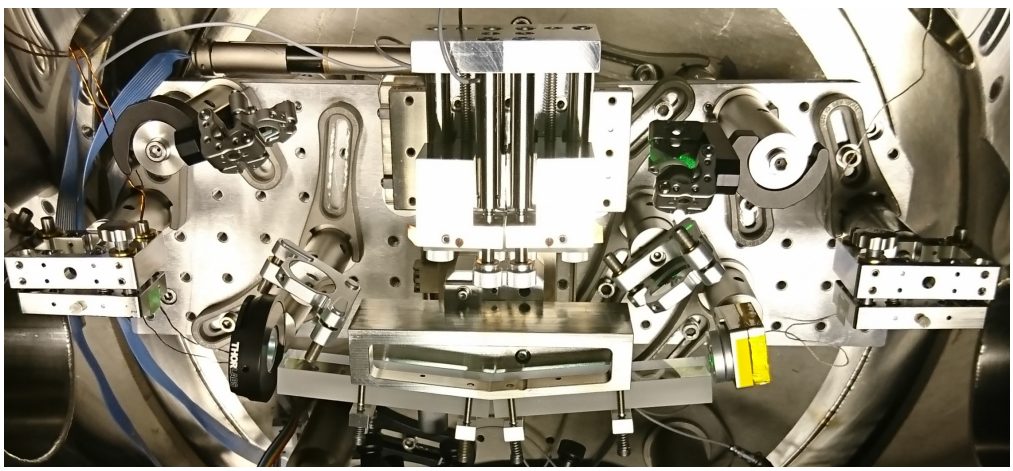

Figure 3.8: A photograph of the post-generation interferometer, including the XUV split mirror, as sketched out in Figure 3.7.

Figure 3.8 shows a photograph of the post-generation interferometer installed in the interferometer chamber described in Section 3.3.1. As seen here, after the polarizing beamsplitters the IR light passes through a motorized iris aperture. If needed, this provides further attenuation by clipping the annular beam from the outside.

The piezoelectric delay stage allows for closed loop operation, with the help of a strain gauge mounted inside the stage itself [51], meaning a high degree of repeatability without the need for an external delay stabilization loop. Its stated characteristics are a 400-µm scan range, and a resolution of 8 nm [51]. Considering the IR optical path a trapezoid, it can be calculated[5] that changing

[5]Note that this result is half the factor calculated in [50].

the height of the trapezoid corresponds to a change in the IR path length with a factor of 0.416, i.e. moving the mirrors down by 1 µm will increase the path length by 0.416 µm.

Taking into account the propagation time of the light as $t = d/c$, this factor will yield the delay range and resolution, according to:

$$\Delta t\,(\text{Delay range}) = \frac{0.42 \cdot 400\ \mu\text{m}}{c} = 5.604 \cdot 10^{-13}\ \text{s} \approx 560\ \text{fs}$$
$$\text{and} \tag{3.1}$$
$$\Delta t\,(\text{Resolution}) = \frac{0.42 \cdot 8\ \text{nm}}{c} = 1.122 \cdot 10^{-17}\ \text{s} \approx 11\ \text{as}.$$

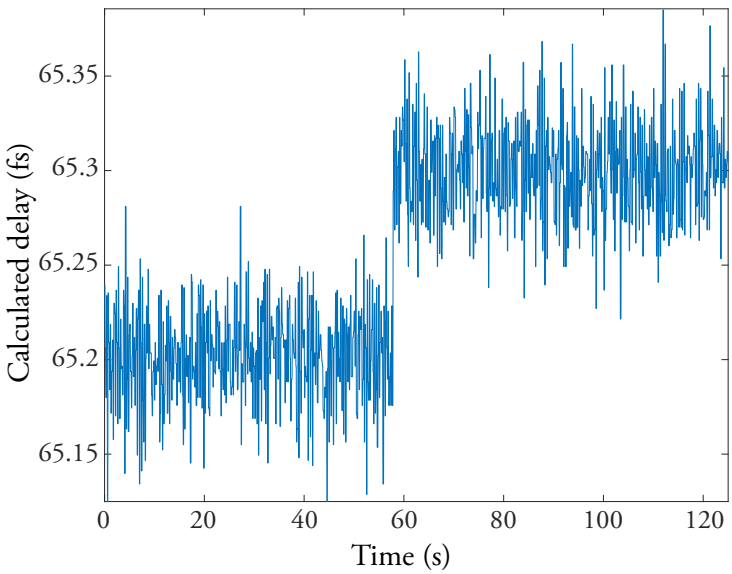

Figure 3.9: The delay calculated from the log of the distance measurements of the piezoelectric translation stage's strain gauge.

To estimate the stability of the delay, it was measured by assuming the XUV mirror remains stationary, and using the distance measured by the strain gauge of the piezoelectric translation stage. The result of logging this can be seen in Figure 3.9, for two steps in a delay scan (chosen arbitrarily, but deemed to be typical).

As can be seen, around 60 seconds into the scan, the set delay is changed from 65.2 to 65.3 fs. The stability of the delay can be judged with this distance as a reference. Apart from the fact that there is hardly any visible backlash (sudden backwards movement as a result of overcompensation during motion), it can also be seen that the absolute error for both delay steps is below 50 as, with a few exceptions. The Root Mean Square (RMS) delay error for this scan was generally between 25 and 30 as. This is higher than that calculated from the specifications but could be due to many factors, such as the coefficients in the PID loop of the stage not being perfectly calibrated.

Commissioning – IR ATI

In order to find the zero-delay (temporal overlap) of the interferometer, and test its performance, the aluminium filter was removed from the XUV arm and the IR passing through the two arms was sent into the focusing optics of the application chamber, as depicted in Section 3.5.

The two IR beams were sent in at varying relative delays to perform ATI, in a similar manner to the SDU testing shown in Figure 3.6, but with neon as the target.

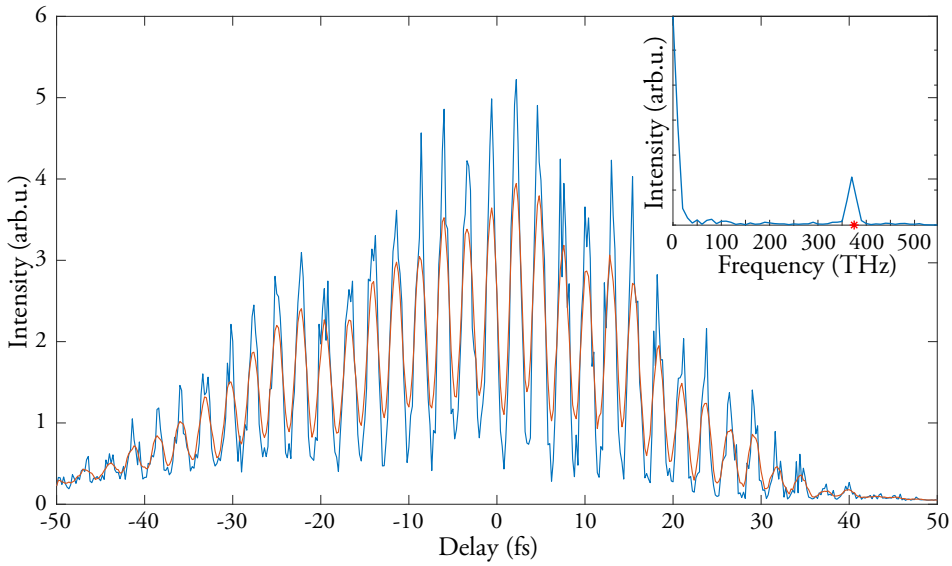

Figure 3.10: The results of a long ATI scan in neon. The *y* axis shows the integrated ion yield, in blue for the measurements and in red with a 7 point running average. The inset shows the Fast Fourier Transform (FFT) of this scan (only the low frequency components), with the red asterisk marking the fundamental frequency of the IR field.

Figure 3.10 shows the results of a 100-fs long scan, in steps of 0.4 fs. Note that in this and subsequent scans, "0 fs" does not necessarily correspond to the exact point of 0 fs delay between the two arms, but was determined in the first round of ATI measurements to be at, or close to, the temporal overlap. The integrated ion yield (the sum of the counts measured by the VMIS[6]) is shown in blue. To minimize the effects of energy fluctuations and render the oscillations a little clearer, a 7-point running average ("smoothing") was also used as, effectively, a low-pass filter, shown in red.

The performed delay scan fills two purposes: it verifies the calculated delay scale, and was used to measure the duration of the IR pulse itself.

To verify the accuracy of the delay scan, rather than measure the peak-to-peak period of the oscillations (which gives a reasonable estimate but is limited by the 0.4 fs resolution), an FFT analysis was

[6] See Section 3.5 for a brief discussion on the VMIS.

performed, as shown in the inset of Figure 3.10. The red asterisk indicates the frequency of the 800 nm fundamental laser field (375 THz), which coincides well with the main (non-DC) peak found in the spectrum of the scan. This was taken as an indication that the time scales are well calibrated.

Once the scale is verified, the ATI signal can be used to measure the pulse duration of the IR pulse. For this, an envelope was fitted over the curve in Figure 3.10. With some assumptions as to the nonlinear order of the process, interaction region, and temporal pulse shape [46], a pulse duration of approximately 60 fs could be extracted.

The pulse duration extracted from this scan is significantly higher than the 40 fs measured after the compressor, but could perhaps be explained by the fact that this first scan was performed with the interferometer chamber at atmospheric pressure. Consequently, the beam path included two additional window valves (of unknown thickness and glass quality) to transport it out of vacuum and back in again. Dispersion by propagation of the IR beam through 20 mm of ordinary fused silica, for example, could almost double the pulse duration [52].

3.3.3 Directions for improvement

While the first results of testing the XUV-IR interferometer are promising, as indicated by the section on challenges there are still some things that could be improved when striving towards more advanced or precise measurements.

Stability

Because of the grazing incidence angle on the optics, even a small angular shift will lead to a finite displacement on the mirrors, which in this case seems to slightly shift the delay between the IR and XUV arms on a day-to-day basis, as well as the XUV-IR focal overlap. This also applies to the pointing fluctuations experienced throughout the measurements.

One problematic aspect of the current XUV-IR interferometer design is the fact that the two arms do not have the same parity, i.e. the XUV beam is reflected once and the IR beam twice. Thus, when the incoming, co-propagating beams are reflected in their respective arms, a sideways displacement of the beam leads to the XUV beam moving in one direction and the IR beam moving in the other. Expressed in a different way, the effect of already existing pointing instabilities is amplified and may lead to a poor signal (focal spot mismatch) and delay errors.

This situation has practical origins. Another reflection in the XUV would reduce the available pulse energy further, as discussed in Section 5.1. Since one of the main goals of the beamline is to have a high XUV intensity, this was not deemed a suitable option, but as will be discussed later, if more XUV energy was to become available, ensuring parity will likely lead to a more stable design.

Long-range pump-probe experiments

As previously mentioned, the XUV-IR interferometer has a delay range of around 560 fs. The limits to this are set by the limits of the delay stage; in order to attain the resolution needed for phase-sensitive measurements such as RABBIT[7], one must use very accurate translation stages, for instance piezoelectric stages. Unfortunately, these kinds of stages are often not practical for longer distances (i.e. more than hundreds of micrometers to a millimeter or so).

There are, however, many pump-probe experiments where it would be beneficial to use a longer pump delay. Especially in the case of large molecules, there are many "slow" processes that may occur on the picosecond timescale [53].

Another example of an experiment where a longer delay would be beneficial is that of molecular alignment. In this case, nonadiabatic, or field-free alignment is discussed, as adiabatic alignment by necessity involves much longer laser pulses than other experiments described in this thesis [54].

A simplified, classical view of nonadiabatic (or impulsive) alignment is that an intense laser pulse impinges on the molecules. The deviation of the molecular axes from the polarization vector of the laser pulse gives the molecules a "kick" (impulse of angular momentum), the magnitude of which depends on the magnitude of the deviation. This means that the molecules will start to rotate with varying speeds depending on their orientation. After a certain time, contingent on the size of the molecules, they will have aligned themselves to the polarization of the laser. The timescales involved here are typically on the order of $10 - 100$ ps.

Techniques already available at the intense XUV beamline, such as velocity map imaging, allow for angularly resolved studies in the ionization and fragmentation of molecules. When performing these kinds of measurements it could be helpful to align the molecules so that there is a definite axis from which to define the angles of the measurement [55].

3.3.4 Pre-generation interferometer

The aim of this interferometer is to address the need for longer delay ranges than those offered by the post-generation interferometer described previously. The longer delay range is solved by using a longer-range stage, a stepper motor stage enabling up to 300 ps range, as a sub-femtosecond resolution for these longer delays is less important. The specified resolution, given by the repeatability of the stage, is still quite good at 7 fs, considering the total range [56]. These delays were calculated as before, but given the much simpler layout of the delay stage (45° reflections everywhere) the total distance was simply taken as double the movement of the stage.

This interferometer, also a Mach-Zehnder-type design, splits an incoming IR pulse with the help of specially coated polarizing beamsplitters at a 56-degree angle of incidence. A $\lambda/2$ plate before the first beamsplitter regulates the division of energy into the pump beam and the generation beam. The setup can be seen in Figure 3.11.

The generation beam is what is left as the s (vertical) polarization after the wave plate. This polariza-

[7] See Section 6.2.1 for an overview of this technique.

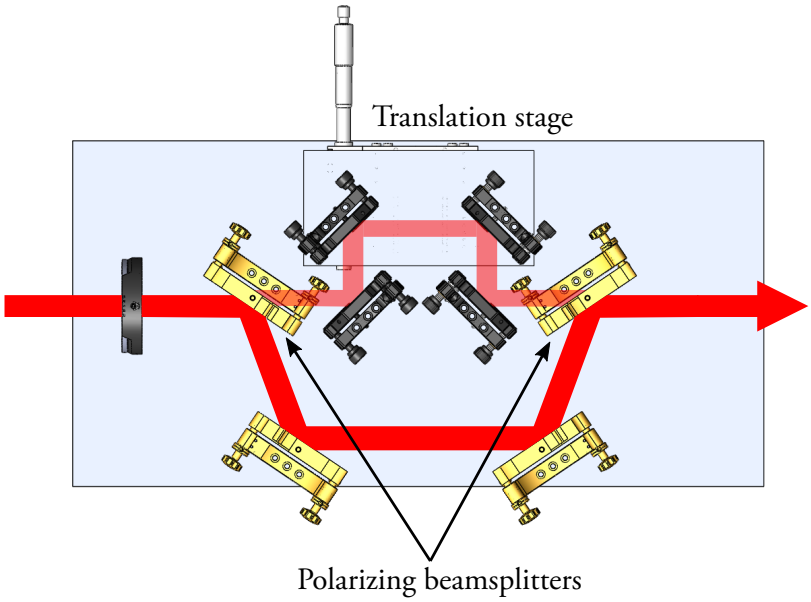

Figure 3.11: The design for the pre-generation interferometer, showing the polarizing beamsplitters dividing the IR into the weak, horizontally polarized pump beam (translucent red) and the strong, vertically polarized generation beam (solid red).

tion is reflected on all the beamsplitters, and is thus affected very little by its transport through the interferometer. The beamsplitters have a reflectivity for the s polarization of around 99.5%, which means that when experiments not requiring long-range IR delays are being performed, all the IR can be sent through this arm, leading to a total insertion loss of only a few percent. Thus the setup may be installed continuously at the beamline, minimizing the downtime between experiments.

The pump beam gets a p (horizontal) polarization and is transmitted through the beamsplitters. The substrate used for the beamsplitters was selected to be low-dispersive glass which is not expected to affect the pulse duration to a substantive degree[8].

In combination with the $\lambda/2$ plate and polarizing mirrors in the post-generation interferometer, this IR-IR interferometer enables a strong discrimination between the two beams. For example, one may use 5% of the pulse energy as a pump beam, which is low enough not to ionize the medium and disturb the HHG process. In the post-generation interferometer, the pump beam is turned to s polarization by the $\lambda/2$ plates and only attenuated by a small factor. The IR pulse used for generation, in the meantime, is turned to p polarization and almost completely attenuated [50].

Together, these two interferometers (the long-range pre-generation interferometer and it high-resolution post-generation counterpart) enable a wide range of experiments, including, for example, IR pump-XUV probe studies on slow molecular dynamics, and XUV pump-IR probe experiments on aligned molecules.

[8]The dispersion is specified as less than 100 fs^2 through the substrate, meaning a stretching of less than 1 fs for a 40 fs pulse; compare, for example, to Figure 4.9 (d).

3.4 Beam diagnostics

Studying the properties of the harmonics generated at the beamline is not only important in order to interpret experiments in which they are used, but can also be an interesting pursuit in itself, as discussed in the present thesis. To these ends, the beamline has a diagnostics chamber placed after the interferometer chamber. The chamber contains a gold mirror on a rotation stage so that the beam can be sent out through any of the outgoing ports. The gold mirror is slightly off-axis in order to swing completely out of the way, allowing the beam to enter the application chamber unimpeded.

During the course of this thesis work, XUV Wavefront sensors (WFSs) have been used both as diagnostic tools and for more in-depth studies of the harmonic wavefronts, as described in Chapters 4 and 5 and Papers III and VI. These have not only been mounted on the diagnostic chamber but are presented here for convenience.

3.4.1 XUV spectrometer

The XUV spectrometer in the beamline is a Jobin-Yvon imaging spectrometer combining a toroidal mirror and a flat-field, variable line space grating [57], using a Multi-Channel Plate (MCP) for XUV photon detection [58].

Typically, the horizontal axis is integrated in order to improve the statistics on the spectrum, but this axis can also be used to estimate the horizontal position and/or width of the XUV beam, which was used for the study presented in Paper V to spectrally resolve the harmonic divergence. The image on the MCP can be seen in the inset of Figure 3.12.

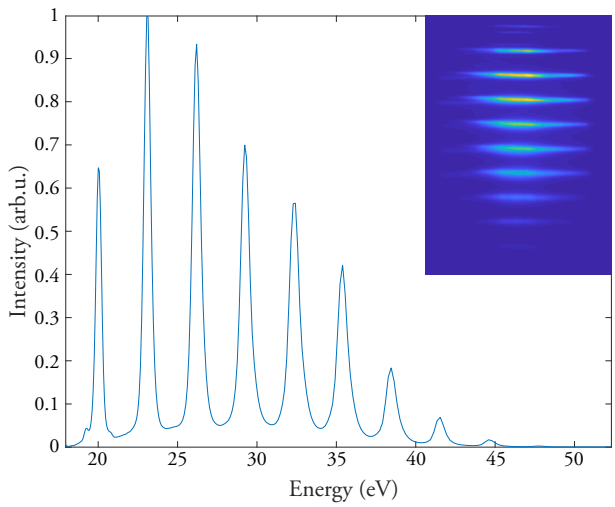

Figure 3.12: XUV spectrum generated in argon. The inset shows the raw image on the MCP screen (cropped).

A typical spectrum, corrected for the grating constant and the transmission/reflection curves of the aluminium filter and gold mirror [59], is also depicted in Figure 3.12. This spectrum was generated in argon which was the gas predominantly used for the experiments making up this thesis work, but harmonics were also generated in neon (higher photon energies) as well as krypton and xenon (lower photon energies, but higher flux)[9].

3.4.2 Imagine Optic / LOA wavefront sensor

An XUV wavefront sensor consisting of a Hartmann mask and an XUV Charge-Coupled Device (CCD) camera, co-developed by the Laboratoire d'Optique Appliquée (LOA) and Imagine Optic, was used for two campaigns, presented in the two following Chapters and described thoroughly in Papers III and VI.

3.4.3 Locally constructed wavefront sensor

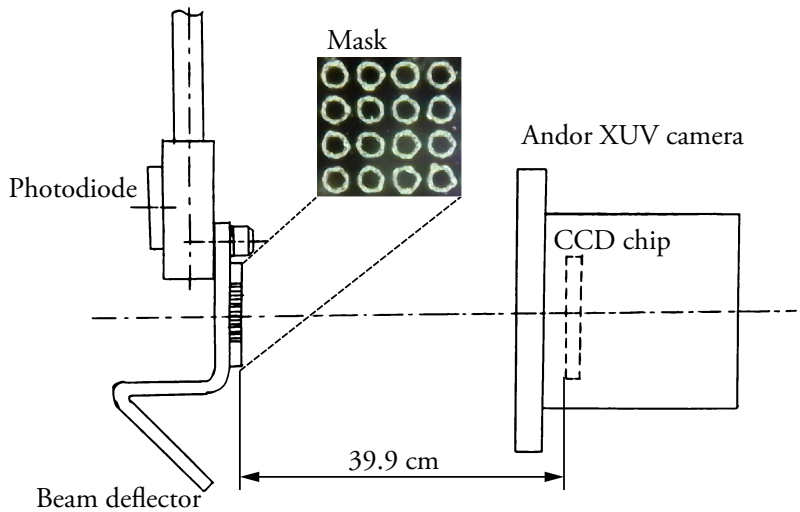

Figure 3.13: A sketch of the design for the Lund WFS. The inset for the mask shows one of the Hartmann masks used, imaged using a microscope. Figure adapted from [60].

Inspired by the experiments performed with the previously mentioned WFS, a custom wavefront sensor was constructed as part of the Master's thesis of Fabian Brunner [60]. It follows the same principle as the previously mentioned wavefront sensor, with a Hartmann mask mounted in front of a camera, which in this case was the Andor camera described in Section 3.5.4. The design of the WFS can be seen in Figure 3.13, along with a picture of one of the Hartmann masks used, made out of glass. This wavefront sensor was used for some of the experiments described in the next two Chapters.

[9] See Section 2.2.2 for a discussion on the impact of the element-specific ionization potential.

3.5 Application chamber

The beamline features an application chamber, oriented towards ionization of atoms and molecules and study of ionization and fragmentation products. Figure 3.14 shows a drawing of the application chamber.

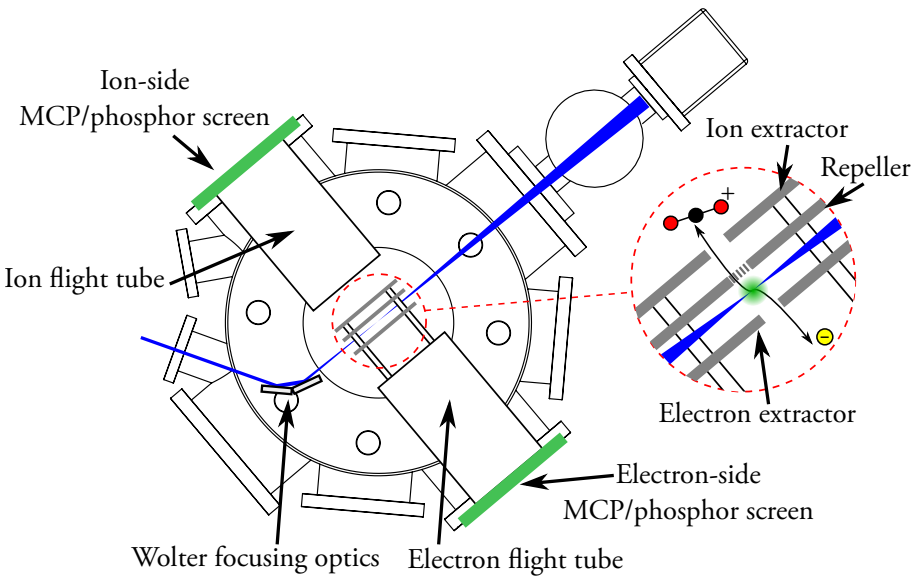

Figure 3.14: A sketch of the intense XUV beamline application chamber.

3.5.1 XUV focusing

The harmonics from the beamline are focused by two toroidal mirrors in a Wolter-like configuration [44, 61]. The reason for this configuration, as discussed in Section 5.2, is that the comatic aberrations of each of the two mirrors can compensate for the other's.

These toroidal mirrors and their impact on the wavefront of the XUV beam have been thoroughly studied, as described in Paper III and Section 5.3.

3.5.2 Molecular source

The beamline features a molecular source with an Even-Lavie valve [62]. This valve, apart from delivering a supersonic jet enabling high gas density, also features a small furnace that can be used to evaporate liquid and solid phase samples into the application chamber, rendering possible investigations of a wide range of targets.

After the valve, the molecular source chamber contains two skimmers, which reduce any superfluous

gas apart from the dense center of the jet from entering the application chamber, maintaining the vacuum level in the chamber (optimally in the region of 10^{-9} mbar).

This molecular source was used for all ionization experiments at the intense XUV beamline described in this thesis including those in Papers I and IV. In the drawing seen in Figure 3.14, the molecular beam can be seen to be coming from "above" through the focus.

3.5.3 Double-sided Velocity Map Imaging Spectrometer

The double-sided Velocity Map Imaging Spectrometer (DVMIS) was designed to allow simultaneous, angularly resolved measurements of the momenta of ions and electrons, as described in Paper IV. The placement of this instrument in the application chamber can be seen in Figure 3.14; the inset to the right shows a closer look at the electrodes.

The operating principle of the VMIS is expanded upon in Paper IV as well as in [63]. In short, by accelerating ions and/or electrons using an electric field, a 2D projection of the 3D momenta of the particles is made on the detector surface (in this case an MCP with a phosphor screen). Assuming a cylindrical symmetry around the laser polarization axis, the 3D projection can then be folded out to retrieve the true 3D momentum distribution, in a process known as Abel inversion, for which there are several algorithms available [64–66]. Figure 3.15 shows the effect of inversion on an image of a photoelectron momentum distribution.

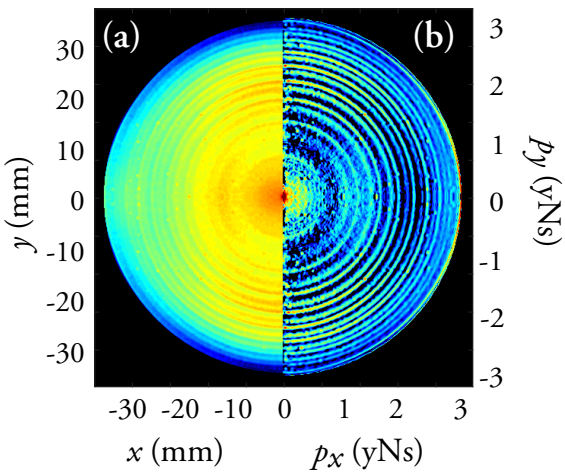

Figure 3.15: A photoelectron momentum distribution, (a) before and (b) after inversion. Figure adapted from Paper IV.

The double-sided design takes advantage of the fact that positively and negatively charged particles are accelerated in opposite directions by the electric fields used in a regular VMIS [63], and thus consists of two sets of flight tubes and extractors, catching the electrons in one direction and positive ions in the other. When it is used as double-sided, the ions are sent through the repeller, which has been fitted with a fine mesh instead of a solid metal electrode.

When studying the ionization of atoms and molecules, this instrument may also be used to measure the Time-Of-Flight (TOF), in order to produce a mass spectrum of ions and possible fragments.

It is of great interest to correlate measured electrons with the ions and fragments from which they emerge, especially in the case of advanced molecular targets that feature several kinds of fragmentation and ionization dynamics. In systems with a high repetition rate, this is typically done in a coincidence scheme, where the incident rate is kept so low ($\ll 1$ event per shot) that any electrons and ions measured simultaneously can reasonably be expected to emerge from the same reaction. This type of technique is used in instruments such as the Reaction Microscope (REMI) [67].

On the intense XUV beamline and other light sources with a similarly low repetition rate, the coincidence scheme is impractical. For this reason, a covariance scheme is used, in which every shot is saved separately, making it possible to determine which "variables" (in this case, each variable is, for example, a single kinetic energy in the velocity map image or mass in a TOF mass spectrum) that correlate with each other and in what way [68]. The viability of this covariance scheme was demonstrated at the intense XUV beamline, as described further in Paper IV.

3.5.4 Camera and wavefront sensor

After the target jet, the beam propagates through the chamber and leaves through one of the flanges on the other side. Here, a small chamber with a manipulator, similar to the filter holder of the interferometer chamber, is mounted. If the holder is left empty, the beam travels to an Andor iKon XUV CCD camera. In addition to providing a high spatial resolution (2048 by 2048 pixels with 13.5 µm pixel size), this camera is also energy-calibrated, so that it can be used to measure the energy of the beam directly.

The chamber also contains an XUV photodiode that can measure the beam energy at a higher repetition rate than the CCD camera. This enables online, single-shot pulse energy measurements which are necessary for partial covariance calculations, in which false covariance effects caused by energy fluctuations are removed, as discussed in Paper IV.

Finally, the chamber contains the masks for the Lund wavefront sensor described in more detail in Section 3.4.3.

3.6 CDI Chamber

One interesting target is not in or after the application chamber. Before the interferometer chamber, it is possible, by means of mirrors on a rotation stage, to divert the beam into another target chamber. This chamber was employed for experiments on using the harmonics of the beamline for Coherent Diffraction Imaging (CDI), as well as frequency-resolved wavefront sensing, both of which are discussed briefly in the outlook.

Moreover, as it provided a good space for various measurement equipment in vacuum and without the optics later in the beamline, this chamber was also used for other experiments, including the single-wavelength wavefront measurements described in Paper VI.

3.7 The LONG GHHG beamline at ELI-ALPS

3.7.1 Beamline overview

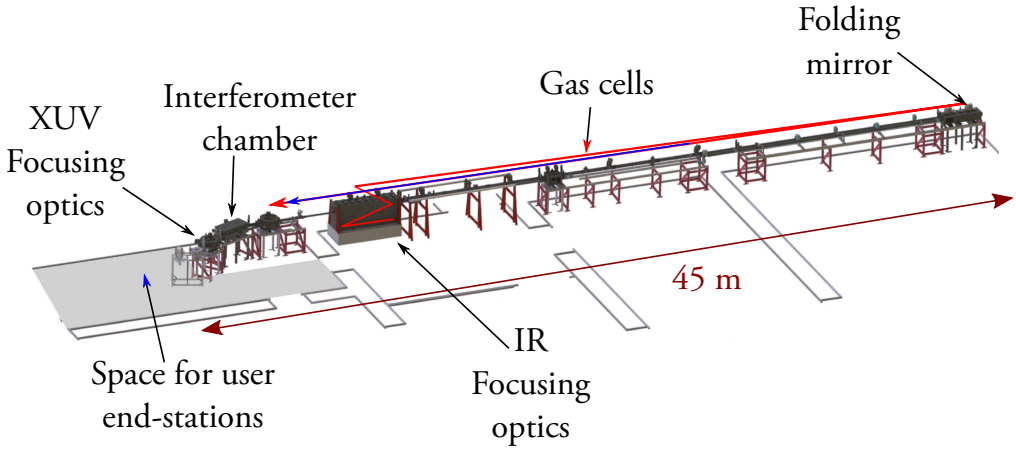

Figure 3.16: The layout of the LONG GHHG beamline, adapted from Paper II. The relevant beams are marked in red (IR) and blue (XUV).

The LONG GHHG (Long Gas HHG) beamline is a beamline under construction at the ELI-ALPS facility in Szeged, Hungary, described in more detail in Paper II. It is one of the systems based on the state-of-the-art SYLOS laser, which uses Optical Parametric Chirped-Pulse Amplification (OPCPA) technology to deliver few-cycle, high energy pulses (nearly 5 TW peak power) at a repetition rate of 1 kHz.

To take advantage of the high-power pulses provided by the SYLOS laser, the LONG GHHG beamline is constructed after the scaling principles outlined in Section 2.3.2. This leads to some quite extreme results: the IR beam will in some cases be focused with a focal length of 55 meters, generating in a 6-m long gas cell (consisting of 15 sub-cells) with only 1 mbar generation gas pressure.

After generation, the beam enters a "transport" chamber, which can be used to divert the beam or introduce a long pump-probe delay. It is then sent to an interferometer chamber, which is in many respects similar to that described in Section 3.3.1. This chamber contains the XUV-IR interferometer described in the next section, as well as an XUV SDU similar to the one installed at the LLC intense XUV beamline. Both of these instruments can be seen in more detail in Figure 3.17.

After the interferometer chamber and a diagnostics chamber, allowing for instruments such as VUV and XUV spectrometers, the beams can be sent to the target. A compact setup featuring XUV focusing optics and a TOF spectrometer is planned but can be replaced with instruments that users bring to the beamline.

It is expected that this beamline will deliver up to 0.5 µJ XUV pulse energy per shot, which at a repetition rate of 1 kHz corresponds to an average power of 0.5 mW, among the highest of any HHG based light sources [14].

3.7.2 XUV-IR interferometer

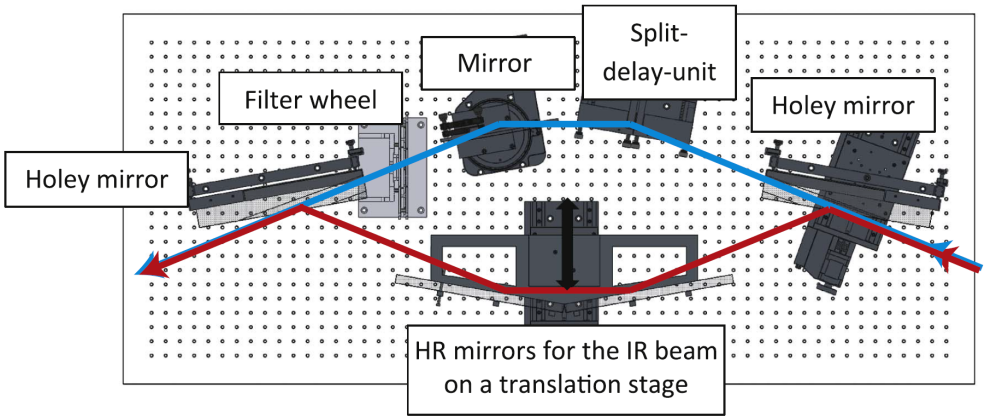

Figure 3.17: The design for the post-generation interferometer, taken from Paper II. The relevant beams are marked in red (IR) and blue (XUV).

Figure 3.17 shows the design of the XUV-IR interferometer intended for the LONG GHHG beamline. The design is based on, and similar to, the previously described post-generation interferometer created for the intense XUV beamline, with a few modifications in order to take into account the scale of the "long" beamline and improve the stability.

In this design, both arms have two mirrors. Consequently, both arms are at the same parity, meaning pointing fluctuations in the beam are more or less identical in the two arms. If the parity is odd, such as in the previous design, pointing fluctuations will cause the beam to move in different directions for the two arms. As mentioned in Section 3.3.2, with the large propagation distances of the long beamline, this becomes even more critical.

Naturally, this means that this design has a lower XUV transmittance. However, as mentioned before, this is a high-power system, both in terms of average and peak power. The SYLOS laser is expected to provide almost two orders of magnitude higher average power, and twice the peak power, of the driving laser for the intense XUV beamline[10], meaning that some concessions can probably be made in this respect, assuming that the HHG can be scaled up successfully [14].

[10] Assuming 100 mJ, 40 fs at 10 Hz for the LLC TW laser (Section 3.1) and 45 mJ, 10 fs at 1 kHz for the SYLOS (Paper II).

Chapter 4

Spatial properties of high-order harmonics

It could be argued that the spatial properties of light waves have been studied for as long as there has been a wave theory of light [69, 70], and they form an integral part of this thesis. It is thus important to have good models of these properties.

This chapter will introduce some fundamental Gaussian optics to describe the propagation of light beams, as well as a theory on wavefront aberrations, based on Zernike polynomials. Following this is an introduction to metrology and correction of wavefront aberrations. The chapter ends with details on three experimental studies of the spatial properties of light: the dipole-phase induced wavefront curvature, the generation-dependent wavefront aberrations, and the impact on the XUV wavefront of passing through an MCP filter.

4.1 Gaussian optics

One particularly useful description of the spatial properties of light, especially for the discussion of laser beams, is that of the Gaussian beam, which combines aspects of spherical waves and plane waves; the function reduces to a plane wave in the focus ($z = 0$) and to a spherical wave in the far field ($z \to \infty$) [35].

A Gaussian beam is a beam whose complex spatial amplitude can be described as

$$E(x, y, z) = A_0 \frac{w_0}{w(z)} \exp\left[-\frac{r^2}{w^2(z)}\right] \exp\left[-ikz - ik\frac{r^2}{2R(z)} + i\xi(z)\right], \tag{4.1}$$

where the first three factors define the amplitude of the beam, and the last factor defines the phase. The beam propagates along the z direction and its transverse amplitude and phase are assumed to be cylindrically symmetric according to the coordinate $r = \sqrt{x^2 + y^2}$. The wavenumber k is defined as $k = 2\pi/\lambda$, where λ is the wavelength of the light.

Some important derived parameters of Equation (4.1) are the beam waist

$$w_0 = w(0) = \sqrt{\frac{\lambda z_0}{\pi}}, \tag{4.2}$$

the beam width

$$w(z) = w_0 \sqrt{1 + \left(\frac{z}{z_0}\right)^2}, \tag{4.3}$$

the wavefront radius of curvature

$$R(z) = z\left[1 + \left(\frac{z_0}{z}\right)^2\right], \tag{4.4}$$

the Gouy phase

$$\xi(z) = \tan^{-1}\frac{z}{z_0}, \tag{4.5}$$

and the Rayleigh length

$$z_0 = \frac{\pi w_0^2}{\lambda}. \tag{4.6}$$

These parameter definitions may also be used further. For example, for a given width $w(z)$ and radius of curvature $R(z)$, one may find that the waist (focus position) can be found at

$$z(w_0) = \frac{R(z)}{1 + \left(\frac{\lambda R(z)}{\pi w(z)^2}\right)^2} \tag{4.7}$$

and the waist radius is

$$w_0 = \frac{w(z)}{\sqrt{1 + \left(\frac{\pi w(z)^2}{\lambda R(z)}\right)^2}}. \tag{4.8}$$

Finally, in the far field (far out of focus, i.e. $z \gg z_0$) the beam width can, by neglecting the first term of equation (4.3), be estimated as

$$w(z) \approx \frac{w_0 z}{z_0} = \theta_0 z, \tag{4.9}$$

where θ_0 is the so-called divergence angle, which can be expressed as

$$\theta_0 = \frac{w_0}{z_0}. \tag{4.10}$$

Following the definition of the Rayleigh length in Equation (4.6), this leads to

$$\theta_0 = \frac{\lambda}{\pi w_0}, \tag{4.11}$$

showing an inverse relationship between divergence and focus size, as well as a linear relationship between divergence and wavelength.

4.2 Wavefront aberrations

When the wavefront of the beam does not conform to an ideal, e.g. a flat, spherical or Gaussian wavefront, it is said to be aberrated. These aberrations can be expressed and defined in different ways depending on the context. In any case, in order to develop an understanding of beam quality and the deviation from the norm, one must develop a "vocabulary", in order to discuss and compare different wavefronts.

A common way to describe the measured aberrations is to use Zernike polynomials [71, 72]. This is a way to characterize the aberrations as a sum of radially and angularly dependent periodic functions on the unit circle $r \leq 1$, here referred to as the pupil of the wavefront.

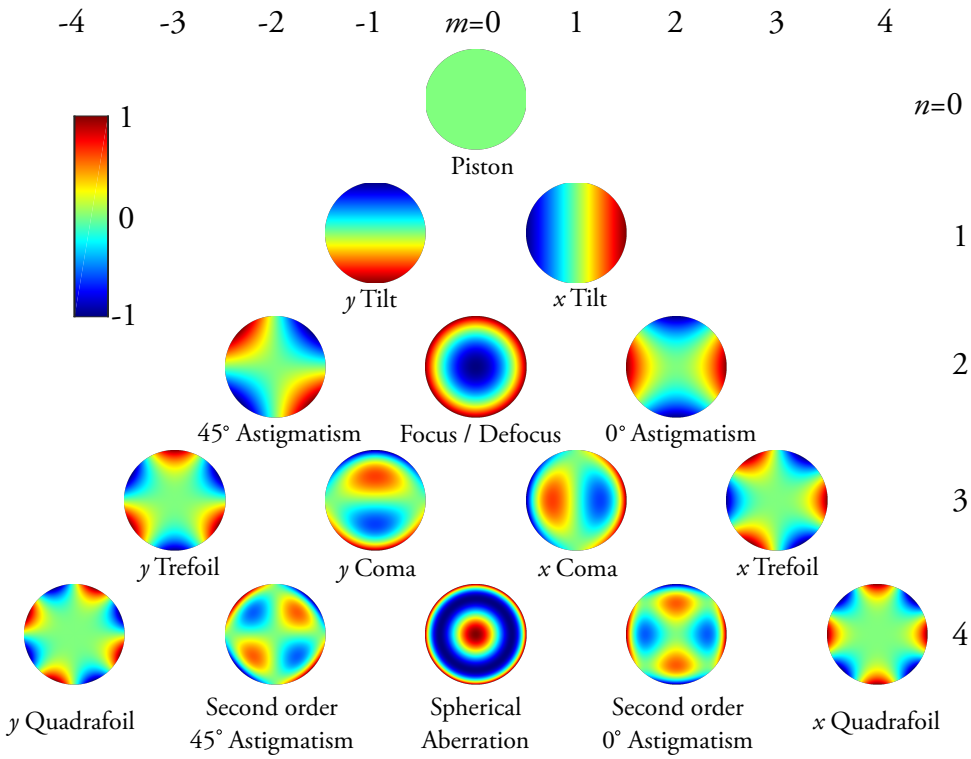

Figure 4.1: The first five orders of aberrations as their Zernike polynomials Z_n^m. The colorbar shows the value of the functions.

The wavefront $W(r, \theta)$ can then be represented as a sum of polynomials

$$W(r, \theta) = \sum_{n,m} C_n^m Z_n^m(r, \theta) \tag{4.12}$$

where C_n^m denotes the coefficient (i.e. the influence of the particular aberration m, n on the wave-

front) and Z_n^m corresponds to the Zernike polynomials themselves, defined as

$$Z_n^m(r,\theta) = \begin{cases} R_n^m \cos m\theta, & m \geq 0 \\ R_n^{|m|} \sin m\theta, & m < 0 \end{cases} \tag{4.13}$$

where R_n^m is the radial function, which can be written as

$$R_n^m(r) = \sum_{k=0}^{\frac{n-m}{2}} \frac{(-1)^k (n-k)!}{k! \left[\frac{1}{2}(n+m)-k\right]! \left[\frac{1}{2}(n-m)-k\right]!} r^{n-2k} \tag{4.14}$$

Figure 4.1 shows the first five orders and the common names of these aberrations, which will be used from time to time, in particular when referring to lower-order aberrations. Specifically, when dealing with focusing optics, depending on the geometry, astigmatism and coma become very important to characterize as they greatly affect the shape of the beam focus.

4.3 Wavefront metrology

In order to determine how the previously mentioned aberrations affect real-world beams used in our experiments, wavefront metrology is necessary.

One of the most common ways of measuring the wavefront is by letting the beam pass through an array of holes in a so-called Hartmann mask [73]. For each hole, the light passing through the hole (known as a beamlet) is deflected in the direction corresponding to the local slope of the wavefront. Figure 4.2 shows an illustration of this.

As shown in Figure 4.2, for each hole the spot of the diffracted beamlet can be compared with that of the reference wavefront, and their difference in position on the plane of the detector is defined as the Hartmann vector $\mathbf{h}$, which is a measure of the wavefront slope. Several wavefront reconstruction algorithms exist, which can broadly be separated into *Zonal reconstruction*, in which the wavefront is calculated by numerical integration of all the slopes [74], and *Modal reconstruction*, in which a set of polynomials (such as Zernike polynomials) are defined and their coefficients fitted to the data [75].

When measuring IR and other optical[1] beams, the most common way of measuring the wavefront is using an array of microlenses instead of holes [76], referred to as a Shack-Hartmann WFS when combined with an imaging device such as a CCD camera. The lenses focus the beamlets, which increases their intensity, enhancing the signal-to-noise ratio of the measurement. The focusing also makes them smaller, enabling a higher resolution when measuring their position.

When an XUV wavefront is measured, transmissive optics such as lenses are often not a realistic option due to the XUV's previously mentioned short absorption length in most optical materials. One may therefore use an array of holes, as in the original Hartmann mask [77], or alternatively an array of zone plates [78], which act as lenses for certain harmonics. Because zone plates will only

[1] "Optical" in this sense refers to wavelength regions around the visible, where transmissive optics are viable.

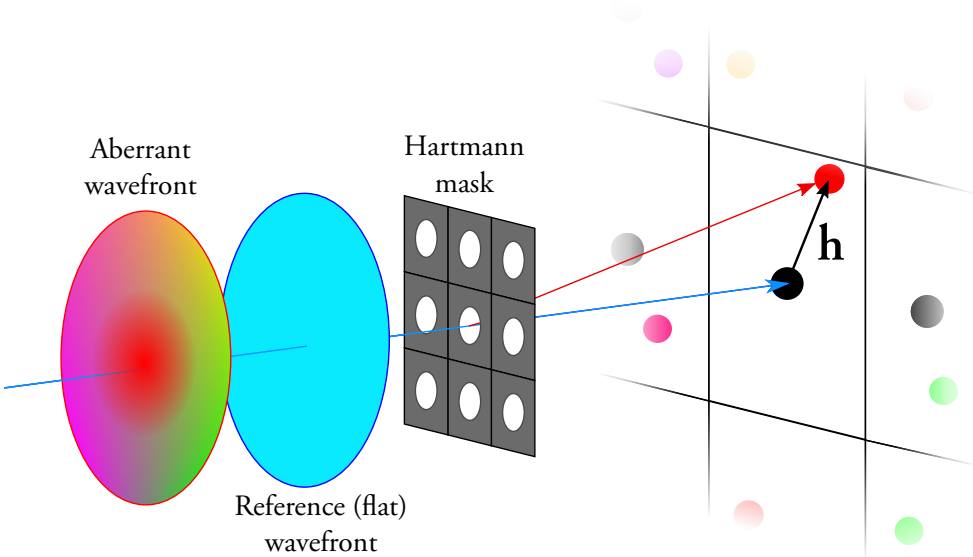

Figure 4.2: The operating principle of a Hartmann mask, showing the diffraction through the central hole of the mask for a flat reference wavefront (blue) and an aberrant wavefront (the different colors show different displacements of the wavefront). **h** denotes the Hartmann vector.

focus a certain wavelength in one plane, and this work deals primarily with broadband XUV pulses, the rest of this thesis discusses only hole arrays, as this is also the technique used for the wavefront experiments described in Papers III and VI as well as this chapter and the next one.

The downside of using this technique for broadband light, however, is that the wavefront is integrated over the spectrum, making it impossible to discern order-dependent variations in the wavefront.

There are other methods for measuring the XUV wavefront (with or without a spectral resolution) such as Spectral Wavefront Optical Reconstruction by Diffraction (SWORD) [79–81], lateral shearing interferometry [82] and point-diffraction interferometry [83]. These methods, however, aside from scanning and thus not being applicable to single-shot measurements, only provide a spatial resolution in one dimension, wherefore one has to assume a rotational symmetry of the beam. Without measuring the non-rotationally symmetric components of the wavefront (i.e. any Z_n^m where $m \neq 0$) it is hard to gauge the reliability of this assumption.

With some notable exceptions [84], one thus has to accept the trade-off between spectral and spatial resolution, possibly combining several measurements. For example, if a 2D technique such as a Hartmann mask shows a symmetric wavefront, one could perform a spectrally resolved 1D measurement with a great deal of confidence in its fidelity.

4.4 Adaptive optics

If it is known in what way the wavefront is aberrant, it is possible to compensate for this. A common method for doing so is to use a DM, a kind of adaptive optic. This element has previously proven useful in compensating for other kinds of aberrations, such as atmospheric turbulence affecting the imaging quality in optical telescopes [85]. If used in the Fourier plane of a compressor, deformable mirrors may even be used for pulse shaping and compression [86].

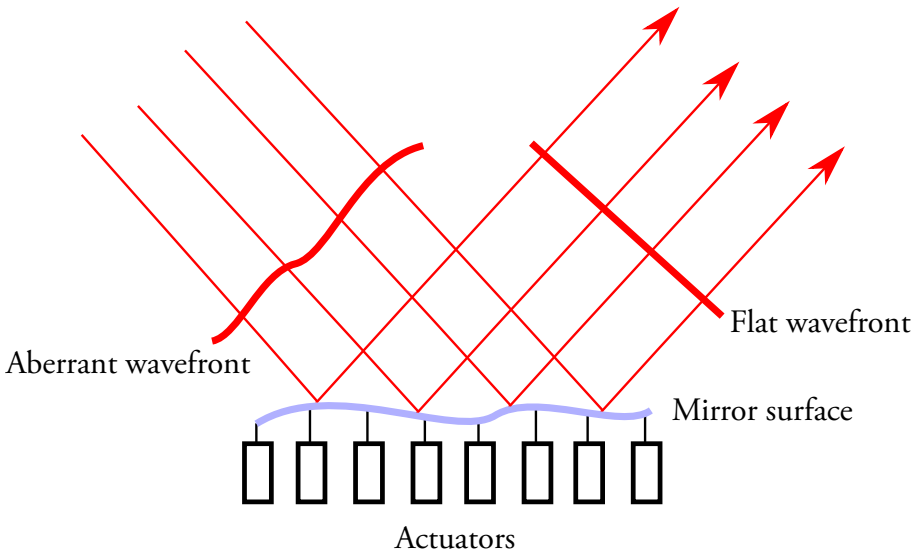

Figure 4.3: A simple schematic for the operating principle of a deformable mirror.

Figure 4.3 shows an example of how this works in principle. According to the simplest way of thinking, the slope of the wavefront is compensated by an "opposite" slope created by the deformation of the mirror surface. The mirror surface can itself be a foil or membrane [87], or a glass surface, possibly coated with a more reflective material, deformed from the back by piezoelectric actuators [88].

For most of the experiments described in this thesis and in Papers III-VI, DMs were used to correct the wavefront before the HHG process, as described further in Section 3.2.1. Paper VI also briefly demonstrates how the DM can be used to introduce wavefront aberrations in a controlled manner.

4.5 Dipole phase curvature

4.5.1 Harmonic wavefront curvature

The harmonic wavefronts can be studied with the help of the previously described new formulation of the harmonic dipole phase [33], presented in Section 2.2.5, in combination with Gaussian optics [89], as discussed in Paper V. Note that the derivations here assume cylindrical symmetry around the z axis and an ideal Gaussian wavefront (free of aberrations with only a symmetric r^2 term).

Considering the contribution for a single trajectory i, the phase of the q:th harmonic can be written as

$$\Phi_q(r,z) = q\phi(r,z) + \Phi_i(r,z). \tag{4.15}$$

Recalling Equation (4.1), the spatial phase of the fundamental is

$$\phi(r,z) = kz - \xi(z) + \frac{kr^2}{2R(z)}. \tag{4.16}$$

The third term describes the curvature of the beam. Using $\Phi_i(r,z)$ from Equation (2.18) with $I = I(r,z)$ as the spatially dependent IR intensity and $\Omega = q\omega$ (q times the fundamental frequency), and omitting the second term (as it is independent of intensity and thus also of z), the spatial dipole phase can be expressed as

$$\Phi_i(r,z) = \frac{\alpha_i I_0 \omega_0^2}{\omega^2(z)} e^{-\frac{2r^2}{w^2(z)}} + \frac{\gamma_i(\Omega-\Omega_\mathrm{p})^2 w^2(z)}{I_0 w_0^2} e^{\frac{2r^2}{w^2(z)}}. \tag{4.17}$$

In order to approximate this analytically, one can perform a Taylor analysis around the center of the beam (i.e. $r \approx 0$). Only the r^2 dependent components will contribute to the wavefront curvature, as will the fundamental contribution $qkr^2/2R(z)$. Thus the total r^2-dependent phase component is $qkr^2/2R_i$, where

$$\frac{1}{R_i(z)} = \frac{1}{R(z)} - \frac{4\alpha_i I_0 w_0^2 c}{w^4(z)\Omega} + \frac{4\gamma_i(\Omega-\Omega_\mathrm{p})^2 c}{I_0 w_0^2 \Omega}. \tag{4.18}$$

Consequently, one can simply add the curvature of the fundamental to that added by the dipole phase contributions.

Introducing the reduced coordinate

$$Z = \frac{z}{z_0}, \tag{4.19}$$

where z_0 is the Rayleigh length as defined in Section 4.1, Equation (4.18) can be rewritten as

$$\frac{z_0}{R_i(z)} = \frac{1}{Z + 1/Z} - \frac{\eta_i}{(1+Z^2)^2} + \mu_i, \tag{4.20}$$

where $\eta_i = 2\alpha_i I_0/q$, $\mu_i = 2\gamma_i\omega^2(q-q_p)^2/qI_0$ and $q_p = I_p/\omega$. Since for the short trajectory $a_i = a_\mathrm{s} = 0$, the second term vanishes[2] and the positions where $R_i(z) \to \pm\infty$, i.e. the focus

[2] This also has the interesting effect that, since μ_i is not z dependent, the dipole phase-induced curvature is constant for the short trajectories, as seen in Figure 4.4 (a).

positions, can be determined by calculating the roots of the equation

$$Z^2 + \frac{Z}{\mu_s} + 1 = 0, \tag{4.21}$$

which for $\mu_s \leq 0.5$ are real and found by

$$Z_\pm = -\frac{1}{2\mu_s} \pm \sqrt{\frac{1}{4\mu_s^2} - 1}. \tag{4.22}$$

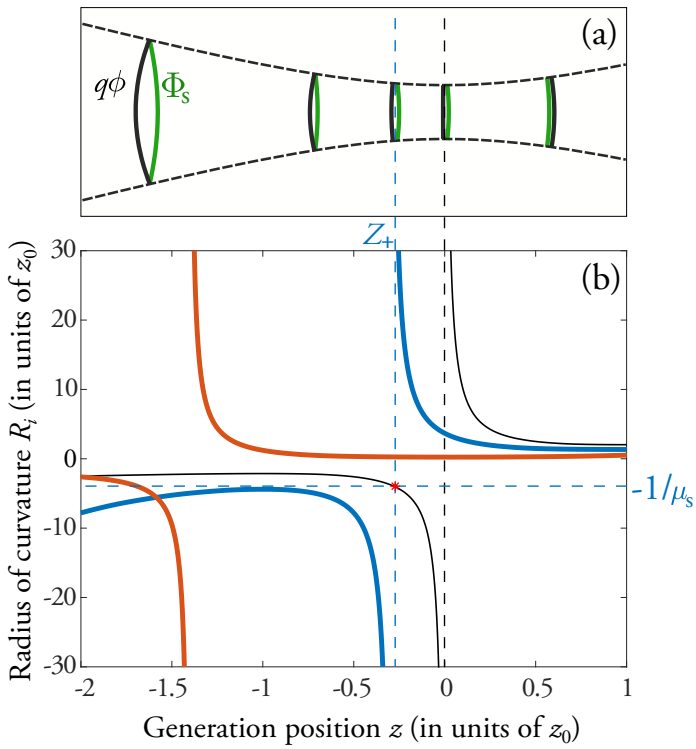

Figure 4.4: (a) The curvature of the fundamental IR field $q\phi$ and the curvature introduced by the dipole phase Φ_s for the short trajectory. Note that the curvature from Φ_s is actually constant over z.
(b) The radii of curvature of the fundamental beam (black), short trajectory (blue) and long trajectory (red) for the 23rd harmonic. The analytically found Z_+ is shown to coincide both with where the fundamental field curvature is equal to $-1/\mu_s$ and with where the two curvatures can be seen to be equal in (a). Figure adapted from Paper V.

For the long trajectory, these positions are found by calculating the radius of curvature $R(z)$ for each generation position and finding the position(s) at which it diverges, which is obviously also possible for the short trajectory. This can be seen in Figure 4.4, where the calculated radii are shown along with the "analytically" determined Z_+ value (Z_- is outside the range of the figure to the left) for the 23rd harmonic in argon, assuming a peak intensity of $3 \cdot 10^{14}$ W/cm^2.

In order to use the formulation of Gaussian beams to calculate the other properties of the generated harmonics, it is necessary to have knowledge of the harmonic width at the generation position. Since the amplitudes of the harmonics reflect the amplitude profile of the fundamental beam (only the sufficiently high intensities in the middle of the beam contribute to this nonlinear process), it is assumed to be proportional to the fundamental amplitude to the power p [90–94]. The width then depends on the fundamental width as $W(z) = w(z)/\sqrt{p}$, with p chosen to be 4 based on TDSE calculations performed as part of Paper V.

Note that $W(z)$ is trajectory independent since generation takes place at z regardless of the trajectory. It is also practically order-independent in the plateau region.

4.5.2 Harmonic focus position and divergence

Using the above stated parameters, the focus position (relative to generation) can be determined, following Equation (4.7), as

$$z_i(z) = -\frac{R_i(z)}{1 + \left(\frac{\lambda_q R_i(z)}{\pi W(z)^2}\right)^2}, \tag{4.23}$$

where $\lambda_q = \lambda/q$. In a similar manner, following Equation (4.8), the harmonic waist[3] w_i can be calculated as

$$w_i(z) = \frac{W(z)}{\sqrt{1 + \left(\frac{\pi W(z)^2}{\lambda_q R_i(z)}\right)^2}}. \tag{4.24}$$

For convenience, these parameters can be made "dimensionless" using reduced coordinates in a similar manner as before, in which case the harmonic focus position in terms of the fundamental Rayleigh length becomes

$$\frac{z_i}{z_0} = -\frac{R_i}{z_0}\left(1 + \left[\frac{pR_i}{qz_0(1+Z^2)}\right]^2\right)^{-1}, \tag{4.25}$$

and the harmonic waist in terms of the fundamental waist is

$$\frac{w_i}{w_0} = \left(\frac{1+Z^2}{p}\right)^{\frac{1}{2}}\left(1 + \left[\frac{qz_0(1+Z^2)}{pR_i}\right]^2\right)^{-\frac{1}{2}} \tag{4.26}$$

Figure 4.5 provides the focus position and waist size of the short trajectory for harmonic orders 31 to 71 in neon (assuming an intensity of $I = 5 \cdot 10^{14}$ W/cm^2, as a higher intensity is typically used for neon compared to argon). Neon was used in place of argon to show the effects discussed more clearly (as neon tends to have a broader and flatter harmonic spectrum than argon), but to some extent these effects are present regardless of the generation conditions.

[3]Note here the omission of the 0 from w_0 for aesthetic reasons, explaining the previous change of symbol for the width to $W(z)$ to avoid confusing the waist with the width.

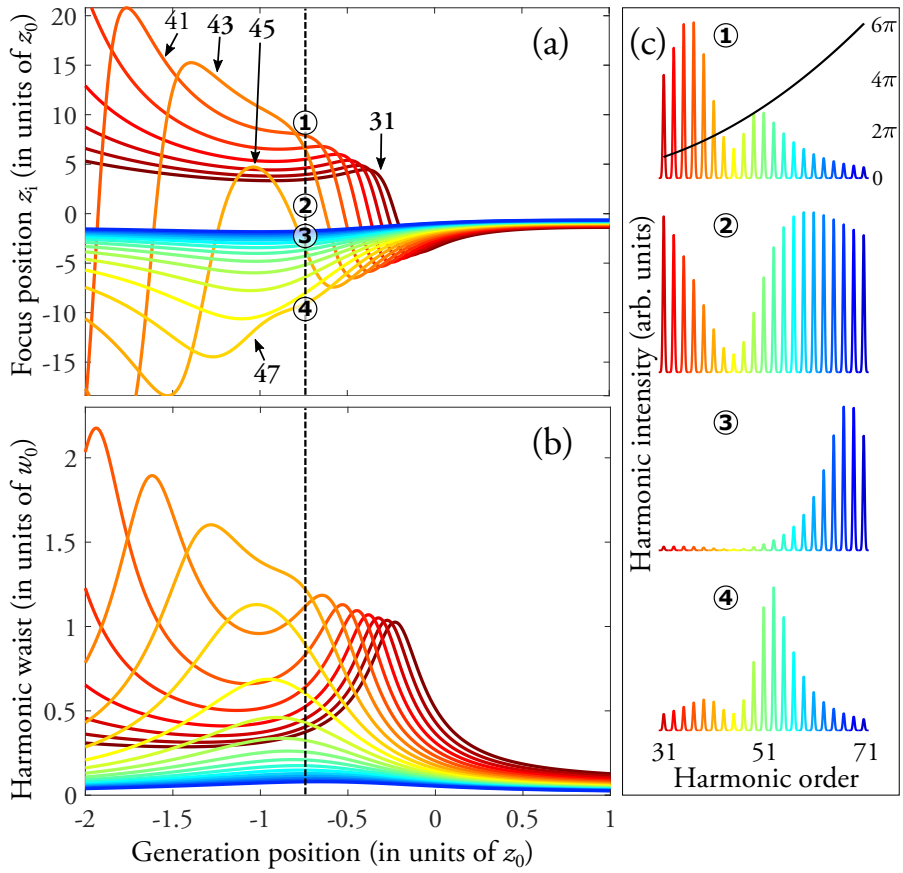

Figure 4.5: (a) The focus position and (b) the waist size of harmonics 31 to 71 in Ne. The harmonics are identified by color, as shown by the x axis of the spectra in (c). The black line in plot ① in (c) shows the on-axis dipole phase. Figure adapted from Paper V.

As can be seen in the figure, the focus position varies strongly with the order for most generation positions, in some cases with a virtual focus before generation (negative z_i values) and in some cases with a real focus after generation, i.e. created with a converging wavefront. This variation is especially dramatic for generation positions before the IR focus, which is the most common when generating harmonics in a loose focusing geometry [13, 95] for phase matching reasons (see Section 2.3.1 for some expansion on this). For example, at the generation position marked by the dashed line, $z = -0.75\, z_0$, the difference between harmonic orders 41 and 47 is almost 20 Rayleigh lengths.

At the same position, the waist size also depends significantly on the order: the waist size of harmonic 45 is almost 25 times larger than that of harmonic 71.

For some (if not most) generation positions, the combination of varying focus positions and waist sizes (i.e. harmonic divergence) means that in some respects the harmonics are not propagating

as one beam, easily controlled and focused, but as a superposition of sometimes wildly varying beams that may occasionally render a focus with the full bandwidth of the harmonic spectrum, but at other times contain a much more narrow spectrum. This is illustrated in Figure 4.5 (c), where the spectrum is shown for four different "detector positions" along the axis of the harmonic focus positions.

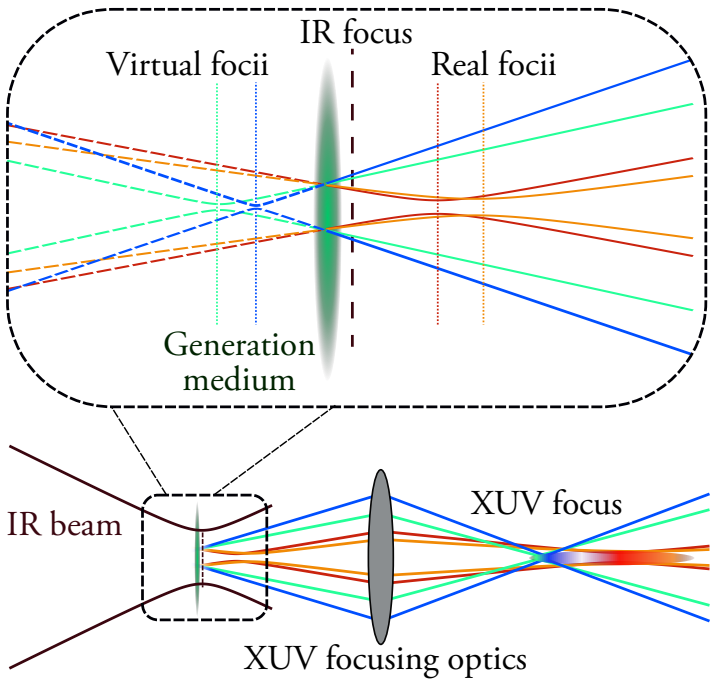

Figure 4.6: An illustration of the chromatic aberration following from the wavefront variations caused by the dipole phase contribution. Figure adapted from Paper V.

Figure 4.6 illustrates the consequences this may have for some of the harmonics shown in Figure 4.5 (following the color code of (c)), propagated as Gaussian beams and then focused. Some harmonics have foci after the point of generation and some before, resulting in a stretched and chromatically aberrated focus when the generation point is imaged. Thus, for applications and experiments that require high-intensity, broadband attosecond pulses, great care must be taken to minimize this chromatic aberration or otherwise compensate for its effects.

4.5.3 Order-dependent divergence experiment

In order to test the "Gaussian" model of order-dependent harmonic wavefronts, an experiment was set up to measure the width of harmonics on the XUV spectrometer. This was done by integrating the spectrum around each harmonic and then fitting a Gaussian function onto the transverse profile.

Figure 4.7 (a) shows the harmonic width as a function of generation position for several harmonics. (c) shows the results of the Gaussian model and (b) a simulation based on numerically solving the

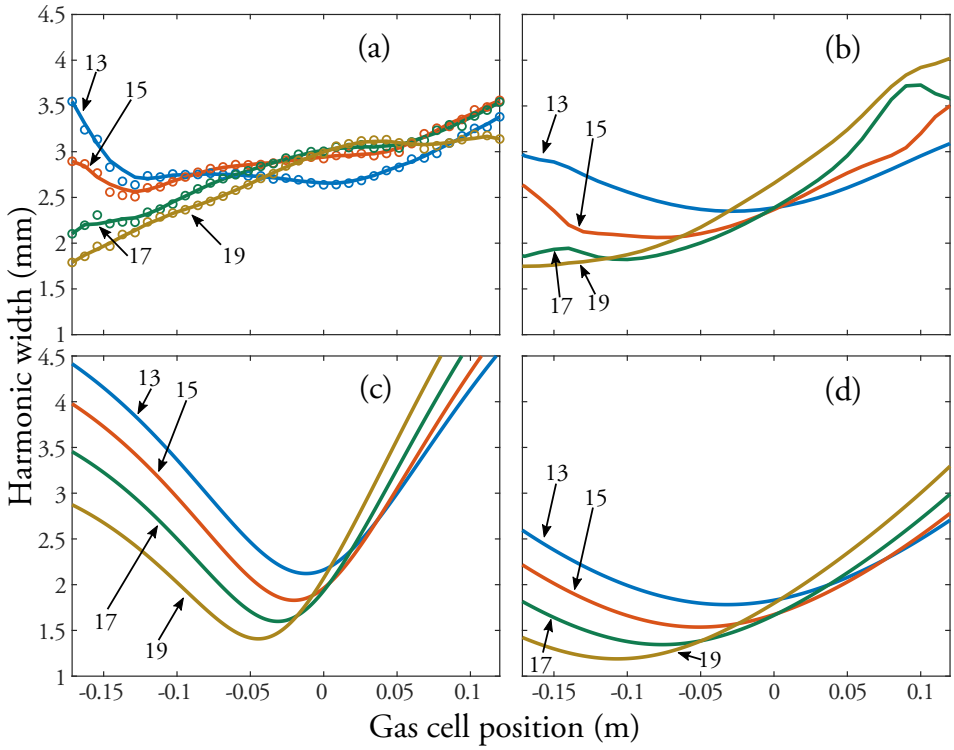

Figure 4.7: The harmonic widths of four low-order harmonics, from Paper V: (a) the measured width, (b) a numerical simulation by TDSE and propagation equations, and analytical simulations, based on (c) the purely Gaussian model and (d) a truncated Gaussian.

TDSE and propagation equations for conditions as close as possible to the experimental conditions.

For each harmonic and each generation position, the harmonic divergence was calculated from the waist, and then multiplied by the distance from the point of generation to the spectrometer.

There is obviously some discrepancy between the Gaussian model on one hand, and the experimental values and numerical simulation on the other. By varying the parameters of the numerical simulation, it was determined that the most important cause of this discrepancy was an aperture, introduced in the TDSE model to simulate the clipping of the beam by the iris before vacuum.

Based on this finding, the Gaussian model calculations were redone, as shown in (d), using a clipped Gaussian beam propagated into the focus [96] as a fundamental beam. This leads to much better agreement with the experiment and the TDSE calculations, while still being very lightweight (as the model is analytical).

The fact that the Gaussian model (albeit with some modifications) is seen to agree so well with both the experiments and the fully quantum mechanical calculations supports the conclusion of the article, namely that the chromatic aberrations and spatiotemporal couplings predicted using this model should be taken into account when attempting to focus broadband, ultrashort pulses.

4.6 Single shot, generation-dependent XUV wavefronts

As described in Paper VI, the LOA / Imagine Optic wavefront sensor was used for an in-depth study into how the characteristics of the harmonics were affected by generation parameters such as pressure, intensity and aperture size, as well as the possible transfer of aberrations from the fundamental IR field into the XUV. For this campaign, most measurements were taken on a single shot basis, so that the wavefronts are not averaged (pointing instabilities may cause a spatial smearing if several wavefronts are averaged).

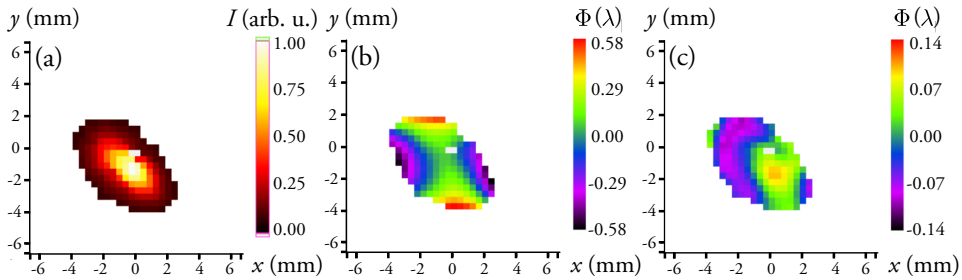

Figure 4.8: (a) The intensity profile and (b) wavefront of a typical single-shot image. (c) The wavefront with the astigmatism numerically removed. Figure adapted from Paper VI with permission from the OSA.

Figure 4.8 shows the result of a typical single-shot acquisition of a harmonic wavefront using the WFS, and the information that can be extracted: (a) the intensity profile and (b) the wavefront. In (c), one can see the wavefront with the astigmatism numerically removed, i.e. only higher-order aberrations are displayed. The fact that this wavefront was much cleaner (comparing the magnitude of errors) indicates that the astigmatism was the main error present. The λ used to express the wavefront error is that of the 19th harmonic, deemed to represent the weighted average of the spectrum [77].

Figure 4.9 shows the effect on the harmonic wavefront, and harmonic yield, of scanning four generation parameters: driving laser pulse energy (a), aperture size (inversely proportional to the *f* number) (b), gas cell backing pressure (c), and the GDD of the compressor, corresponding to the pulse duration of the IR (d). The harmonic yield is given as APT energy, meaning that the energy of all the harmonic pulses in the APT is added together.

One conclusion from these scans was that for each parameter there is an optimum point to achieve the best XUV wavefront, and this is not necessarily the optimum point for harmonic yield. Thus there is a certain trade-off between sheer number of photons and focusability that needs to be taken into account when a high intensity is desired.

Figure 4.10 shows the wavefronts of individual harmonics, orders 19, 23 and 33. These were acquired by reflecting the XUV light on specially constructed Multi-Layer Mirrors (MLMs)[4] into the CDI chamber described in Section 3.6. These mirrors were characterized before the experiment, so that their effects on the wavefront could be accounted for. In this figure, the wavefront error is given

[4] See Section 5.1 for a discussion on XUV optics.

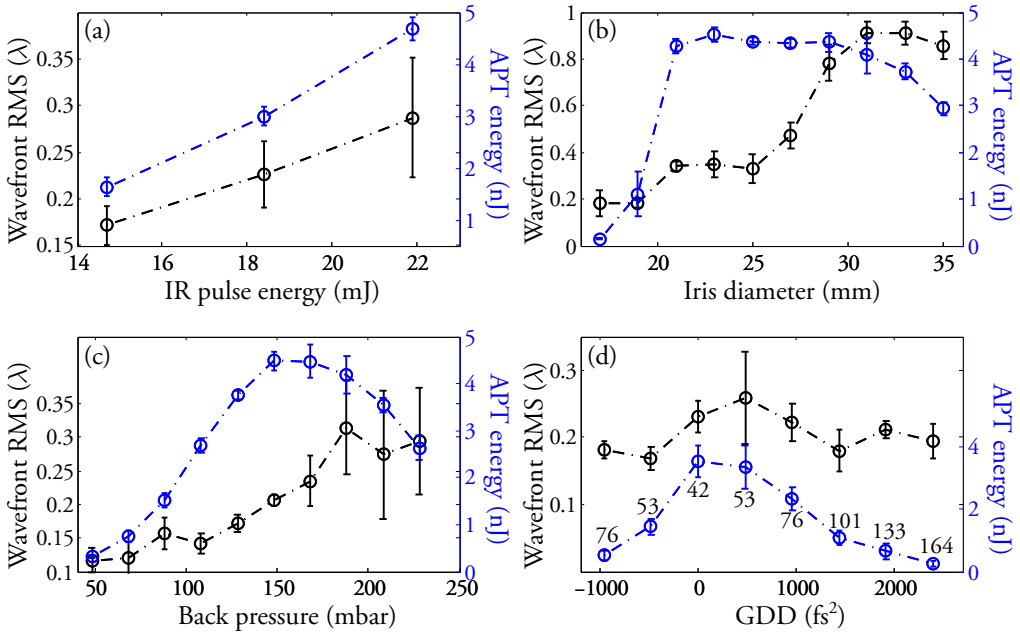

Figure 4.9: Wavefront error (black) and attosecond pulse train energy (blue) as a function of (a) driving field energy, (b) aperture size, (c) gas cell backing pressure and (d) compressor position (the numbers above each measurement point correspond to the approximate pulse duration in fs at each GDD). Figure adapted from Paper VI with permission from the OSA.

in terms of λ_q, where q is the harmonic order. In addition to the intensity profiles and wavefronts, this figure also portrays the beam profiles of the sources of the XUV light, calculated in a similar manner as in Section 5.3.

As can be seen, the 33rd harmonic has a wavefront quality that is inferior to the others. One explanation for this is given by Figure 4.9: in order to generate the 33rd harmonic at all, the generation conditions had to be pushed to a regime with severe wavefront deterioration (such as high energy, short pulses, etc.)[5].

[5]Recall, from Section 2.2.1, that the cutoff energy is dependent on the intensity of the IR field.

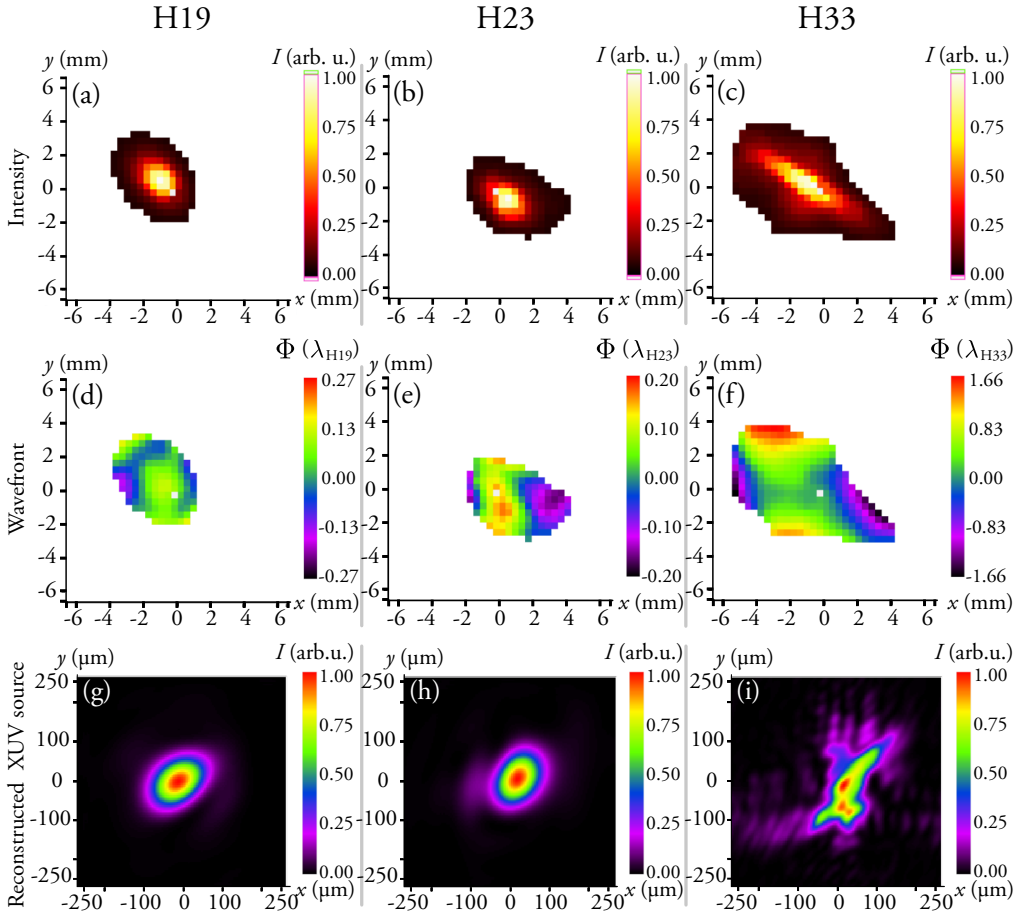

Figure 4.10: (a, b, c) The intensity profiles, (d, e, f) wavefronts, and (g, h, i) calculated source profiles of harmonics 19, 23 and 33. Figure adapted from Paper VI with permission from the OSA.

4.7 MCP IR filter characterization

The Lund wavefront sensor was used to study the effects of employing a single-layer MCP as a filter to extinguish the IR beam while preserving the XUV. The periodic structure of the MCP enables it to function like a transmission grating for the XUV, but the hole structure is too fine to admit the IR light [97]. The 0th order was studied, as this is where all harmonics co-propagate. The MCP was mounted on a translation stage after the single silica plate described in Section 3.3.1.

The XUV transmission had been studied before but not much was known as to how the XUV wavefront would be affected by transmission through this kind of structure. Thus a series of wavefront measurements were taken, 100 images with the MCP in the beam and 100 images without as a reference (as the beam could not be expected to be completely without aberrations, this was necessary to identify the effects of the MCP). Figure 4.11 shows the Zernike polynomial coefficients of the

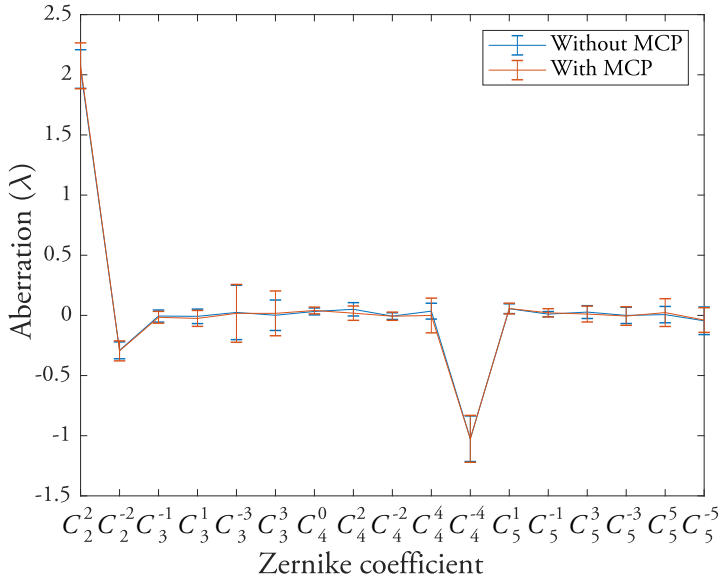

Figure 4.11: Wavefront aberrations for the beam with and without an MCP filter.

first higher-order aberrations; the tilt and focus components were also included in the analysis but are not shown here as they were virtually identical for the two measurements.

As can be seen in the figure, any difference between the two is within the error bars, so it was concluded that the wavefront is not adversely affected by the MCP filter to a significant degree.

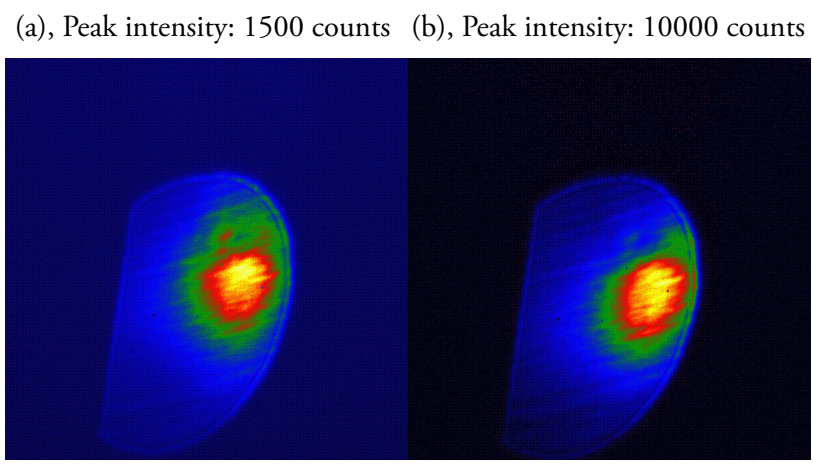

Figure 4.12: Andor images showing the XUV beam profile (a) with and (b) without the MCP filter.

Beam profiles of the XUV beams with and without the XUV filter were also studied, and can be seen in Figure 4.12. Aside from the profiles looked similar (indicating that the MCP does not

cause a distortion of the beam profile), the linear energy response of the Andor camera[6] made it possible to estimate the XUV transmission. According to these measurements, the MCP filter has a transmission (in the 0th order) of around $15 - 20\%$, which corresponds well with previous measurements.

To enable the Andor image without an MCP, an aluminium filter was mounted in front of it in the interferometer chamber. This also protected the MCP from the full IR power of the intense XUV beamline. It is not known whether it would withstand this, but in the case of higher repetition rate sources with lower pulse energy [98] it works well. In that case it also finds a second purpose, as a differential pumping section between the HHG chamber and the subsequent parts of the beamline. This is useful since, as discussed in Section 2.3.2, for a lower IR pulse energy the length of focusing goes down and the pressure goes up to preserve phase matching, necessitating a steeper pressure gradient in the HHG setup.

[6] See Section 3.5.4 for more information on the camera itself.

Chapter 5

Focusing high-order harmonics

In order to efficiently use the XUV light created in the HHG process, it often has to be refocused. This may be because the target of interest is very small [99] or because a high intensity is needed, for example if multiphoton interactions are required [100].

In order to efficiently focus broadband XUV light, it must be reflected on curved optics at grazing incidences. As will be shown in this chapter, this often introduces aberrations in the wavefront, leading to suboptimal focusing conditions. However, these aberrations can be overcome using combinations of curved surfaces, as is demonstrated for the intense XUV beamline, where two toroidal mirror are used in a Wolter-like configuration.

5.1 XUV optics

The high photon energy of the XUV light causes the absorption cross section to be high for most materials. In this sense, this wavelength regime is quite particular; for longer wavelengths such as visible and IR light, many materials such as glasses are transparent, as is the case for most substances at shorter wavelengths (going into the hard X-ray regime).

Transmissive optics are commonly used for a wide range of applications such as focusing and imaging the light, manipulating its polarization, and separating its wavelength components. They are not possible in the case of XUV light, so these operations must be carried out using reflection of the light. However, reflection of XUV light is also far from trivial.

In the case of s polarization, for example[1], the reflection at a boundary from vacuum to a material

[1] The p polarization has a different expression but the conclusions are largely the same.

can be found from the Fresnel equations as [101]

$$R_s = \frac{\left|\cos\theta - \sqrt{n^2 - \sin^2\theta}\right|^2}{\left|\cos\theta + \sqrt{n^2 - \sin^2\theta}\right|^2}, \tag{5.1}$$

where θ is the incidence angle and n is the refractive index of the material.

What makes the case of XUV radiation special is that for most materials, at these photon energies n is complex and has a real component very close to unity (often even slightly smaller). This means that at angles close to normal incidence the reflection is minor. Figure 5.1 shows the angle-dependent reflection coefficients of three common optical materials (aluminium, gold and fused silica) for XUV light with a wavelength of 42 nm, corresponding to the 19th harmonic of an 800 nm IR laser beam.

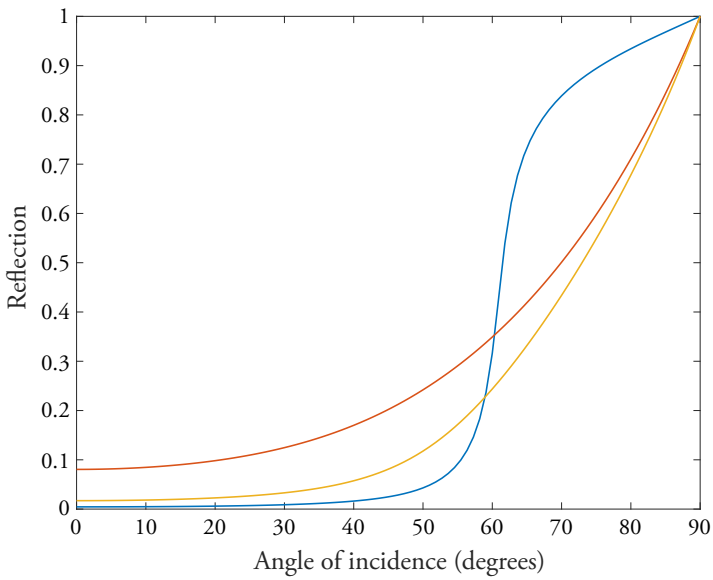

Figure 5.1: Reflection as a function of the angle of incidence (0° is normal incidence) for aluminium (blue, [102]) gold (red, [103]) and fused silica glass (yellow, [104]) for s-polarized 42 nm light.

As seen in Figure 5.1, using reflective optics at normal incidence leads to a loss of $90 - 99\%$ of the XUV light, depending on the material. As is discussed in Section 2.3.2, generating a large amount of XUV photons is quite a challenge in itself, so one needs to preserve what one has to the greatest extent possible.

Rather than use bulk materials for reflective optics, one option is to use multi-layer coated optics, referred to as MLMs. These consist in an extremely flat substrate onto which thin layers (often $5-10$ atoms) of varying materials are adsorbed in sequence [105]. For a given angle and wavelength, these mirrors can have reflectances of over 50% with the help of Bragg reflection [106].

One notable feature of these MLMs is that they tend to work in a very narrow spectral region. This

can be useful for some applications, for example in which a narrow spectrum is needed for exciting or probing certain energy levels, or in some imaging applications, but for ultrashort pulses reducing the bandwidth of the pulse generally leads to a longer pulse duration, as discussed in Section 2.1.

5.2 Wavefront and focus

There is an interplay between the wavefront quality of a beam and its focus: a high-quality wavefront is necessary for a small and well-defined focus, but at the same time, focusing optics may themselves introduce aberrations into the wavefront.

Focusing optics

As described in the previous section, most transmitting optics are not possible for XUV beams. Furthermore, the poor reflectivity at normal incidence means that the optics must also be used at grazing incidence (close to parallel with the surface rather than the normal) in order to preserve XUV flux [107].

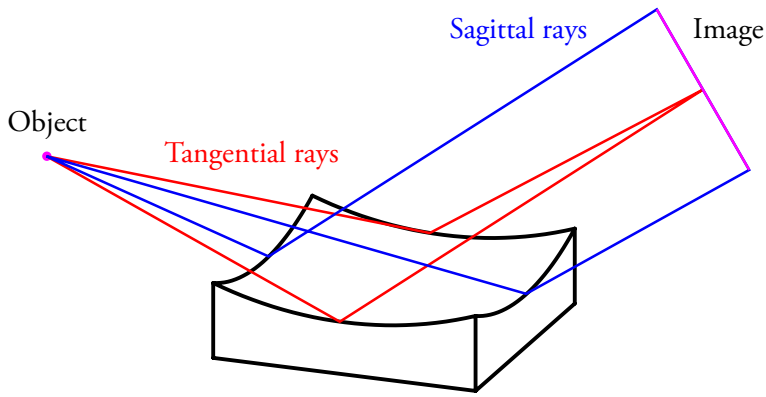

Figure 5.2: Imaging of an object using an off-axis spherical mirror. As can be seen from the difference in shape between the object and image, this imaging is not optimal.

The necessity of reflective focusing optics at grazing incidence gives rise to certain challenges. Many of these optics will introduce strong aberrations into the beam if not used at normal incidence or imaging points outside the exact focus [108, 109]. As illustrated in Figure 5.2, a spherical mirror with a radius of curvature R, for example, will have sagittal and tangential focal lengths depending on the angle of incidence as

$$\begin{aligned} f_T &= \frac{R \sin\theta}{2} \\ f_S &= \frac{R}{2 \sin\theta} \end{aligned} \tag{5.2}$$

As an example, a grazing angle of 10° (corresponding to an angle of incidence of 80° in Figure 5.1) leads to a sagittal focal length that is 33 times larger than its tangential counterpart, corresponding to a focusing that is much weaker in the sagittal plane. This can thus be seen as an extreme case of astigmatism.

In principle, an elliptical mirror leads to an ideal focus regardless of the angle [109], but only from one of its foci to another. In the practical case, one will never have a true point source of light. Even a small displacement from this focal point will causes a strong coma aberration. In addition to this, the surface is difficult to manufacture [110, 111].

Another solution is to combine several mirrors. The first truly successful focusing of X-rays[2] was achieved using the X-ray microscope of Kirkpatrick and Baez, which introduced the Kirkpatrick-Baez configuration of mirrors [110]. In this configuration, two spherical mirrors, with their axes orthogonal to each other, are arranged so that their respective (tangential) foci end up in the same position.

A toroidal mirror, which can have different radii of curvature in the tangential and sagittal planes, can in principle focus at an angle it is designed for (but will have strong aberrations at other angles, since the focal lengths will no longer overlap). However, a single toroidal mirror at grazing incidence will still have coma aberrations as it cannot satisfy the Abbe sine condition, which states that the sine of the angles of in- and outgoing rays should be proportional. One conclusion from the sine condition is that the so-called principal surface, where the rays would intersect when traced through the optic, should be spherical and normal to the incident rays [107].

Wolter showed [61] that certain pairs of conic sections such as ellipsoidal, paraboloidal and hyperboloidal surfaces with foci in the same plane can in principle create aberration-free images [112]. The Abbe sine condition is nearly satisfied, thanks to the principal surface being a virtual surface "between" the two actual mirror surfaces. As mentioned before, these surfaces are very difficult to manufacture, but toroidal mirrors, being local approximations to an ellipsoidal surface [111], can be used in "Wolter-like" configurations (which will be referred to as Wolter configurations for simplicity).

Focus characterization

If the wavefront and beam profile are completely characterized in the far field, they can be used to calculate the size, shape and position of the focal spot by means of diffraction integrals [35].

A useful quantity when discussing the focus is the Strehl ratio, which expresses the peak intensity of the beam as a ratio of the peak intensity of an ideal focus without the aberrations present in the beam [113]. Thus, a Strehl ratio of 1 corresponds to a perfect focus.

[2] Most of the techniques mentioned in this section originated in the X-ray domain, since X-rays and XUV light pose the same kinds of challenges. One can often assume that a (reflective) technique that works for shorter-wavelength light will also work for the XUV.

5.3 Micro-focusing

An experiment was performed, using the LOA / Imagine Optic wavefront sensor, with the goal of optimizing the focusing at the intense XUV beamline. As detailed in Paper III, the aberrations introduced by toroidal focusing optics of the intense XUV beamline were studied, as well as how to use the optics to minimize the XUV focus size in order to maximize the intensity.

An interesting conclusion was that not only could the aberrations introduced by the toroidal mirrors be minimized, they could even be tuned to counteract the aberrations already present in the XUV wavefront.

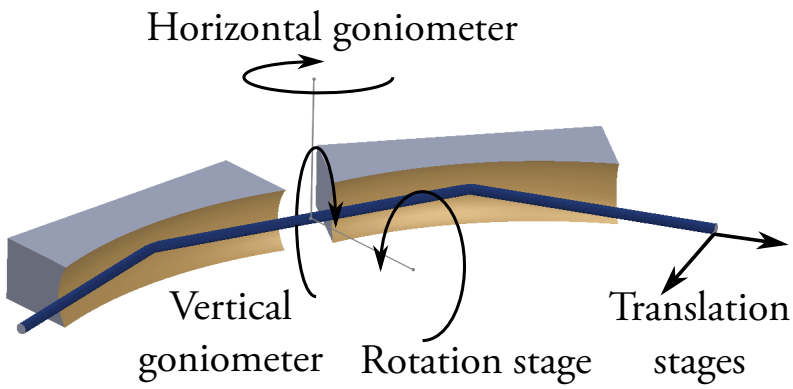

Figure 5.3: A sketch of the two toroidal mirrors of the Wolter focusing setup, with the actuators available for controlling its alignment. Figure adapted from Paper III.

The two mirrors are mounted together in the "C" Wolter-like configuration [61, 111]. Here, the two mirrors are fixed relative to one another in such a way that the comatic aberrations (caused by off-axis reflections in a curved mirror) of the two mirrors compensate each other. Figure 5.3 shows the manipulators for the Wolter optics. Only the rotation stage and goniometers will be discussed further, as the translation stages are not expected to have the same impact on the harmonic wavefront.

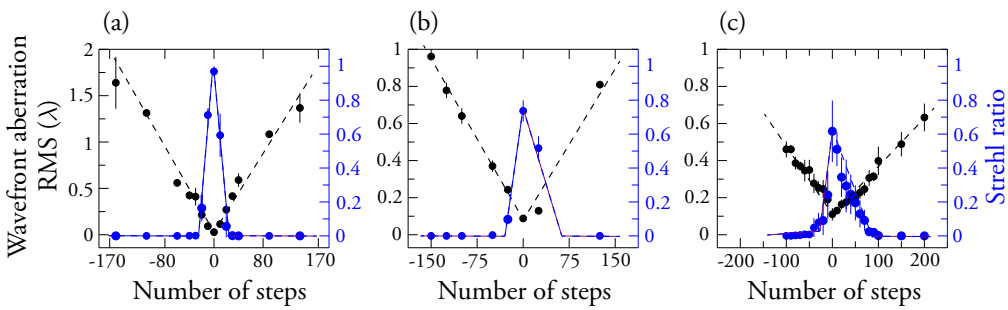

Figure 5.4: The total wavefront RMS error (black) and Strehl ratio (blue) when moving (a) the rotation stage, (b) the horizontal goniometer, and (c) the vertical goniometer. Figure adapted from Paper III.

The impact on the wavefront of moving these actuators can be seen in Figure 5.4, where the total wavefront error RMS and the Strehl ratio (as discussed in Section 5.2) are plotted for a certain amount of steps of movement of (a) the rotation stage, (b) the horizontal goniometer, and (c) the vertical goniometer.

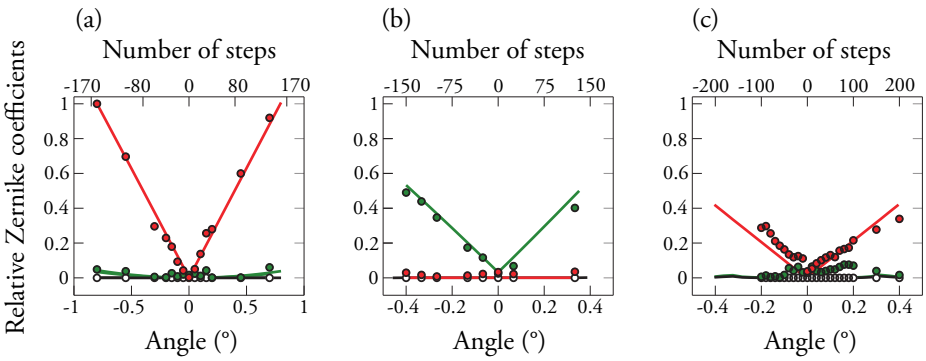

Figure 5.5: The Zernike coefficients for 0° astigmatism (green), 45° astigmatism (red), and coma (black), as a function of moving (a) the rotation stage, (b) the horizontal goniometer, and (c) the vertical goniometer. Figure adapted from Paper III.

Figure 5.5 shows the same movement steps as Figure 5.4, but this time the effect of the movement is resolved in terms of the Zernike coefficients of the low-order aberrations, 0° and 45° astigmatism and coma. As clearly seen in the figure, the rotation stage almost exclusively affects the magnitude of the 45° astigmatism, while the horizontal goniometer only has an effect on the 0° astigmatism component. The coma is not affected much by any movement, as intended by the design[3].

The fact that two actuators can each affect a respective aberration more or less independently is highly useful, since this means that both aberrations can be minimized. An interesting effect of this is that not only can the aberrations introduced by the focusing optics be minimized, but the optics can also be tuned to reduce the aberrations present in the XUV wavefront even before focusing, leading to an improved quality and reduced size of the focal spot. Figure 5.6 shows the result of this improvement, where (c) shows the wavefront measured after the diagnostics chamber (see Figure 3.2), i.e. before the focusing optics, and (d) shows the wavefront after focusing.

Given the greatly reduced aberrations seen in Figure 5.6 (d), it seemed likely that the focusing would be improved. To study this, the wavefront and intensity profile were used to calculate the focal spot profile by use of a 2D Fourier transform.

[3] See the previous section.

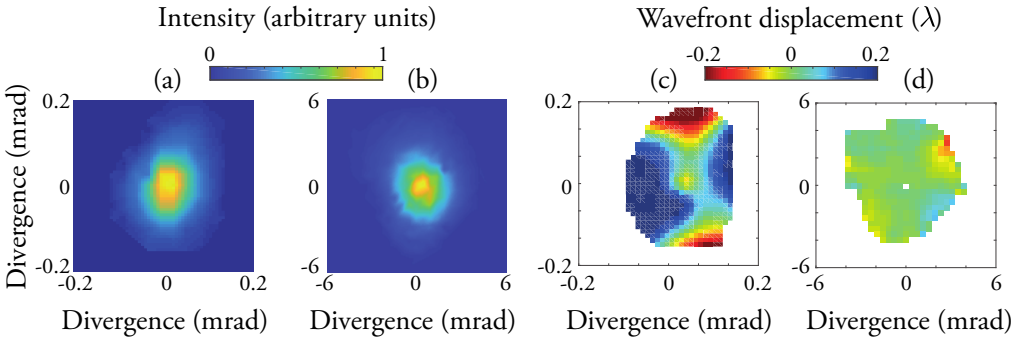

Figure 5.6: (a) The far field beam profiles and (c) wavefronts of the beam before the focusing optics, and (b,d) after. Comparing with Figure 4.1, the wavefront in (c) can be seen to have a quite strong 0° astigmatism. Figure adapted from Paper III.

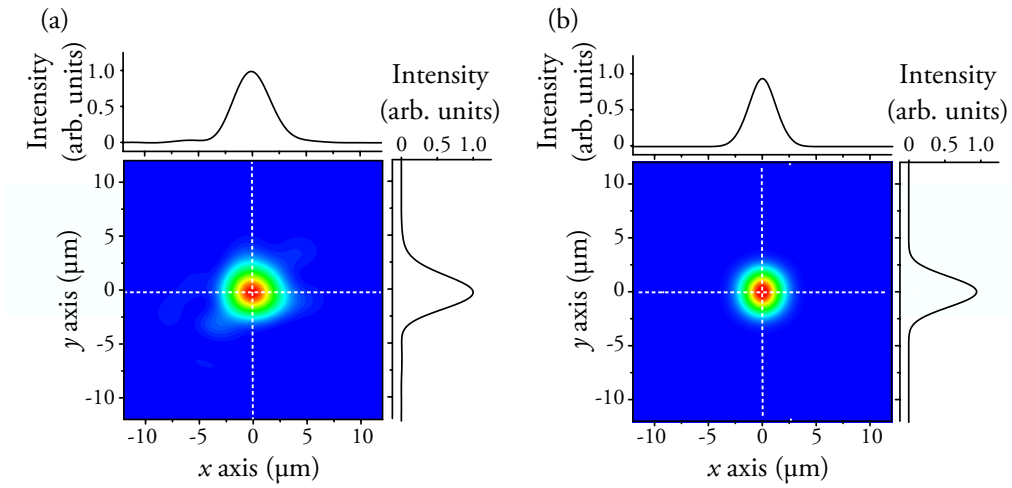

Figure 5.7: The focal spot profile, back-calculated from the far-field wavefront measurement (a) and simulated (b). Figure adapted from Paper III.

Figure 5.7 shows (a) the calculated focus, contrasted with (b) the ideal focus of the Wolter focusing optics, as modelled using the FRED™ raytracing software[4]. The FWHM of the calculated focal spot is 4.0×3.6 μm^2, to be compared with 3.2×3.0 μm^2 for the simulated focus.

As can be seen, the shape is nearly isotropic. The size is slightly larger compared to the ideal focus, but apart from suboptimal focusing this could also be explained by the divergence assumed in the FRED calculations varying slightly from the real-world case.

[4]The appendix of [111] has a good overview of raytracing using this software, especially its use for coherent raytracing using Gaussian beam decomposition [114].

5.4 Automatic focusing optics optimization

The analysis software for the Lund WFS was connected to the control unit for the focusing optics actuators described in the previous section (Figure 5.3). By letting the analysis software control the mirror mount's rotation and translation axes while taking wavefront measurements, this proved to be a nearly automatic way of optimizing the harmonic wavefront.

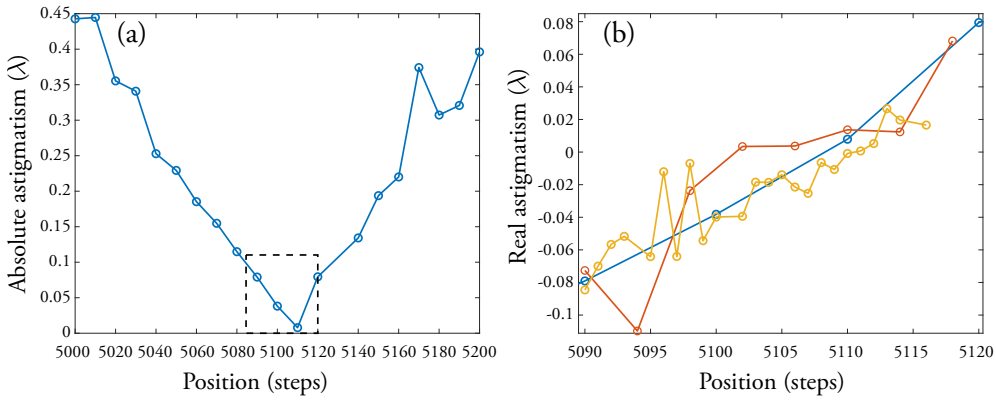

Figure 5.8: Coarse (blue) and finer (red and yellow) scans of the rotation axis, showing the coefficient for 45° astigmatism (as $|C_2^{-2}|$ for (a) and C_2^{-2} for (b)). The dashed box in (a) shows the axes of (b).

Figure 5.8 shows the results on the 45 degree astigmatism of (a) a coarse scan and (b) finer scans of the rotation stage axis, in terms of the Zernike coefficient C_2^{-2} from Equation (4.12). In (a), the absolute value of the astigmatism coefficient is shown to emphasize the similarity to the rotation scan plotted in Figure 5.5 (a). In (b) the real values are used, to show the zero crossing more clearly. As can be seen, the response is clearly linear in the coarse scan (dark blue circles), and seems to be linear, albeit more noisy, in the fine scan. This corresponded to the conclusions from using the LOA / Imagine Optic WFS mentioned previously.

By comparing the increasingly fine scans, some conclusions can be made about the measurements. The difference between the consecutive scans (blue-red-yellow) gives an indication of the backlash of the actuators controlling the mirrors. The deviations from a straight line, especially evident for the finest (yellow) scan, shows the approximate shot-to-shot reproducibility of the wavefront analysis.

A measurement of the Ne^{2+} yield similar to that described in Section 6.3.1 and Paper I showed an increase in the yield after focal spot optimization, indicating an increase in intensity as expected from a smaller focal spot. As found by counting (finding the amount of shots that contained a Ne^{2+} ion), the yield almost doubled; the counting showed Ne^{2+} ions in 17% of shots before this optimization and 30% after. Assuming an I^2 dependent process this corresponds to an increase in the intensity of around 33%, roughly corresponding to a focus that's $13 - 14\%$ smaller in each direction[5].

[5]The focus becoming smaller to the same degree in both directions assumes one is in the so-called "focus of least confusion", between the sagittal and tangential focii.

Chapter 6

Temporal aspects and pump-probe experiments

The study of dynamics in atoms and molecules requires ultrashort pulses and the ability to control these short pulses in time, such as in pump-probe experiments. Thus interferometry is needed, to characterize the temporal structure of the pulses as well as control their relative delay. The first work towards a RABBIT characterization of the attosecond pulses produced at the intense XUV beamline is presented in this chapter.

The target in question must also absorb two or more photons within the time frame of the dynamics studied. In the case of photoionization by two XUV photons, this requires an intensity which is rarely found at HHG sources, but is demonstrated at the intense XUV beamline.

6.1 Pump-probe experiments

Pump-probe experiments are one of the most common ways of performing time resolved studies in physics, chemistry and related disciplines. Pump-probe experiments have been performed on the femtosecond timescale since the early 1990s [115] and led to Ahmed Zewail receiving the Nobel Prize in chemistry in 1999 [4].

The main reason for performing pump-probe experiments is the fast nature of the phenomena one wishes to study; in order to have a good time resolution one must define the time scale. In a pump-probe experiment the way to define the time scale is to start the reaction with a *pump pulse* and measure it with a *probe pulse*. By varying the delay between the pump and the probe pulses, one records the observable (which can be anything, such as photon energies, the ion yield, or electron emission angles) at different points in the reaction and can thus build a time-resolved picture of how the reaction occurs.

A very simple example of this is shown in Figure 6.1. A pump pulse excites the target molecule. As

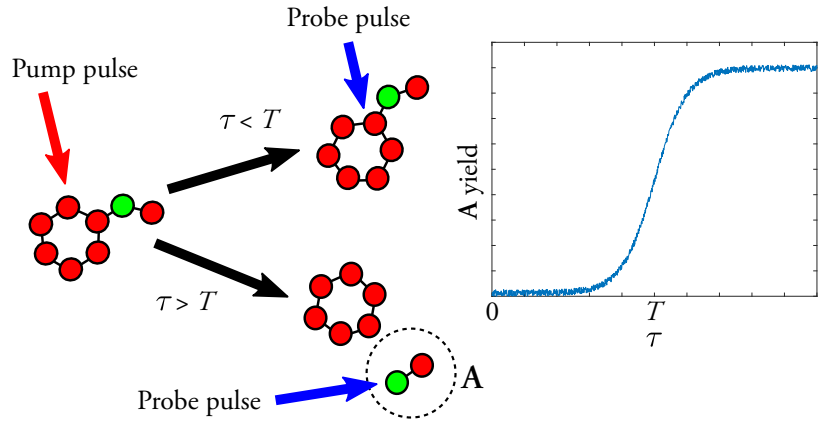

Figure 6.1: A simple pump-probe experiment: the yield of the fragment **A** measured as a function of the delay shows the time for fragmentation.

a result of this excitation, the molecule will fragment, leading to the emission of the fragment **A**. In order to measure the time this reaction takes, one may introduce a probe pulse with a variable delay τ. Only if the probe pulse arrives when the reaction has happened, the fragment will be ionized and collected by a particle detector[1]. The duration T for this process can thus be determined as the time where it is more likely than not that the fragment will be free and addressed by the probe pulse.

An important advantage in using light pulses is that since their velocity is well known (and extremely high), events at very small timescales can be controlled and measured by varying distances rather than times, which is one of the main points of interferometry. Many modern piezoelectric stages, for example, enable control of distances down to a few nanometers [51], which (depending on the geometry of the interferometer) can correspond to a few attoseconds in time.

6.2 XUV-IR experiments

6.2.1 RABBIT

The RABBIT technique has been used for nearly two decades, and was the first approach used to show the time structure of the attosecond pulse train [22]. It takes advantage of the fact that when an XUV pulse ionizes a target in the presence of a phase-locked IR field, the resulting photoelectron spectrum contains two-photon pathways known as sidebands.

A sideband can result either from the absorption of an XUV photon with energy $(2n-1)\omega$ and an IR photon (ω), thus reaching the energy of $(2n)\omega$, or the absorption of a $(2n+1)\omega$ XUV photon and emission of an IR photon. As an example, Figure 6.2 shows these energy levels for the first harmonics capable of ionizing neon ($I_p = 21.56$ eV).

[1] Section 3.5.3 shows a useful detector for experiments like this.

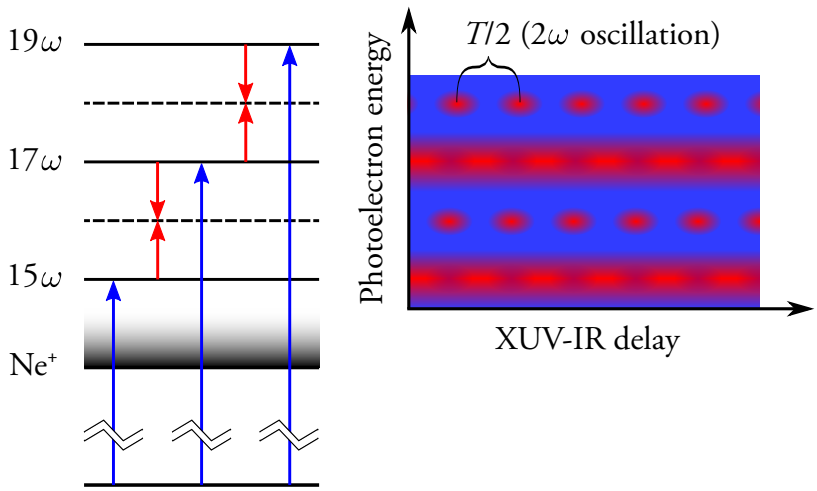

Figure 6.2: A schematic of the energy levels involved in a RABBIT experiment in neon. Layout adapted from [116].

Since the two pathways interfere with each other, varying the delay τ between the APT and the IR pulse thus leads to a modulation of the sideband q intensity as

$$I(\tau)_q = A_q + B_q \cos(2\omega\tau - \Delta\phi_q - \Delta\phi_q^{at}) \tag{6.1}$$

where A, B_q are delay independent amplitudes, $\Delta\phi_q$ is the phase difference between consecutive harmonics $\phi_{q+1} - \phi_{q-1}$, and $\Delta\phi_q^{at}$ is the "atomic phase", induced by XUV ionization and subsequent IR photon interaction.

With knowledge, or an assumption, of the phase structure of the ionization process, the technique can be used to reconstruct the time structure of the harmonic pulse train [22]. If instead the harmonic pulse train is well characterized, the technique can be employed to accurately determine the phase of electron wavepackets emitted from the atom, enabling high resolution temporal measurements of phenomena such as autoionizing resonances [117].

6.2.2 XUV-IR experiments at the intense XUV beamline

After the testing using IR beams showed promising results, the post-generation interferometer described in Section 3.3.2 was employed for XUV-IR pump-probe experiments. In order to overlap the XUV and IR foci, the XUV light had to be sent onto the actuated mirror of the SDU, and its alignment piezos used, since there was no actuated mirror in the IR arm. Section 3.5 gives an overview of the setup of this experiment after the interferometer chamber. Using the previously described focusing optics, the two beams were focused into a dense neon gas jet and the resulting photoelectrons were studied using the VMIS.

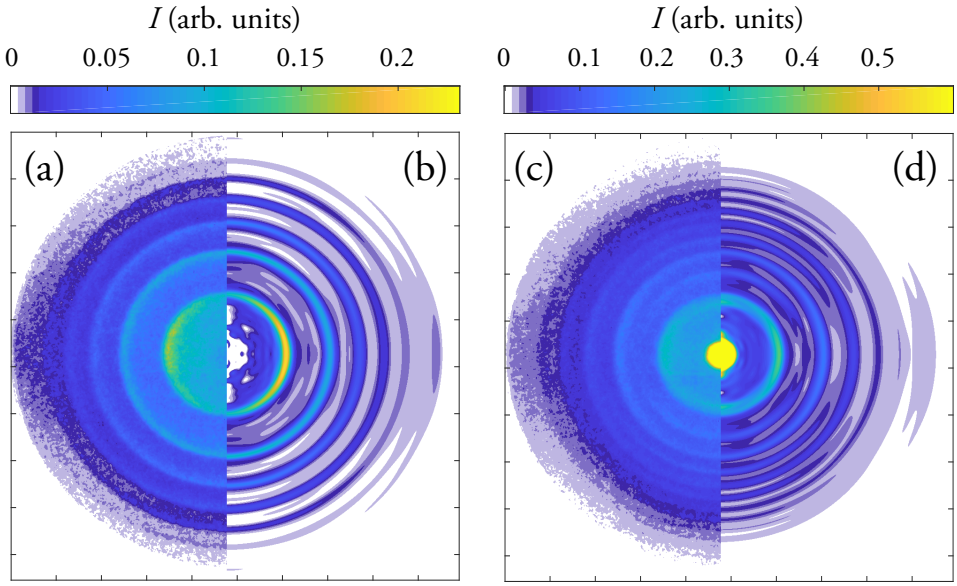

Figure 6.3: VMIS images of the photoelectron spectrum for (a,b) only XUV and (c,d) with IR also incident on the target. (a,c) show the "raw" image on the MCP phosphor screen, and (b,d) show the same image inverted using the pBASEX algorithm [66]. The color maps of these figures have been renormalized to emphasize the features of the spectrum.

Photoelectron VMIS images with and without IR, as well as before and after inversion (see Section 3.5.3 or Paper IV), can be seen in Figure 6.3. There could be some interesting delay-dependent angular features in (c, d) that may warrant some further study [118]. The figure also shows the effects of inversion, and how this enhances the spectral resolution of the image.

By angularly integrating these images, one can study the photoelectron spectrum, as demonstrated in Figure 6.4 for the spectra with and without IR light. As can be seen, the characteristic sidebands (noted in red) appear when the IR light is applied.

Figure 6.5 shows a first RABBIT scan. The same scan was carried out 4 times, with 100 acquisitions for each delay step (0.1 fs) in each scan. The reason for this is to minimize the influence of short- and long term fluctuations in the IR laser intensity and pointing.

There are already clear oscillations in the sidebands, as well as some weaker ones in the harmonics. The FFT of each individual sideband shows an oscillation frequency of 2ω, which is to be expected because of the $T/2$ periodicity of the APT as discussed in Section 2.2.3. This periodicity can also be seen in the inset, which shows the sideband oscillations over a delay of 3 fs, or slightly more than one IR laser cycle. Comparing consecutive sidebands, the nearly-linear phase shift indicative of the characteristic "attochirp" can also be seen as the dashed line through the sideband crests.

At the time of writing, the reconstruction of the APT by these phase measurements has not yet been performed, but it is the hope of the author that this can soon be done. In any case, the possibility of measuring the attochirp bodes well for reconstruction.

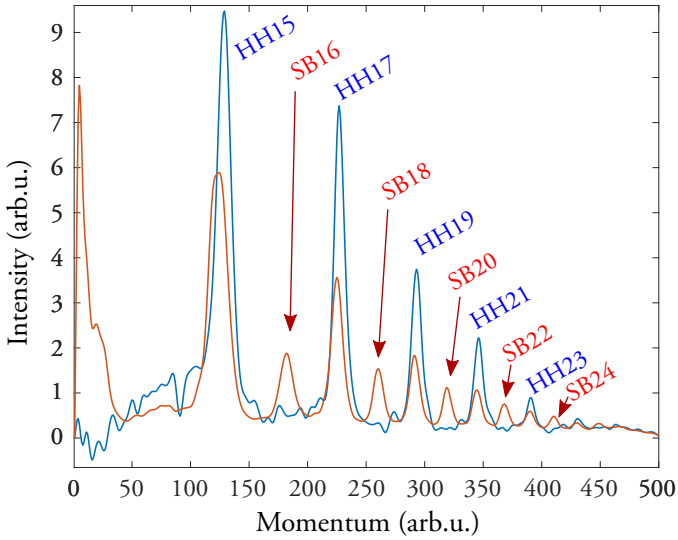

Figure 6.4: The inverted photoelectron momentum distribution shown without (blue) and with (red) incident IR light.

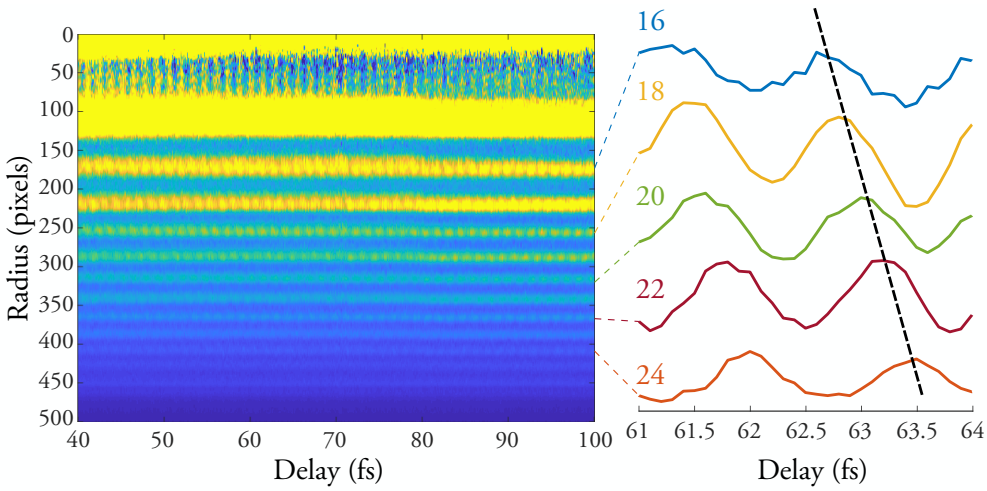

Figure 6.5: A RABBIT trace, acquired using the XUV-IR interferometer. The inset to the right shows the amplitude of the sidebands for approximately one cycle of the fundamental field, with the dashed line showing the approximate position of the maximum of each sideband.

6.3 XUV-XUV experiments

6.3.1 XUV multiphoton ionization

While light intensities enabling nonlinear light-matter interaction in the XUV and X-ray regimes have been accessible at Free-Electron Lasers (FELs) for more than a decade [119], it is a more elusive phenomenon for lab-scale laser systems [100, 120]. In Paper I, we demonstrate that the intense XUV beamline is among the few high-order harmonic beamlines capable of providing sufficient intensity for XUV multiphoton experiments by showing two-photon double ionization of neon.

To study this interaction, the high-order harmonic generation process was optimized to maximize the flux, and the harmonics were focused into the gas jet using the focusing optics detailed in Section 5.3.

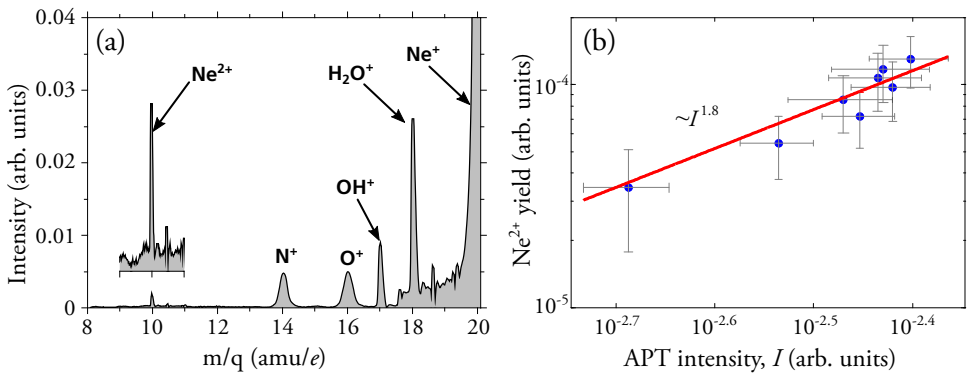

Figure 6.6: (a) Mass spectrum of ions and (b) the yield of Ne^{2+} plotted against the XUV intensity on a log-log scale. Adapted from Paper I.

Figure 6.6 (a) shows the time-of-flight mass spectrum. As can be seen, the most likely interaction by far is the single ionization of Ne. Other peaks that can be seen, identified as N^+, O^+, OH^+, and H_2O^+, were found to come from air and water pollution in the gas line.

At an m/q value of 10 we can observe a peak identified as the Ne^{2+} signal, which is expected to stem from two-photon double ionization. The Ne^{2+} yield is only 0.35% of that of Ne^+, which is in the order of magnitude to be expected when one compares the cross sections of one- and two-photon interactions at the intensity used ($3 \cdot 10^{12}$ W/cm^2). The energy required to doubly ionize Ne is 62.5 eV, and the fact that photons of this energy were not produced in the experiment is another indication of a multiphoton process.

Another way of identifying a two-photon signal is by its intensity dependence (as a second-order process it should be proportional to the square of the intensity). Thus, the XUV intensity was adjusted by tuning the pressure in the gas cell, and estimated by the (single-photon) H_2O^+ ion signal. Figure 6.6 (b) shows the Ne^{2+} yield plotted against intensity, on a doubly logarithmic scale. A linear regression shows a slope of 1.8, close to the slope of 2 which would imply a quadratic intensity dependence.

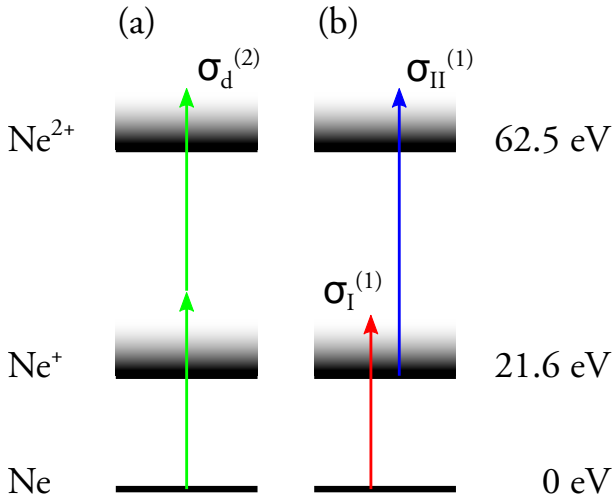

Figure 6.7: (a) The direct and (b) the sequential modes of two-photon double ionization in neon. The diffuse sections indicate the continua above the two ionization potentials.

Being able to measure a two-photon signal also led to the investigation of whether the two-photon double ionization took place through the direct or sequential processes, as illustrated in Figure 6.7. In the direct process, the two-photon double ionization takes place immediately through what can be seen as a virtual energy level. In the sequential process, one photon ionizes the Ne atom, and the next ionizes the Ne^+ ion further.

Using previously measured and calculated values [121–123] for the cross sections, it was calculated that the sequential process should be the dominant channel given the APT pulse duration (assumed to be 4.5 fs, from 15 pulses of 300 as each). In order to verify this, the harmonic spectrum was manipulated.

The total energy required to reach the Ne^{2+} state is 62.5 eV, which means that the direct process for double ionization only needs two photons with a total energy matching this value. In contrast, the sequential process always requires the second photon to have an energy of at least 40.9 eV (the ionization potential of Ne^+). Thus, if the harmonic spectrum could be eliminated above this energy value, whatever double ionization still occurred would be a result of the direct process.

The beamline was reconfigured to generate harmonics in krypton instead of argon, as they have a lower cutoff (see Section 2.2). An absorption cell of argon gas was used to ensure the same pulse energy as the previous measurement, in order to maintain the same intensity. The two spectra can be seen in Figure 6.8 (a), with the krypton spectrum in blue and the argon spectrum in red.

Figure 6.8 (b) shows the count rate in the TOF measurement for different m/q values, binned to improve the signal-to-noise ratio. The bin between 9.93 and 10.09 amu/e is then the Ne^{2+} peak. As can be seen, this peak is only present for the higher-order argon harmonics, supporting the hypothesis that the two-photon double ionization chiefly occurs through the sequential process.

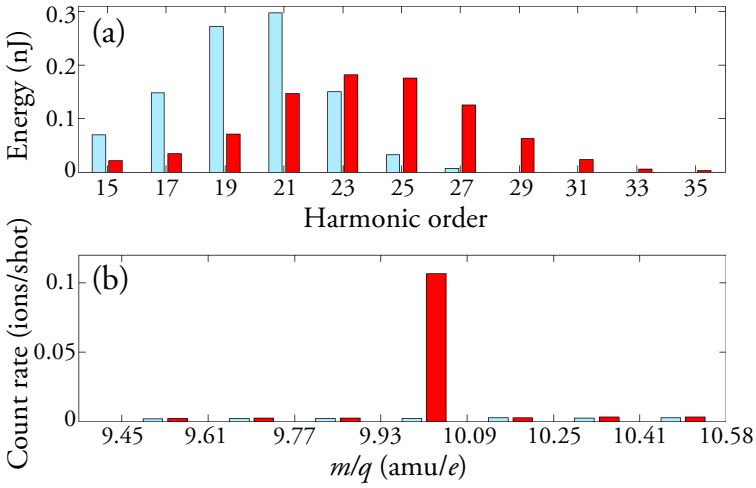

Figure 6.8: (a) Spectrum and (b) Ne^{2+} yield for harmonics generated in argon (red) and krypton (blue). Adapted from Paper I.

6.3.2 XUV autocorrelation

Some attempts have been made at using the SDU described in Section 3.3.1 for XUV autocorrelation experiments, in order to determine the time structure of the APT. No conclusive results have emerged so far.

One potential explanation for the difficulty in measuring the autocorrelation is that pointing instabilities lead to the XUV beam position on the "split" between the two mirrors in the SDU varies, resulting in varying energy proportions in the two arms and reducing the contrast. Another is that possibly the chromatic aberration and spatiotemporal coupling discussed in Paper V reduces the pulse bandwidth at each point in the focus, changing the time structure. Finally, the statistics involved (for Ne^{2+}, for example, an ion might appear in 25% of the shots, or even less, as seen in Figure 6.8 (b)) mean that a large number of shots is required, which makes the measurement more sensitive to long-term fluctuations in laser energy and pointing.

Summary and outlook

In this chapter, the most important results of the thesis work and the resulting Papers are summarized, followed by prospects for ongoing and future work.

Summary

The presented thesis work has partly been an attempt to study XUV light generated through the high-order harmonic generation process, spatially, by flat field spectrometers and Hartmann mask wavefront sensors, and temporally, mainly by cross-correlation with IR pulses. Some investigations have also been performed towards using the high-order harmonics to probe atomic and molecular dynamics and for temporally resolved measurements.

An intense attosecond light source

The intense XUV beamline described in Chapter 3 has proven capable of producing XUV light with high pulse energies, as detailed in Section 6.3.1. In combination with the focusing optics used, the beamline offers XUV intensities matched by only a few other lab-sized sources. Papers I and IV describe experiments using these energetic XUV pulses; Paper I in particular demonstrates two-photon double ionization, which requires very high intensities, above 10^{12} W/cm^2, in the XUV. This has enabled studies of ionization dynamics previously inaccessible for most table-top light sources.

Paper IV reports on a measurement instrument for simultaneous characterization of photoelectrons and positive ions, created by photoionization; the covariance technique described allows ions, electrons and fragments of molecules to be correlated to each other despite the large event rates resulting from such an intense light source.

Pump-probe experiments

In order to exploit the short and intense pulses, as well as electron and ion spectrometry techniques, provided by the intense XUV beamline, a very interesting avenue is to use them for time-resolved

experiments.

To this end, an interferometer has been constructed, as described in Section 3.3.2. This XUV-IR interferometer has been tested in terms of accuracy and repeatability by ATI using two IR beams, and employed for RABBIT scans overlapping XUV and IR beams. While some challenges have been identified, the experiments were largely successful and it seems that the interferometer will be a useful instrument. Its design resembles that proposed for the ELI-ALPS "long" gas beamline described in Paper II and Section 3.7, and successful testing at the intense XUV beamline indicates that design's viability.

To extend the range of the proposed experiments, another interferometer design has also been proposed, enabling long-range pump-probe experiments with an additional IR pulse.

Spatial properties of high-order harmonics

Paper VI describes an in-depth study on the origins of the XUV wavefront aberrations. The wavefronts are collected as single shots, minimizing the influence of pointing fluctuations on the measurements. The experiments show that many factors used to control the phase matching and subsequent harmonic yield also have a negative impact on the quality of the beam, leading to a certain trade-off between APT energy and focus size when the highest intensity is desired.

Another factor for the spatial properties of the harmonics, as discussed in Paper V, is that individual harmonic orders of the attosecond pulse train may have different divergences and source positions due to the curvature induced by the dipole phase, introduced by the HHG process. This may lead to chromatic aberrations, where the focal region has a rapidly varying spectral content. Because of the time-frequency coupling, this also leads to spatiotemporal couplings, in which the time structure of the pulse varies along the focal region. The theoretical model for the curvature added by the dipole phase proposed in Paper V is also supported by experiments measuring the order-dependent divergence of the harmonics.

The quality of the beam dictates the size of the focus, and the size of the focus determines the intensity available for experiments. Paper III presents a study of the focusing parameters of the toroidal mirror setup used at the intense XUV beamline, and how they can be optimized to minimize the aberrations of the XUV wavefront, enhancing the focus and thus the intensity. After optimization of the wavefront, the focus could be calculated to be 3.6×4.0 μm^2, close to the ideal spot size of 3.0×3.2 μm^2. Minimizing the focal spot size is shown to enable the intensities necessary for multiphoton experiments.

Outlook

Frequency-resolved wavefront sensing

The EUV Generation & Imaging group at the Advanced Research Center for Nanolithography (ARCNL) has developed a novel approach to wavefront sensing which provides a 2D wavefront

measurement as well as spectral resolution. It is in essence a Hartmann mask in which every hole is also a transmission grating [84].

Some experiments using this grating Hartmann mask were performed at the intense XUV beamline. For the experiments in question, the mask was mounted in the sample holder of the CDI chamber mentioned in Section 3.6.

This instrument was used to study, among other things, the focus-dependent harmonic properties that were expected as a result of the dipole phase contributions, with analysis still ongoing.

The spatiotemporal impact of the dipole phase

The harmonic-dependent spatial influence of the dipole phase, as described in Section 2.2.5 and paper V, is clearly important to study, since it carries so many implications as to the feasibility and reproducibility of ultrafast experiments with broadband pulses. However, it is also intriguing in an experimental sense; there are many observables, parameters to control, and (sometimes conflicting) theoretical interpretations.

In paper V, we try to verify the changes in harmonic divergence in one dimension, necessitated by the fact that we need the other for our spectral resolution. With the aforementioned frequency-resolved wavefront sensing, other observables such as the radii of curvature (giving us a measure of the focus position) can be studied in two dimensions (thus taking into account, for example, astigmatism, unlike frequency resolved but spatially one-dimensional measurements, as discussed in Section 4.3).

With the help of fully frequency-resolved wavefront sensing I'm hopeful that more characteristics of the harmonics can be studied, enabling the testing of even higher-level theory.

Multiple-beam pump-probe experiments

The post-generation interferometer has now been shown to be capable of IR-IR and IR-XUV pump-probe experiments. This in itself opens up a wide range of interesting experiments, but this could be widened further by introducing more beams.

There are two immediate "next steps", interesting avenues of progress, both of which are quite well prepared already. The first is XUV-XUV experiments with the addition of an extra IR pulse to use, for example, as an excitation pulse. As the SDU is already installed in the interferometer chamber, this would require only minor rebuilding of the optical setup.

The second thing that would be interesting to try is molecular alignment using the pre-generation interferometer. It has already been built and a rough temporal overlap has been found, so the main challenge would be to insert it into the beam path in a minimally disruptive way and find a suitable target for testing. This would require a slight rebuild of the post-generation interferometer, for example installing an actuated rotation stage for the $\lambda/2$ plate in order to regulate the ratio of energy in the alignment beam and IR pump/probe beam in a controlled manner.

Studying complex molecules with the DVMIS

This thesis has mainly dealt with the development and characterization of instruments and sources for experiments in atomic and molecular dynamics, but not so much with the experiments themselves. However, some work has also been done towards these kinds of experiments.

An important reason for the development of the double-sided VMIS was the aim to study fragmentation of large molecules. The investigation of fragment yields in a time-resolved fashion is a good way to study fast events in molecules such as charge transfer and ionization dynamics [124, 125].

The molecular source, as described previously, does not limit us much when it comes to the target of choice. Our research group has already made some progress in the study of more complex molecules, and some investigations of hydrocarbons and even small amino acids have already been performed.

Perhaps the most promising of the molecular experiments so far is a fragmentation dynamics study of adamantane ($C_{10}H_{16}$) , the smallest diamondoid [126]. Figure 3 shows some preliminary results of the experiments on adamantane; the mass spectrum measured using the TOF is plotted, displaying the fragments resulting from single or double ionization of the molecule. Above every fragment, VMIS images are shown; these are derived from the pixel-by-pixel covariance with the given peak in the mass spectrum. Consequently, they show the momentum distribution of each given fragment, without the need for separate VMIS measurements.

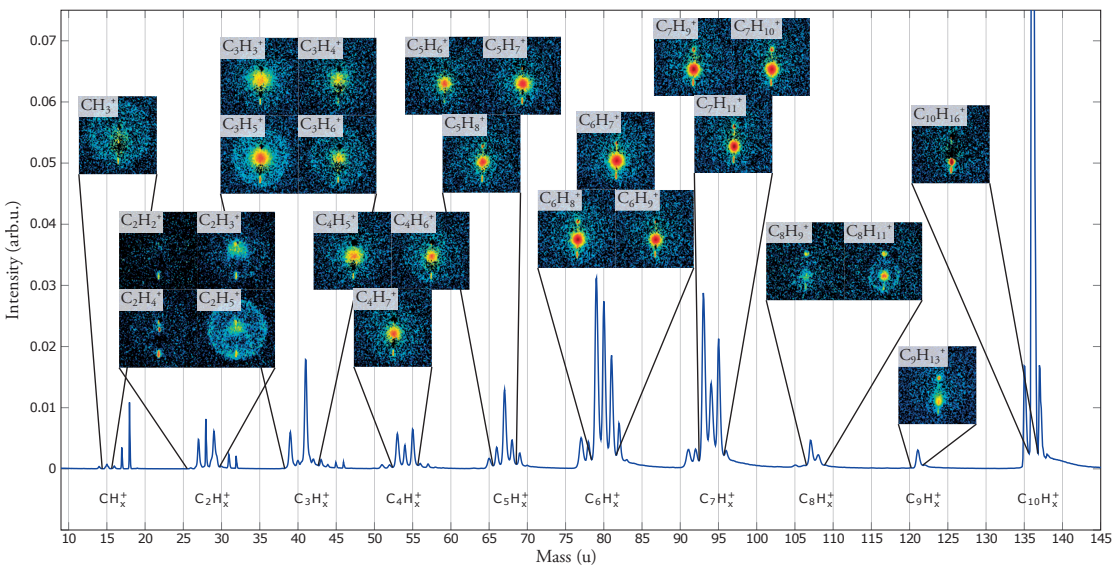

Figure 3: The mass spectrum of fragments of adamantane, and the correlated VMIS images of each fragment. Figure adapted from [127].

The analysis of these results is still ongoing, but some theoretical work on the fragmentation dynamics has already been done. With the capabilities we now have for pump-probe experiments it would be very interesting to repeat these studies, in order to learn more about the dynamics of the system [128].

Coherent diffractive imaging

CDI is a technique for imaging microscopic samples using X-rays [129, 130]. While the method has been performed for quite some time using FELs and synchrotron facilities, the use of HHG sources to perform these experiments was only quite recently demonstrated [131].

Some experiments on CDI were performed at the intense XUV beamline. Their main objective was to test the viability of using a polychromatic source such as the XUV light of the intense XUV beamline for this technique [132]. Using a priori knowledge of the harmonic spectrum (which can be measured using the XUV spectrometer, or by double slit diffraction in the CDI setup), the diffraction pattern for each harmonic can be calculated, after which the image can be reconstructed. An example of this reconstruction can be seen in Figure 4.

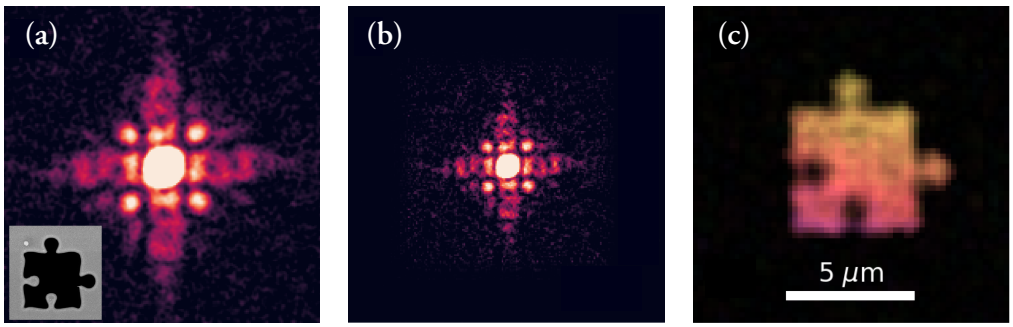

Figure 4: (a) The CDI pattern of a puzzle piece aperture, shown in the inset; (b) The calculated diffraction pattern of only one harmonic; (c) The reconstructed image of the puzzle piece. Figure adapted from [132].

Being able to make use of polychromatic light somewhat offsets the "downside" of HHG sources producing very broadband spectra. Enabling imaging techniques such as CDI on table-top XUV sources could in turn make this technique more widely available to scientists compared to performing it at large-scale facilities.

Generation optimization algorithm

A piece of software using a genetic algorithm [133] was developed as part of this thesis work, with the initial goal of simplifying the optimization of harmonic generation by manipulating the IR wavefront using the DM. Because the drivers for the DM were initially not available, the first parameters to be optimized were instead the pulse energy, pulse duration, iris opening, and timing (delay and pulse length) of the pulsed valve for the generation gas[2].

The algorithm, as shown in a simplified manner in Figure 5, works by starting with 10 row vectors of initially random elements that each represent one of the generation parameters. For each of these vectors, or "individuals", the generation parameters specified in its "genes" are applied to the beamline and the XUV pulse energy (measured as the integrated signal on the Andor CCD

[2]The components of the HHG setup are described in detail in Chapter 3.

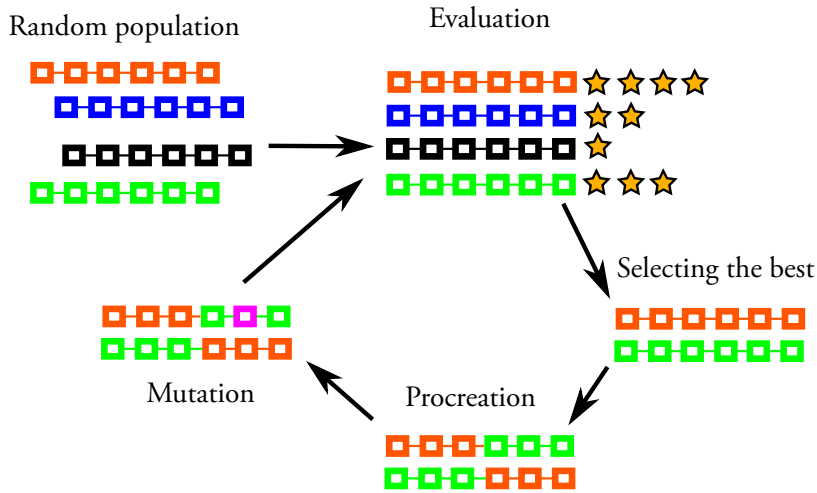

Figure 5: The scheme of a simple genetic algorithm.

camera) constitutes the "score". The three highest scoring individuals procreate, i.e. their "genes" are swapped at an arbitrary crossover point, leading to six new individuals. Finally, four new random individuals are added to the population, and in some cases a "mutation" is added to one of the existing individuals. This is to avoid being stuck in a local scoring maximum.

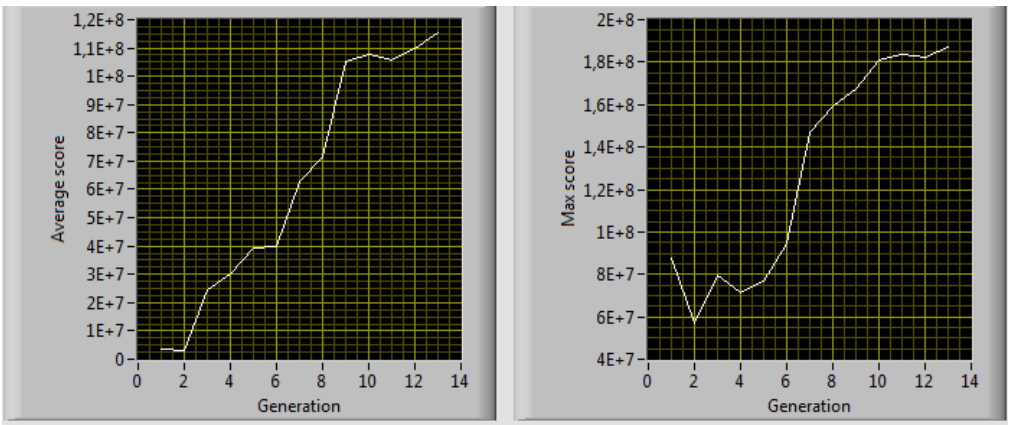

Figure 6: The results of testing the genetic algorithm for HHG optimization, showing the average (left) and maximum (right) scores of the populations.

The results of testing this algorithm can be seen in Figure 6. As can be seen, there is initially a period (the first $5-6$ generations) where the maximum score does not improve much. What happens here is that the average score increases as the genes of the most, but still not very, successful individuals propagate through the population. At generation 7 an individual with a much higher score appears. As can be seen then, the quick growth in maximum score is followed by an increase in average score as, again, the successful traits are distributed among the population.

The end result of optimization was a set of parameters very close to that found by manually optimizing the generation conditions, and it took only slightly longer; each generation took around 50 seconds to evaluate, meaning that the 13 generations took less than 11 minutes in total. In comparison, the conditions are typically found in around 5 minutes by experienced operators of the beamline. However, it should be noted that this example involved only 5 parameters; a manual search gets increasingly complex with more dimensions of the solution space.

While these results were promising, it would be very interesting to attempt to apply this technique to the DM, to do something similar in the spatial domain what has previously been done in the Fourier domain for ultrafast IR pulses [134] and for HHG [135]. As the DM has 32 different parameters, finding an optimum manually is not deemed realistic, thus pointing at the potential of an algorithm to solve this problem.

The long-term goal, however, would be to make the algorithm method- and scoring-agnostic, meaning that it could be applied to any input and output parameters. Some obvious examples are the various generation parameters, or even individual Zernike polynomials of the IR wavefront, as the output and factors such as total harmonic yield, XUV wavefront error, or a direct measure of intensity (such as the ion yield of a multiphoton process) as the input, or "score".

In addition to increasing the domain of parameters that can be optimized, another interesting avenue of inquiry would be to try alternative algorithms and heuristics. The genetic algorithm is very easy to implement and is quite good at eventually finding an optimum solution for a multidimensional parameter space, but requires a relatively large number of evaluations. In the case of a physical process such as HHG that must be evaluated, and in contrast to many computational problems in which evaluation is more or less trivial, the evaluation function is referred to as *expensive* in the terms of machine learning literature. Some heuristics indicated to be more suitable for an expensive evaluation function (i.e. that require fewer evaluations) include Bayesian optimization [136] and Lipschitz constant optimization [137].

In conclusion, work on algorithmic optimization can hopefully lead to a more efficient HHG process, meaning that the scope of available experiments widens for the beamline as more or higher-energy photons are produced.

Comments on papers

Paper I: Two-photon double ionization of neon using an intense attosecond pulse train

This paper demonstrates the power of the intense XUV beamline by studying the two-photon double ionization of neon. Rate equations predict that for the parameters described in the paper, the sequential channel dominates the ionization process over the direct. This is supported by studying the response of the system to a spectral shift in the XUV light.

I took part in the experiment, participated in the discussions, chiefly on those regarding the two ionization channels, and gave feedback on the manuscript.

Paper II: The ELI-ALPS facility: The next generation of attosecond sources

This paper shows the designs of all the beamlines of the future ELI-ALPS facility, currently under construction in Szeged, Hungary. This facility will contribute to laser system development as well as work as a user facility. One of the beamlines, the "long" gas HHG beamline using the SYLOS laser, was designed in Lund, and is based on the theory of scale-invariant harmonic generation that has also influenced the high-intensity XUV beamline in Lund.

I contributed to the design of an XUV-IR interferometer for use in the "long" beamline described in section 3.4 of the paper. The design is similar to that constructed for the beamline in Lund but takes into account the increased scale of the ELI-ALPS beamline. I also gave feedback on the Lund section of the manuscript.

Paper III: Micro-focusing of broadband high-order harmonic radiation by a double toroidal mirror

This paper concerns aberrations of the XUV wavefront, their effect on the XUV focal spot, and how they can be minimized using toroidal mirrors in a Wolter configuration. It is demonstrated that by orienting the configuration of the presented mirrors, one can not only minimize the aberrations introduced by the mirrors, but even use them to reduce the aberrations already present in the XUV

wavefront. The focus is studied indirectly (by back propagation of the wavefront) and directly (with a scintillator crystal) and is shown to be close to the theoretical limit, estimated by the use of raytracing software.

I took part in the experiments, mainly the generation of the harmonics used to test the optics, and gave feedback on the manuscript.

Paper IV: A versatile velocity map ion-electron covariance imaging spectrometer for high intensity XUV experiments

This paper presents a design for a useful ion/electron spectrometer, which enables simultaneous measurements on ions and electrons, either measuring the ion momenta using the VMI technique or getting highly accurate mass spectra using time-of-flight. The covariance technique is also tested and proven to be a good way of coping with the high event rate / low rep rate of our beamline.

I took part in the installation and testing of the DVMIS and its chamber, gave feedback on the manuscript, and took part in discussions on revisions.

Paper V: Spatiotemporal coupling of attosecond pulses

This paper describes the use of Gaussian optics to estimate the spatial consequences of a new formulation of the atomic dipole phase. The calculations lead to the conclusion that harmonic orders may vary strongly in terms of divergence and focus position, leading to chromatic aberration and subsequent spatiotemporal coupling when the harmonics are focused, which is often the case for applications. Thus these effects may need to be taken into account for many experiments.

I planned the experiments and performed them along with the intense XUV group, analyzed the experimental data, plotted most of the analytical calculations in the paper, and wrote large parts of the manuscript.

Paper VI: Single-shot extreme-ultraviolet wavefront measurements of high-order harmonics

This paper deals with wavefront measurements and calculations of the generated harmonics, and the dependence of the wavefronts on the generation parameters used. In some cases, the conditions leading to optimum harmonic yields will not give rise to the highest quality wavefronts of the generated XUV light. This means that a trade-off between pulse energy and focusability needs to be taken into account when intense harmonics are required.

I took part in the experiments and discussions on the manuscript and gave feedback on the manuscript.

Acknowledgements

Om du har en god vän, ta vara på den!
- General Knas

While I would like to believe that finishing a thesis is, at least partly, thanks to grit and conviction, the truth is that there are many people without whom I could never have done this.

First of all I want to thank my main supervisor, Per Johnsson. For the whole time I've been here, time and time again you have shown how committed you are to the success and wellbeing of your group and its members. When times are hard, you are always there for a pep talk, and when times are good, you are quick to celebrate but also remind us of the hard work it took to get there. Thanks for believing in me when you didn't (yet?) have a reason to do so, and for setting a good example of work-life balance.

I would also like to thank my co-supervisor, Anne L'Huillier. Heading a group as big and diverse as the atto-group, you would be excused for not knowing the details of everything going on, but you somehow do, and always have questions and suggestions. Thanks for inviting me to participate in the "harmfoc" project, it means a lot since it's obvious how much you care about it.

Moving on, none of the work in this thesis could have been done without the 10 Hz (I mean Intense Attosecond... no, wait, I mean Intense XUV beamline... Intense XUV Attosecond?) group.

Out of the "old guard", I'd like to thank Bastian Manschwetus for welcoming me to the beamline and Christoph Heyl for explaining so many things. Thanks to Piotr Rudawski for believing in my design and teaching me about tolerances. Thanks to Filippo Campi for "making optics great again", and to Linnea Rading for designing the awesome DVMIS (and taking us to Edison).

I want to thank Sylvain Maclot for all the blast beats we enjoyed in and outside the lab, and for introducing me to the scientific lifestyle. Thanks to Hélène Coudert-Alteirac for the hard Labview work (sitter vi i samma båt?) and to Jan Lahl for the card games we shared (... ...resolves). Finally, thanks to Jasper Peschel for the night shifts (and relaxing hangouts after night shifts!) and to Hugo Dacasa Pereira for the wavefront wisdom.

I'd also like to thank all of the people who have worked on the beamline: the three Balázs (Farkas, Major and Nagyilles), with some special thanks to BM for all the help in commissioning and testing the IR-XUV interferometer, Fabian Brunner, Emma Kueny, Marius Plach, Hanna Berg, Erik Malm, Viktoria Nefedova and Tarek Mohammed, thanks for everything you've done for us and for the cool things we got an opportunity to try.

Big thanks also go to our other collaborators outside the intense XUV group, including Cord Arnold, Jan Vogelsang, Chen Guo and Stefanos Carlström in the "LASC group", Mathieu Gisselbrecht and Bart Oostenrijk from the synchrotron radiation division; Peter Smorenburg at ASML; Patrick Rousseau at UNICAEN; Stefan Witte, Matthijs Jansen and Kevin Liu at ARCNL; and Philippe Zeitoun at LOA.

Since very little could have been done without the "10 Hz" laser, very little could have been done without Anders Persson, without whom the laser stops being the best laser in the world and becomes simply **among** the best. Speaking of indispensable people, all the work at the atomic physics division would be much harder, if at all possible, without the hard work of Anne Petterson-Jungbeck, Åke Johansson, Jakob Testad (Hardcore will never die!) and Claes-Göran Wahlström, for which I want to thank them profusely. I would also like to thank Håkan Ivansson for always being ready and helpful in the workshop (and not once commenting on the quality of my sketches).

Thanks to everyone in the atto group for being an inspiring and helpful group of peers and friends, and for the scientific talks, get-togethers, conferences, summer schools and parties we have shared. First of all, thanks to Neven and Lana (the *hermanos*); Neven for the "enemy dances" and song meetings, and Lana for your no-BS attitude (except towards our national dish).

I also want to thank David B for the discussions, RABBIT and otherwise, Samuel for being the best Santa in the division, Emma S for the "excellent stuff", and Yu-Chen for your optimism and curiosity (I was going to say your singing, but Jan stole it). Thanks to Miguel for the alignment wizardry, Maïté for being an inspirational daredevil, and Anne H for always seeing the best in people.

There are many other current and former members that I also want to thank for brightening my day at the atomic physics division one way or another; thanks a lot to Esben, Simon, Johan, Saikat, Anna, Ello, Sara, Lisa, Shekhar, Marija, David K, Alexandre, Fabian L, Laura, Chuang, Hugo L, Maria, Marcus, and Shiyang.

The atomic physics division in general has provided a great place to work and a wonderful atmosphere, for which I want to thank, among others, the members of the high intensity group (also thanks for all the laser work you did), the quantum information group, the X-ray physics group, and the medical optics group. Thanks also to Lars Engström for all the work you've done for the teaching in the division (and for teaching me atomic physics in the first place!).

On a more personal note, I (along with the thesis, I presume) benefitted greatly from good opportunities to relax outside of work and for that I would like to thank Oskar, Emma, Karolina, Giorgi, Jonas, Axel, Adrian and the rest of my Lund and Malmö friends, and of course Miklos, Alexander, Christian, Olof and many others in the Uppsala contingent (see you at Palermo!), as well as those in other places I don't see as often but miss nonetheless.

Even outside the lab I couldn't avoid the lasers - many experiments were performed at various other locations with a wonderful group of friends and collaborators in the "Hard Crew", Tarantism, Øka and Seizure, and I want to thank everyone involved. I would also like to thank my friends at Rydbergs Minne, Sydskånska Nationen and Radio AF for letting me keep a semblance of student life while working.

During the writing process I made great use of the Overleaf service, for which I am and will remain grateful. Gott och Nära provided much needed "food for thought" during the later stages of thesis writing, and Freshers supplied some of the critical writing caffeine. Those mentioned have not sponsored me, although they are most welcome to do so.

My parents are due a large debt of gratitude for supporting me, pushing me, and always being (or seeming) convinced I'd end up a scientist, even when I wasn't. Thanks to Jacob for the near-daily discussions, regardless of relevance. Thanks also to our "new families" Anna, Ebba and Axel as well as Alf, Kerstin, Erik and Karin, for coming into our lives and letting us into yours. Speaking of family, Björn and Catrine are probably at least partly responsible for the way the thesis looks, and Mats and Per for the subject matter. Thanks to everyone else in my extended family and to all four generations of the Johansson-Kreuger clan.

Finally, I can't thank my soon-to-be wife Linnea enough for all the love and support through the years. May we finally get to spend more time together, and may our adventures never end!

Figure 7: Image taken from *"A user end station at the intense XUV beamline"* by J. Peschel and H. Wikmark (manuscript in preparation).

Bibliography

[1] W. E. Bradley, "The surface-barrier transistor: Part I - principles of the surface-barrier transistor", *Proceedings of the IRE*, vol. 41, no. 12, pp. 1702–1706, 1953.

[2] N. F. Ramsey, *Nuclear Moments*. John Wiley & Sons, 1953.

[3] L. Essen and J. V. L. Parry, "An atomic standard of frequency and time interval: A cæsium resonator", *Nature*, vol. 176, pp. 280–282, 1955.

[4] A. Zewail, "Femtochemistry: Atomic-Scale Dynamics of the Chemical Bond", *Journal of Physical Chemistry A*, vol. 104, pp. 5660–5694, 2000.

[5] "LabMaster 10 Zi-A datasheet." Teledyne LeCroy website, retrieved from `https://teledynelecroy.com/doc/docview.aspx?id=8636` on 2019-02-03.

[6] M. Göppert-Mayer, "Über Elementarakte mit zwei Quantensprüngen", *Annalen der Physik*, vol. 401, no. 3, pp. 273–294, 1931.

[7] T. H. Maiman, "Stimulated optical radiation in Ruby", *Nature*, vol. **187**, pp. 493–494, 1960.

[8] W. Kaiser and C. G. B. Garrett, "Two-photon excitation in CaF_2:Eu^{2+}", *Physical Review Letters*, vol. 7, no. 6, pp. 229–231, 1961.

[9] A. McPherson, G. Gibson, H. Jara, U. Johann, T. S. Luk, I. A. McIntyre, K. Boyer, and C. K. Rhodes, "Studies of multiphoton production of vacuum-ultraviolet radiation in the rare gases", *Journal of the Optical Society of America B*, vol. 4, pp. 595–601, 1987.

[10] M. Ferray, A. L'Huillier, X. Li, L. Lompre, G. Mainfray, and C. Manus, "Multiple-harmonic conversion of 1064 nm radiation in rare gases", *Journal of Physics B: Atomic, Molecular and Optical Physics*, vol. 21, pp. L31–L35, 1988.

[11] K. C. Kulander, K. J. Schafer, and J. L. Krause, "Dynamics of short-pulse excitation, ionization and harmonic conversion", in *Super-Intense Laser-Atom Physics*, Plenum Press, New York, 1993.

[12] M. Lewenstein, P. Balcou, M. Y. Ivanov, A. L'Huillier, and P. B. Corkum, "Theory of high-order harmonic generation by low-frequency laser fields", *Physical Review A*, vol. 49, pp. 2117–2132, 1994.

[13] P. Salières, A. L'Huillier, P. Antoine, and M. Lewenstein, "Study of the spatial and temporal coherence of high-order harmonics", *Advances in Atomic, Molecular and Optical Physics*, vol. 41, pp. 83–142, 1999.

[14] C. M. Heyl, C. L. Arnold, A. Couairon, and A. L'Huillier, "Introduction to macroscopic power scaling principles for high-order harmonic generation", *Journal of Physics B: Atomic, Molecular and Optical Physics*, vol. 50, no. 1, 013001, 2017.

[15] C. M. Heyl, P. Rudawski, F. Brizuela, P. Johnsson, C. L. Arnold, and A. L'Huillier, "Conceptual design report for a gas HHG beamline at ELI-ALPS", 2012.

[16] F. Krausz and M. Ivanov, "Attosecond physics", *Reviews of Modern Physics*, vol. 81, no. 1, pp. 163–234, 2009.

[17] H. R. Telle, G. Steinmeyer, A. Dunlop, J. Stenger, D. Sutter, and U. Keller, "Carrier-envelope offset phase control: A novel concept for absolute optical frequency measurement and ultrashort pulse generation", *Applied Physics B*, vol. 69, no. 4, pp. 327–332, 1999.

[18] F. Arecchi and R. Bonifacio, "Theory of optical maser amplifiers", *IEEE Journal of Quantum Electronics*, vol. 1, no. 4, pp. 169–178, 1965.

[19] P.-A. Belanger and C. Pare, "Self-focusing of Gaussian beams: an alternate derivation", *Applied Optics*, vol. 22, no. 9, pp. 1293–1293, 1983.

[20] D. Strickland and G. Mourou, "Compression of amplified chirped optical pulses", *Optics Communications*, vol. 56, no. 3, pp. 219–221, 1985.

[21] G. Farkas and C. Tóth, "Proposal for attosecond light pulse generation using laser induced multiple-harmonic conversion processes in rare gases", *Physics Letters A*, vol. 168, no. 5-6, pp. 447–450, 1992.

[22] P. M. Paul, E. S. Toma, P. Breger, G. Mullot, F. Augé, P. Balcou, H. G. Muller, and P. Agostini, "Observation of a train of attosecond pulses from high harmonic generation", *Science*, vol. 292, no. 5522, pp. 1689–1692, 2001.

[23] L. V. Keldysh, "Ionization in the Field of a Strong Electromagnetic Wave", *Soviet Physics, Journal of Experimental and Theoretical Physics*, vol. 20, pp. 1307–1314, 1965.

[24] R. Haight and P. F. Seidler, "High resolution atomic core level spectroscopy with laser harmonics", *Applied Physics Letters*, vol. 65, no. 5, pp. 517–519, 1994.

[25] E. J. Takahashi, T. Kanai, K. L. Ishikawa, Y. Nabekawa, and K. Midorikawa, "Coherent water window X ray by phase-matched high-order harmonic generation in neutral media", *Physical Review Letters*, vol. 101, no. 25, 253901, 2008.

[26] M. Ammosov, N. Delone, and V. Krainov, "Tunnelling ionization of complex atoms and of atomic ions in an alternating electromagnetic field", *Soviet Physics, Journal of Experimental and Theoretical Physics*, vol. 64, no. 6, pp. 1191–1194, 1986.

[27] P. Corkum, "Plasma perspective on strong-field multiphoton ionization", *Physical Review Letters*, vol. 71, no. 13, pp. 1994–1997, 1993.

[28] S. Ghimire, A. D. DiChiara, E. Sistrunk, P. Agostini, L. F. DiMauro, and D. A. Reis, "Observation of high-order harmonic generation in a bulk crystal", *Nature Physics*, vol. 7, no. 2, pp. 138–141, 2010.

[29] B. Dromey, M. Zepf, A. Gopal, K. Lancaster, M. Wei, K. Krushelnick, M. Tatarakis, N. Vakakis, S. Moustaizis, R. Kodama, *et al.*, "High harmonic generation in the relativistic limit", *Nature Physics*, vol. 2, no. 7, pp. 456–459, 2006.

[30] H. Liu, Y. Li, Y. S. You, S. Ghimire, T. F. Heinz, and D. A. Reis, "High-harmonic generation from an atomically thin semiconductor", *Nature Physics*, vol. 13, no. 3, pp. 262–265, 2016.

[31] M. B. Gaarde, A. L'Huillier, and M. Lewenstein, "Theory of high-order sum and difference frequency mixing in a strong bichromatic laser field", *Physical Review A*, vol. 54, no. 5, pp. 4236–4248, 1996.

[32] Y. Mairesse, A. de Bohan, L. J. Frasinski, H. Merdji, L. C. Dinu, P. Monchicourt, P. Breger, M. Kovačev, R. Taïeb, B. Carré, H. G. Muller, P. Agostini, and P. Salières, "Attosecond synchronization of high-harmonic soft X-rays", *Science*, vol. 302, no. 5650, pp. 1540–1543, 2003.

[33] C. Guo, A. Harth, S. Carlström, Y.-C. Cheng, S. Mikaelsson, E. Mårsell, C. Heyl, M. Miranda, M. Gisselbrecht, M. B. Gaarde, K. J. Schafer, A. Mikkelsen, J. Mauritsson, C. L. Arnold, and A. L'Huillier, "Phase control of attosecond pulses in a train", *Journal of Physics B: Atomic, Molecular and Optical Physics*, vol. 51, no. 3, 034006, 2018.

[34] C. Guo, *A High Repetition Rate Attosecond Light Source Based on Optical Parametric Amplification*. PhD thesis, Faculty of Engineering, LTH, 2018.

[35] B. E. A. Saleh and M. C. Teich, *Fundamentals of Photonics*. John Wiley & Sons, 2007.

[36] C. M. Heyl, H. Coudert-Alteirac, M. Miranda, M. Louisy, K. Kovacs, V. Tosa, E. Balogh, K. Varjú, A. L'Huillier, A. Couairon, and C. L. Arnold, "Scale-invariant nonlinear optics in gases", *Optica*, vol. 3, no. 1, pp. 75–81, 2016.

[37] S. Svanberg, J. Larsson, A. Persson, and C.-G. Wahlström, "Lund High-Power Laser Facility – Systems and First Results", *Physica Scripta*, vol. 49, no. 2, pp. 187–197, 1994.

[38] C. G. Wahlström, J. Larsson, A. Persson, T. Starczewski, S. Svanberg, P. Salières, P. Balcou, and A. L'Huillier, "High-order harmonic generation in rare gases with an intense short-pulse laser", *Physical Review A*, vol. 48, pp. 4709–4720, 1993.

[39] M. Dalui, A. Permogorov, H. Pahl, A. Persson, and C.-G. Wahlström, "Influence of micromachined targets on laser accelerated proton beam profiles", *Plasma Physics and Controlled Fusion*, vol. 60, no. 3, 035014, 2018.

[40] K. Svendsen, I. Gallardo González, M. Hansson, J. Björklund Svensson, H. Ekerfelt, A. Persson, and O. Lundh, "Optimization of soft X-ray phase-contrast tomography using a laser wakefield accelerator", *Optics Express*, vol. 26, no. 26, pp. 33930–33941, 2018.

[41] D. E. Spence, P. N. Kean, and W. Sibbett, "60-fsec pulse generation from a self-mode-locked Ti:sapphire laser", *Optics Letters*, vol. 16, pp. 42–44, 1991.

[42] I. Gallardo González, *Development and Applications of a Laser-Wakefield X-ray Source*. PhD thesis, Faculty of Engineering, LTH, 2018.

[43] E. B. Treacy, "Optical pulse compression with diffraction gratings", *IEEE Journal of Quantum Electronics*, vol. 5, no. 9, pp. 454–458, 1969.

[44] F. Campi, H. Coudert-Alteirac, M. Miranda, L. Rading, B. Manschwetus, P. Rudawski, A. L'Huillier, and P. Johnsson, "Design and test of a broadband split-and-delay unit for attosecond XUV-XUV pump-probe experiments", *Review of Scientific Instruments*, vol. 87, no. 2, 023106, 2016.

[45] P. H. Bucksbaum, R. R. Freeman, M. Bashkansky, and T. J. McIlrath, "Role of the ponderomotive potential in above-threshold ionization", *Journal of the Optical Society of America B*, vol. 4, pp. 760–764, 1987.

[46] H. Coudert-Alteirac, *Spatial and temporal characterization of intense attosecond pulses*. PhD thesis, Faculty of Engineering, LTH, 2018.

[47] D. Kroon, D. Guénot, M. Kotur, E. Balogh, E. Witting Larsen, C. M. Heyl, M. Miranda, M. Gisselbrecht, J. Mauritsson, P. Johnsson, K. Varjú, A. L'Huillier, and C. L. Arnold, "Attosecond pulse walk-off in high-order harmonic generation", *Optics Letters*, vol. 39, no. 7, pp. 2218–2221, 2014.

[48] L. Zehnder, "Ein neuer Interferenzrefraktor", *Zeitschrift für Instrumentenkunde*, vol. 11, pp. 275–285, 1891.

[49] L. Mach, "Über einen Interferenzrefraktor", *Zeitschrift für Instrumentenkunde*, vol. 12, pp. 89–93, 1892.

[50] H. Wikmark, "A high-order harmonic pump-probe setup using annular-beam interferometers", Master's thesis, Lund University, 2016.

[51] "nanoX 400 data sheet." Piezosystem Jena homepage, retrieved from `http://www.piezosystem.com/fileadmin/datasheets/nanoX/Nanopositioning-System-nanoX_400.pdf` on 2015-05-05.

[52] I. H. Malitson, "Interspecimen comparison of the refractive index of fused silica", *Journal of the Optical Society of America*, vol. 55, no. 10, pp. 1205–1209, 1965.

[53] J. Åqvist, W. van Gunsteren, M. Leijonmarck, and O. Tapia, "A molecular dynamics study of the C-terminal fragment of the L7L12 ribosomal protein: Secondary structure motion in a 150 picosecond trajectory", *Journal of Molecular Biology*, vol. 183, no. 3, pp. 461 – 477, 1985.

[54] H. Stapelfeldt and T. Seideman, "Colloquium: Aligning molecules with strong laser pulses", *Reviews of Modern Physics*, vol. 75, no. 2, pp. 543–557, 2003.

[55] P. Johnsson, A. Rouzée, W. Siu, Y. Huismans, F. Lépine, T. Marchenko, S. Düsterer, F. Tavella, N. Stojanovic, A. Azima, R. Treusch, M. F. Kling, and M. J. J. Vrakking, "Field-free molecular alignment probed by the free electron laser in hamburg (FLASH)", *Journal of Physics B: Atomic, Molecular and Optical Physics*, vol. 42, no. 13, 134017, 2009.

[56] "LNR50 series linear long-travel translation stage user guide." Thorlabs home page, retrieved from `https://www.thorlabs.com/_sd.cfm?fileName=17000-D01.pdf&partNumber=LNR50S/M` on 2019-03-22.

[57] J. Dahlström, "Generation, detection and optimisation of high order harmonics in neon", Master's thesis, Lund University, 2009.

[58] J. L. Wiza, "Microchannel plate detectors", *Nuclear Instruments and Methods*, vol. 162, no. 1-3, pp. 587–601, 1979.

[59] B. Henke, E. Gullikson, and J. Davis, "X-ray interactions: Photoabsorption, scattering, transmission, and reflection at E = 50 − 30, 000 eV, Z = 1 − 92", *Atomic Data and Nuclear Data Tables*, vol. 54, no. 2, pp. 181 – 342, 1993.

[60] F. Brunner, "Focus optimization of intense attosecond XUV pulses", Master's thesis, Lund University / ETH Zürich, 2017.

[61] H. Wolter, "Spiegelsysteme streifenden Einfalls als abbildende Optiken für Röntgenstrahlen", *Annalen der Physik*, vol. 445, no. 1-2, pp. 94–114, 1952.

[62] U. Even, "Pulsed supersonic beams from high pressure source: Simulation results and experimental measurements", *Advances in Chemistry*, vol. 2014, no. 636042, pp. 1–11, 2014.

[63] A. T. J. B. Eppink and D. H. Parker, "Velocity map imaging of ions and electrons using electrostatic lenses: Application in photoelectron and photofragment ion imaging of molecular oxygen", *Review of Scientific Instruments*, vol. 68, no. 9, pp. 3477–3484, 1997.

[64] L. Montgomery Smith, D. R. Keefer, and S. Sudharsanan, "Abel inversion using transform techniques", *Journal of Quantitative Spectroscopy and Radiative Transfer*, vol. 39, no. 5, pp. 367–373, 1988.

[65] M. J. J. Vrakking, "An iterative procedure for the inversion of two-dimensional ion/photoelectron imaging experiments", *Review of Scientific Instruments*, vol. 72, no. 11, pp. 4084–4089, 2001.

[66] G. A. Garcia, L. Nahon, and I. Powis, "Two-dimensional charged particle image inversion using a polar basis function expansion", *Review of Scientific Instruments*, vol. 75, no. 11, pp. 4989–4996, 2004.

[67] J. Ullrich, R. Moshammer, A. Dorn, R. Dörner, L. P. H. Schmidt, and H. Schniidt-Böcking, "Recoil-ion and electron momentum spectroscopy: reaction-microscopes", *Reports on Progress in Physics*, vol. 66, no. 9, pp. 1463–1545, 2003.

[68] L. J. Frasinski, K. Codling, and P. A. Hatherly, "Covariance mapping: A correlation method applied to multiphoton multiple ionization", *Science*, vol. 246, no. 4933, pp. 1029–1031, 1989.

[69] C. Huygens, *Traitée de la lumière*. Pieter van der Aa, 1690.

[70] T. Young, "The Bakerian lecture. On the theory of light and colours", *Philosophical Transactions of the Royal Society of London*, vol. 92, pp. 12–48, 1802.

[71] F. Zernike and F. J. M. Stratton, "Diffraction theory of the knife-edge test and its improved form, the phase-contrast method", *Monthly Notices of the Royal Astronomical Society*, vol. 94, no. 5, pp. 377–384, 1934.

[72] V. Lakshminarayanan and A. Fleck, "Zernike polynomials: a guide", *Journal of Modern Optics*, vol. 58, no. 7, pp. 545–561, 2011.

[73] J. Hartmann, "Bemerkungen über den Bau und die Justirung von Spektrographen", *Zeitschrift für Instrumentenkunde*, vol. 20, pp. 17–27, 47–58, 1900.

[74] W. Southwell, "Wave-front estimation from wave-front slope measurements", *Journal of the Optical Society of America*, vol. 70, no. 8, pp. 998–1006, 1980.

[75] R. Cubalchini, "Modal wave-front estimation from phase derivative measurements", *Journal of the Optical Society of America*, vol. 69, no. 7, pp. 972–977, 1979.

[76] B. C. Platt and R. Shack, "History and principles of Shack-Hartmann wavefront sensing", *Journal of Refractive Surgery*, vol. 17, no. 5, pp. S573–S577, 2001.

[77] C. Valentin, J. Gautier, J.-P. Goddet, C. Hauri, T. Marchenko, E. Papalazarou, G. Rey, S. Sebban, O. Scrick, P. Zeitoun, G. Dovillaire, X. Levecq, S. Bucourt, and M. Fajardo, "High-order harmonic wave fronts generated with controlled astigmatic infrared laser", *Journal of the Optical Society of America B*, vol. 25, no. 7, pp. B161–B166, 2008.

[78] S. Le Pape, P. Zeitoun, J.-F. Hergot, B. Carré, P. Dhez, M. François, M. Idir, H. Merdji, D. Ros, A. Carillon, and P. Salières, "Measurement of the wavefront of XUV sources", *Le Journal de Physique IV*, vol. 11, no. PR2, pp. 533–536, 2001.

[79] E. Frumker, G. G. Paulus, H. Niikura, D. M. Villeneuve, and P. B. Corkum, "Frequency-resolved high-harmonic wavefront characterization", *Optics Letters*, vol. 34, no. 19, pp. 3026–3028, 2009.

[80] D. T. Lloyd, K. O'Keeffe, P. N. Anderson, and S. M. Hooker, "Gaussian-Schell analysis of the transverse spatial properties of high-harmonic beams", *Scientific Reports*, vol. 6, 30504, 2016.

[81] A. S. Johnson, D. R. Austin, D. A. Wood, C. Brahms, A. Gregory, K. B. Holzner, S. Jarosch, E. Witting Larsen, S. Parker, C. S. Strüber, P. Ye, J. W. G. Tisch, and J. P. Marangos, "High-flux soft X-ray harmonic generation from ionization-shaped few-cycle laser pulses", *Science Advances*, vol. 4, no. 5, eaar3761, 2018.

[82] D. R. Austin, T. Witting, C. A. Arrell, F. Frank, A. S. Wyatt, J. P. Marangos, J. W. Tisch, and I. A. Walmsley, "Lateral shearing interferometry of high-harmonic wavefronts", *Optics Letters*, vol. 36, no. 10, pp. 1746–1748, 2011.

[83] D. G. Lee, J. J. Park, J. H. Sung, and C. H. Nam, "Wave-front phase measurements of high-order harmonic beams by use of point-diffraction interferometry", *Optics Letters*, vol. 28, no. 6, pp. 480–482, 2003.

[84] L. Freisem, G. S. M. Jansen, D. Rudolf, K. S. E. Eikema, and S. Witte, "Spectrally resolved single-shot wavefront sensing of broadband high-harmonic sources", *Optics Express*, vol. 26, no. 6, pp. 6860–6871, 2018.

[85] J. M. Beckers, "Adaptive optics for astronomy: Principles, performance, and applications", *Annual Review of Astronomy and Astrophysics*, vol. 31, no. 1, pp. 13–62, 1993.

[86] C. Radzewicz, P. Wasylczyk, W. Wasilewski, and J. S. Krasiński, "Piezo-driven deformable mirror for femtosecond pulse shaping", *Optics Letters*, vol. 29, no. 2, pp. 177–179, 2004.

[87] G. Vdovin and P. M. Sarro, "Flexible mirror micromachined in silicon", *Applied Optics*, vol. 34, no. 16, pp. 2968–2972, 1995.

[88] J. C. Dainty, A. V. Koryabin, and A. V. Kudryashov, "Low-order adaptive deformable mirror", *Applied Optics*, vol. 37, no. 21, pp. 4663–4668, 1998.

[89] L. Quintard, V. Strelkov, J. Vabek, O. Hort, A. Dubrouil, D. Descamps, F. Burgy, C. Péjot, E. Mével, F. Catoire, and E. Constant, "Mirrorless focusing of XUV high-order harmonics.." arXiv:1810.07282. Preprint, posted October 16, 2018.

[90] C. Hernández-García, J. San Román, L. Plaja, and A. Picón, "Quantum-path signatures in attosecond helical beams driven by optical vortices", *New Journal of Physics*, vol. 17, no. 9, 093029, 2015.

[91] L. Rego, J. San Román, A. Picón, L. Plaja, and C. Hernández-García, "Nonperturbative twist in the generation of extreme-ultraviolet vortex beams", *Physical Review Letters*, vol. 117, no. 16, 163202, 2016.

[92] F. Catoire, A. Ferré, O. Hort, A. Dubrouil, L. Quintard, D. Descamps, S. Petit, F. Burgy, E. Mével, Y. Mairesse, and E. Constant, "Complex structure of spatially resolved high-order-harmonic spectra", *Physical Review A*, vol. 94, no. 6, 2016.

[93] J. A. Pérez-Hernández, L. Roso, and L. Plaja, "Harmonic generation beyond the strong-field approximation: the physics behind the short-wave-infrared scaling laws", *Optics Express*, vol. 17, no. 12, 9891, 2009.

[94] C. G. Durfee III, A. R. Rundquist, S. Backus, C. Herne, M. M. Murnane, and H. C. Kapteyn, "Phase matching of high-order harmonics in hollow waveguides", *Physical Review Letters*, vol. 83, 2187, 1999.

[95] P. Salières, A. L'Huillier, and M. Lewenstein, "Coherence control of high-order harmonics", *Physical Review Letters*, vol. 74, no. 19, pp. 3776–3779, 1995.

[96] Z. L. Horváth and Z. Bor, "Focusing of truncated Gaussian beams", *Optics Communications*, vol. 222, no. 1-6, pp. 51–68, 2003.

[97] S. Ek, "Evaluation of the wavefronts and spatial structures of ultrashort pulses passing through a micro-channel plate", Master's thesis, Lund University, 2019.

[98] E. Lorek, E. Witting Larsen, C. M. Heyl, S. Carlström, D. Paleček, D. Zigmantas, and J. Mauritsson, "High-order harmonic generation using a high-repetition-rate turnkey laser", *Review of Scientific Instruments*, vol. 85, no. 12, 123106, 2014.

[99] M. Zürch, C. Kern, and C. Spielmann, "XUV coherent diffraction imaging in reflection geometry with low numerical aperture", *Optics Express*, vol. 21, no. 18, pp. 21131–21147, 2013.

[100] Y. Nabekawa, H. Hasegawa, E. J. Takahashi, and K. Midorikawa, "Production of Doubly Charged Helium Ions by Two-Photon Absorption of an Intense Sub-10-fs Soft X-Ray Pulse at 42 eV Photon Energy", *Physical Review Letters*, vol. 94, 043001, 2005.

[101] D. Attwood, *Soft X-rays and Extreme Ultraviolet Radiation*. Cambridge University Press, 1999.

[102] A. D. Rakić, "Algorithm for the determination of intrinsic optical constants of metal films: application to aluminum", *Applied Optics*, vol. 34, no. 22, pp. 4755–4767, 1995.

[103] D. L. Windt, W. C. Cash, M. Scott, P. Arendt, B. Newnam, R. F. Fisher, and A. B. Swartzlander, "Optical constants for thin films of Ti, Zr, Nb, Mo, Ru, Rh, Pd, Ag, Hf, Ta, W, Re, Ir, Os, Pt, and Au from 24 Å to 1216 Å", *Applied Optics*, vol. 27, no. 2, pp. 246–278, 1988.

[104] R. Kitamura, L. Pilon, and M. Jonasz, "Optical constants of silica glass from extreme ultraviolet to far infrared at near room temperature", *Applied Optics*, vol. 46, no. 33, pp. 8118–8133, 2007.

[105] R.-P. Haelbich and C. Kunz, "Multilayer interference mirrors for the XUV range around 100 eV photon energy", *Optics Communications*, vol. 17, no. 3, pp. 287 – 292, 1976.

[106] H. Mashiko, A. Suda, and K. Midorikawa, "Focusing coherent soft-x-ray radiation to a micrometer spot size with an intensity of 10^{14} W/cm^2", *Optics Letters*, vol. 29, pp. 1927–1929, 2004.

[107] J. H. Underwood, "9 - imaging properties and aberrations of spherical optics and nonspherical optics", in *Vacuum Ultraviolet Spectroscopy* (J. Samson and D. Ederer, eds.), pp. 145 – 181, Burlington: Academic Press, 2000.

[108] L. Poletto, F. Frassetto, F. Calegari, S. Anumula, A. Trabattoni, and M. Nisoli, "Microfocusing of attosecond pulses by grazing-incidence toroidal mirrors", *Optics Express*, vol. 21, no. 11, pp. 13040–13051, 2013.

[109] C. Bourassin-Bouchet, M. M. Mang, F. Delmotte, P. Chavel, and S. de Rossi, "How to focus an attosecond pulse", *Optics Express*, vol. 21, no. 2, pp. 2506–2520, 2013.

[110] P. Kirkpatrick and A. V. Baez, "Formation of optical images by X-Rays", *Journal of the Optical Society of America*, vol. 38, no. 9, pp. 766–774, 1948.

[111] F. Campi, *An intense attosecond light source - Towards extreme ultraviolet pump-probe experiments*. PhD thesis, Faculty of Engineering, LTH, 2017.

[112] E. A. Spiller, *Soft X-Ray Optics*. SPIE, 1994.

[113] V. N. Mahajan, "Strehl ratio for primary aberrations in terms of their aberration variance", *Journal of the Optical Society of America*, vol. 73, no. 6, pp. 860–861, 1983.

[114] J. Arnaud, "Representation of Gaussian beams by complex rays", *Applied Optics*, vol. 24, no. 4, pp. 538–543, 1985.

[115] T. Baumert, M. Grosser, R. Thalweiser, and G. Gerber, "Femtosecond time-resolved molecular multiphoton ionization: The Na_2 system", *Physical Review Letters*, vol. 67, no. 27, pp. 3753–3756, 1991.

[116] M. Isinger, D. Busto, S. Mikaelsson, S. Zhong, C. Guo, P. Salières, C. L. Arnold, A. L'Huillier, and M. Gisselbrecht, "Accuracy and precision of the RABBIT technique", *Philosophical Transactions of the Royal Society A: Mathematical, Physical and Engineering Sciences*, vol. 377, no. 2145, 20170475, 2019.

[117] M. Kotur, D. Guénot, A. Jiménez-Galán, D. Kroon, E. Witting Larsen, M. Louisy, S. Bengtsson, M. Miranda, J. Mauritsson, C. L. Arnold, S. E. Canton, M. Gisselbrecht, T. Carette, J. M. Dahlström, E. Lindroth, A. Maquet, L. Argenti, F. Martín, and A. L'Huillier, "Spectral phase measurement of a Fano resonance using tunable attosecond pulses", *Nature Communications*, vol. 7, 10566, 2016.

[118] D. Busto, J. Vinbladh, S. Zhong, M. Isinger, S. Nandi, M. Gisselbrecht, A. L'Huillier, E. Lindroth, and J. M. Dahlström, "Fano's propensity rule in angle-resolved attosecond pump-probe photoionization." arXiv:1811.05341. Preprint, posted November 13, 2018.

[119] V. Ayvazyan, N. Baboi, J. Bahr, V. Balandin, B. Beutner, A. Brandt, I. Bohnet, A. Bolzmann, R. Brinkmann, O. Brovko, J. Carneiro, S. Casalbuoni, M. Castellano, P. Castro, L. Catani, E. Chiadroni, S. Choroba, A. Cianchi, H. Delsim-Hashemi, G. Di Pirro, M. Dohlus, S. Dusterer, H. Edwards, B. Faatz, A. Fateev, J. Feldhaus, K. Flottmann, J. Frisch, L. Frohlich, T. Garvey, U. Gensch, N. Golubeva, H. Grabosch, B. Grigoryan, O. Grimm, U. Hahn, J. Han, M. Hartrott, K. Honkavaara, M. Huning, R. Ischebeck, E. Jaeschke, M. Jablonka, R. Kammering, V. Katalev, B. Keitel, S. Khodyachykh, Y. Kim, V. Kocharyan, M. Korfer, M. Kollewe, D. Kostin, D. Kramer, M. Krassilnikov, G. Kube, L. Lilje, T. Limberg, D. Lipka, F. Lohl, M. Luong, C. Magne, J. Menzel, P. Michelato, V. Miltchev, M. Minty, W. Moller, L. Monaco, W. Muller, M. Nagl, O. Napoly, P. Nicolosi, D. Nolle, T. Nunez, A. Oppelt, C. Pagani, R. Paparella, B. Petersen, B. Petrosyan, J. Pfluger, P. Piot, E. Plonjes, L. Poletto, D. Proch, D. Pugachov, K. Rehlich, D. Richter, S. Riemann, M. Ross, J. Rossbach, M. Sachwitz, E. Saldin, W. Sandner, H. Schlarb, B. Schmidt, M. Schmitz, P. Schmuser, J. Schneider, E. Schneidmiller, H. Schreiber, S. Schreiber, A. Shabunov, D. Sertore, S. Setzer, S. Simrock, E. Sombrowski, L. Staykov, B. Steffen, F. Stephan, F. Stulle, K. Sytchev, H. Thom, K. Tiedtke, M. Tischer, R. Treusch, D. Trines, I. Tsakov, A. Vardanyan, R. Wanzenberg, T. Weiland, H. Weise, M. Wendt, I. Will, A. Winter, K. Wittenburg, M. Yurkov, I. Zagorodnov, P. Zambolin, and K. Zapfe, "First operation of a free-electron laser generating GW power radiation at 32 nm wavelength", *European Physical Journal D*, vol. 37, no. 2, pp. 297–303, 2006.

[120] P. Tzallas, D. Charalambidis, N. A. Papadogiannis, K. Witte, and G. D. Tsakiris, "Direct observation of attosecond light bunching", *Nature*, vol. 426, pp. 267–271, 2003.

[121] A. M. Covington, A. Aguilar, I. R. Covington, M. F. Gharaibeh, G. Hinojosa, C. A. Shirley, R. A. Phaneuf, I. Álvarez, C. Cisneros, I. Dominguez-Lopez, M. M. Sant'Anna, A. S. Schlachter, B. M. McLaughlin, and A. Dalgarno, "Photoionization of Ne^+ using synchrotron radiation", *Physical Review A*, vol. 66, no. 6, 062710, 2002.

[122] J. B. West and G. V. Marr, "The absolute photoionization cross sections of helium, neon, argon and krypton in the extreme vacuum ultraviolet region of the spectrum", *Proceedings of the Royal Society of London. Series A*, vol. 349, no. 1658, pp. 397–421, 1976.

[123] M. Førre, S. Selstø, and R. Nepstad, "Nonsequential two-photon double ionization of atoms: Identifying the mechanism", *Physical Review Letters*, vol. 105, no. 16, 163001, 2010.

[124] F. Calegari, D. Ayuso, A. Trabattoni, L. Belshaw, S. De Camillis, S. Anumula, F. Frassetto, L. Poletto, A. Palacios, P. Decleva, J. B. Greenwood, F. Martin, and M. Nisoli, "Ultrafast electron dynamics in phenylalanine initiated by attosecond pulses", *Science*, vol. 346, no. 6207, pp. 336–339, 2014.

[125] E. P. Månsson, "Temporal gating of attosecond pulse trains", *Lund Reports on Atomic Physics*, vol. 403, 2008.

[126] R. C. Fort and P. von R. Schleyer, "Adamantane: Consequences of the diamondoid structure", *Chemical Reviews*, vol. 64, no. 3, pp. 277–300, 1964.

[127] J. Lahl, *Investigation of Ultrafast Molecular Dynamics via Covariance Mapping: A Tool for Intense XUV Light Sources*. PhD thesis, Faculty of Engineering, LTH, 2019.

[128] A. Marciniak, V. Despré, V. Loriot, G. Karras, M. Hervé, L. Quintard, F. Catoire, C. Joblin, E. Constant, A. I. Kuleff, and F. Lépine, "Electron correlation driven non-adiabatic relaxation in molecules excited by an ultrashort extreme ultraviolet pulse", *Nature Communications*, vol. 10, no. 1, 2019.

[129] J. R. Fienup, "Reconstruction of an object from the modulus of its Fourier transform", *Optics Letters*, vol. 3, no. 1, pp. 27–29, 1978.

[130] J. Miao, P. Charalambous, J. Kirz, and D. Sayre, "Extending the methodology of X-ray crystallography to allow imaging of micrometre-sized non-crystalline specimens", *Nature*, vol. 400, pp. 342–344, 1999.

[131] M. Zürch, J. Rothhardt, S. Hädrich, S. Demmler, M. Krebs, J. Limpert, A. Tünnermann, A. Guggenmos, U. Kleineberg, and C. Spielmann, "Real-time and sub-wavelength ultrafast coherent diffraction imaging in the extreme ultraviolet", *Scientific Reports*, vol. 4, 7356 EP, 2014.

[132] E. Malm *et al.*, "Singleshot polychromatic coherent diffraction imaging with a high-harmonic source", 2019. Manuscript in preparation.

[133] D. Whitley, "A genetic algorithm tutorial", *Statistics and Computing*, vol. 4, no. 2, pp. 65–85, 1994.

[134] E. Zeek, K. Maginnis, S. Backus, U. Russek, M. Murnane, G. Mourou, H. Kapteyn, and G. Vdovin, "Pulse compression by use of deformable mirrors", *Optics Letters*, vol. 24, no. 7, pp. 493–495, 1999.

[135] C. Valentin, O. Boyko, E. Papalazarou, G. Rey, B. Mercier, L. Antonucci, and P. Balcou, "Optimization of high harmonic generation by genetic algorithm", *Acta Physica Hungarica Series B, Quantum Electronics*, vol. 26, no. 3-4, pp. 335–342, 2006.

[136] D. R. Jones, M. Schonlau, and W. J. Welch, "Efficient global optimization of expensive black-box functions", *Journal of Global Optimization*, vol. 13, no. 4, pp. 455–492, 1998.

[137] C. Malherbe and N. Vayatis, "Global optimization of Lipschitz functions." arXiv:1703.02628. Preprint, posted June 15, 2017.

Printed by Media-Tryck, Lund 2019 NORDIC SWAN ECOLABEL 3041 0903

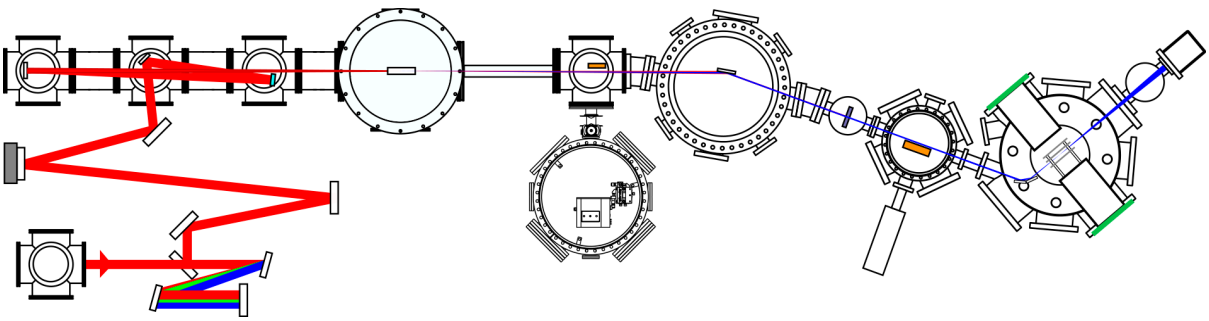

LUND UNIVERSITY

Lund University, Faculty of Engineering
ISBN 978-91-7895-042-3
ISSN 0281-2762
Lund Reports on Atomic Physics, LRAP-556